Surface studies of $Fe_3O_4(001)$, $Fe/Ge(001)$ and $Fe_3O_4(001)/Ge(001)$

A thesis submitted to the University of Dublin, Trinity College,

in application for the degree of Doctor in Philosophy

by

Kenneth Jordan

Physics Department

Trinity College Dublin

March 2006
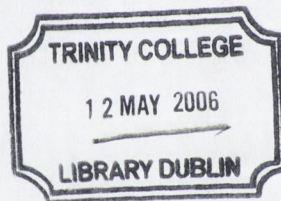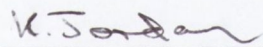
Declaration

This thesis is submitted by the undersigned for the degree of Doctor in Philosophy at the University of Dublin. It has not been submitted as an exercise for a degree at any other university.

Apart from the advice, assistance and joint effort mentioned in the acknowledgements and in the text, this thesis is entirely my own work.
I agree that the library may lend or copy this thesis freely on request.

Kenneth Jordan
March 2006

Acknowledgements

Firstly I would like to thank my supervisor Prof. Igor Shvets for giving me the opportunity to work in his group and the assistance he provided during the course of this thesis. Thanks also to Dr. Guido Mariotto, who first trained me to use the UHV system and shared his knowledge of the magnetite (001) surface. Over the last four years Dr. Shane Murphy has always helped out when things went wrong, equipment needed to be fixed, a thesis needed to be read, or coffee needed to be drank.

My fellow Ph.d. students in the group have made this an enjoyable four years. Sergio F. Ceballos "trained" me for my first job in the group: the cutting of a rather hard lump of MnNi using a diamond wheel saw. I went on to work with him for most of my time here, and despite the awful 80's music, he was an excellent person with whom to share a lab, and to discuss the finer points of the magnetite unit cell with (until he broke it). Giuseppe Manai, who arrived a week or two after I started, has also been an excellent colleague and friend over the last four years. Other than the many hours spent in work, I have had dinner in his place numerous times and we have drank countless pints together. I also thank Lucia, who hosted a skiing trip (with no snow!!), has come for lunch throughout the four years, and recently made me proper Italian lasagne. Alex Cazacu also started around the same time as myself, and luckily for me was given the task of building the low temperature STM. I still haven't got to taste the Romanian liquor I was promised 4 years ago, but at least I did get a traditional Romanian meal, (of Goodfellas pizza). Kevin Radican, a more recent addition to the group, has shown Americans are not so bad, (but that's probably because his mother is Irish). He has provided a colleague who finds changing other people's computer settings and wallpaper

as entertaining as I do.

Thanks also to all the other group members past and present, Anselm, William, Victor, Roman, Vivienne, Dimitri, Nikolai, Sunil, Jin and Yang Xuesong, Sumesh, Ciaran (who gave the group a much needed boost in Irishness), Gops, Rafa, Floriano, Keith and Anthony. Also Marie Kinsella for her effective administration work and organising trips to conferences.

The group could not operate without the efforts of all the departmental staff; John Kelly, Mick Reilly (who machined countless parts for the (not so) Ti - STM.), Ken Concannon, Joe McCauley, Pat Flanagan, Michelle Duffy, Susan Priest and Elaine O'Malley.

I would also like to thank Emma Kerr and Gregory Cabailh. Emma has provided company for many coffees, teas, choc ices, feasts and, of course, pints of porter. She has been a great friend, for gossiping and listening to my Ph.d and other moans, and I suppose I owe her a dinner or two. Gregory Cabailh was usually with myself and Emma drinking those pints of porter, and was much missed on his departure from Trinity. Thanks to all my friends from the Glasvevin/Finglas/Ballymun (take your pick!!) area. From mid write-up holidays, to fleadh ceoils, to weekend sessions; Rob, Mark, John, Andy and the later addition of Eoin (who's not from the northside at all) made the last four years highly enjoyable. Also Caroline who, from living in the villas, virtually qualifies as one of the lads. Last but not least, in the "friends" category, thanks to Emma, who reminded me that first dates are far more stressful than I had remembered, and has since redeemed my opinion of southsiders and pharmacists.

Finally, thanks to my family. Firstly, my Grandfather, Michael, who wonders why the heck I don't have a proper job at the age of 26. My sister, Lorraine, and brother-in-law, Chris, have been great to me over the last few

years, with most of my worldly possessions coming courtesy of them. My parents, William and Mildred, have kept me fed and sheltered, and put up with me spending what little money I had on holidays to far away places. Most importantly they have been there for me throughout, and I dedicate this thesis to them.

Abstract

This work consists of surface studies of three systems; firstly, the (001) surface of a Fe_3O_4 single crystal, secondly, the initial nucleation of Fe on the Ge(001) surface, and finally, iron oxide formed on Ge(001).

The magnetite (001) surface was studied using Auger electron spectroscopy (AES), low energy electron diffraction (LEED), scanning tunneling microscopy (STM) and scanning tunneling spectroscopy (STS). The clean surface is shown to exhibit the $(\sqrt{2} \times \sqrt{2})R45°$ LEED mesh. The surface is imaged with tips made from both antiferromagnetic MnNi and non-magnetic W. An enhanced atomic scale contrast is imaged with the MnNi tips, which is explained in terms of a spin polarised contribution to the tunneling current. A model of the surface termination is put forward.

AES, LEED and STM/STS were also used to study the Fe/Ge(001) system. The work concentrates on the initial nucleation of Fe on the (2×1) reconstructed surface. The clean surface is characterised and then the nucleation of sub-monolayer Fe films is studied. STS is carried out on the surface. The influence of elevated substrate temperature on the nucleation is also examined, as is post annealing of films deposited at room temperature, and the temperature dependence of intermixing between the Fe and Ge.

Finally iron oxide/Ge(001) is studied. The oxide is formed by post annealing of Fe films on Ge(001). The surface of the films are characterised with AES, LEED and STM/STS. The results are consistent with the formation of magnetite (001). The effect of annealing temperature on the surface is also examined.

Publications

K. Jordan, G. Mariotto, S. F. Ceballos, S. Murphy and I. Shvets. "Atomic scale SPSTM imaging of the $Fe_3O_4(001)$ surface using antiferromagnetic tips". J. Mag. Mag. Mat. **290-291**, 1029, (2005).

I. V. Shvets, G. Mariotto, K. Jordan, N. Berdunov, R. Kantor, and S. Murphy. "Long-range charge order on the $Fe_3O_4(001)$ surface". Phys. Rev. B. **70**, 155406, (2004).

S.F. Ceballos., G. Mariotto, K. Jordan, S. Murphy and I. Shvets. "An atomic scale study of the $Fe_3O_4(001)$ surface". Surf. Sci. **548**, 106-116, (2004).

S. Murphy, S.F. Ceballos, G. Mariotto, N. Berdunov, K. Jordan, I.V. Shvets and Y.M. Mukovskii. "Atomic scale spin-dependent scanning tunneling microscopy using antiferromagnetic STM tips". Microscopy Research and Techniques. **66**, 85-92, (2005).

S. F. Ceballos, K. Jordan, S. Murphy, C. Seoighe, and I. V. Shvets. "Contaminants Induced Onset of Nanostripes and Nanotrenches on the Fe_3O_4 (001) Surface". AIP Conf. Proc. **696**, 879, (2003).

G. Mariotto, K. Jordan, S. F. Ceballos, S. Murphy, C. Seoighe, and I. V. Shvets. "Charge Ordering on the $(\sqrt{2} \times \sqrt{2})R45°$ Reconstructed $Fe_3O_4(001)$ Surface". AIP Conf. Proc. **696**, 873, (2003).

List of abbreviations

1D - one dimensional

2D - two dimensional

3D - three dimensional

AES - Auger electron spectroscopy

CMA - cylindrical mirror analyser

DFT - density functional theory

DMS - dilute magnetic semiconductor

DOS - density of states

e-beam - electron beam

HT - high-temperature

L - Langmuir

LDOS - local density of states

LEED - low energy electron diffraction

LT - low-temperature

LTSTM - low-temperature scanning tunneling microscopy

MBE - molecular beam epitaxy

ML - monolayer

PES - photo-electron spectroscopy

RT - room temperature

RTSTM - room-temperature scanning tunneling microscopy

SPM - scanning probe microscopy

SPSTM - spin polarised scanning tunneling microscopy

STM - scanning tunneling microscopy

STS - scanning tunneling spectroscopy

TMR - tunneling magneto resistance

TSP - titanium sublimation pump

UHV - ultra high vacuum

XPS - X-ray photo-electron spectroscopy

XRD - X-ray diffraction

List of Figures

IX

Contents

Chapter 1

Introduction

Current semiconductor technology makes use of electron charge for information processing. On the other hand, magnetic recording devices, which make use of the spin of the electron, are generally used for mass storage of information. The possibility of making devices which allow the use of both the charge and spin of the electron is the focus of much current research [1, 2]. For example, the growth and characterisation of proposed half metals [3], fabrication and measurements of new ferromagnetic semiconductors [4–6], and the growth of ferromagnetic layers on semiconductors with a view to injection spin polarised carriers [7, 8] are all highly active areas of research.

Within this field, magnetite, Fe_3O_4, has attracted much interest due to the fact that it is predicted to be a half metallic ferromagnet; that is, the electrons at the Fermi level are 100% spin polarised [9]. This fact, coupled with its relatively high T_c, makes it a suitable candidate for use as a source of spin polarised electrons. A detailed knowledge of the surface properties of this material is essential for device development. To this end, the study presented here involves a detailed investigation of the (001) surface of magnetite, using Auger electron spectroscopy (AES), low energy electron diffraction (LEED)

1

and scanning tunneling microscopy and spectroscopy (STM/STS).

Fe/semiconductor systems have also attracted much interest due to the possibility of injecting spin polarised carriers from the ferromagnetic layer into the semiconductor. This avenue towards integrating charge and spin electronics is perhaps the most suited to current processing technologies [7]. Such spin injection has already been successfully demonstrated [10]. The work presented here concentrates on the initial nucleation of Fe onto the Ge(001) substrate, for deposition at both room temperature and elevated substrate temperature. The types of Fe island formed on the surface, and the influence of the islands on the Ge substrate, are discussed in detail. The system is also studied with regard to the integrity of the interface, and the onset of intermixing following post annealing. Intermixing at the ferromagnetic/semiconductor interface is an important issue, as it drastically alters the electronic, magnetic, and transport properties of the interface.

Finally, it is of interest to attempt to grow proposed half metallic materials, such a magnetite, on semiconductor substrates [11, 12]. This is to investigate the possibility of integration of potential spin polarised carrier sources into current processing technologies. In the work presented here, Fe films on Ge(001) are oxidised and charaterised using AES, LEED and STM/STS. The results are in agreement with the formation of magnetite (001).

Chapter 2

Experimental Techniques and Set-up

2.1 Background of Experimental Techniques

2.1.1 Auger Electron Spectroscopy

Auger electron spectroscopy (AES) is one of the most important, and widely used, chemically sensitive surface analysis tools for conducting and semiconducting samples [13,14]. The technique is based on the excitation of so-called "Auger electrons". A schematic of the process is shown in figure 2.1. The sample is bombarded with primary electrons of energy 3 - 10 keV. For the example shown in the figure the, so called, K level is ionised by an incident electron. For ionisation to occur the energy of the incident electron, E_p, must be greater than the binding energy of the electron in the K level, E_K. A hole is created in the K level, which is subsequently filled via an electron transition from an outer level, shown as L_1 in the schematic. Following the transition an excess energy, $(E_K\text{-}E_{L1})$, is available. This energy can be used in one of
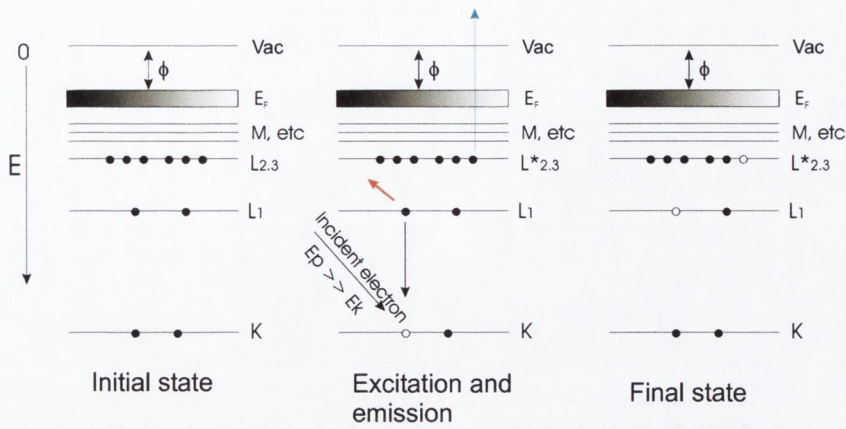
Figure 2.1: Schematic of the Auger emission process. The ground state is shown on the left. Centre: An incident electron of energy E_p creates a hole in the core level, K, by ionisation. Relaxation occurs and an electron from the L_1 level fills the core level hole, releasing an energy, $(E_k\text{-}E_{L1})$. This energy can be emitted as a photon (red arrow), or can be given to a secondary electron, which is then emitted from the crystal (blue arrow). The state following emission is shown on the right.

two ways. Firstly a characteristic X-ray photon of energy $(E_K\text{-}E_{L1})$ can be emitted. This is called X-ray fluorescence. Alternatively this energy can be given to another (secondary) electron, occupying either the same level or a more shallow level, and this secondary electron is then ejected. This is the process of Auger emission. The Auger transition of figure 2.1 is labelled as $KL_1L_{2,3}$. The Auger electrons have a characteristic energy for each element, allowing one to identify the element emitting them. The technique renders information on the elemental composition of the first 2-10 atomic layers [13].
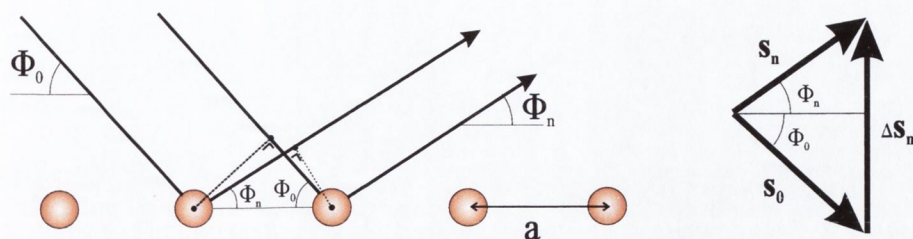
Figure 2.2: Schematic of the Bragg condition for a 1-D lattice, as explained in the text.

2.1.2 Low Energy Electron Diffraction

Low energy electron diffraction (LEED) is an important technique in the field of surface science, which allows one to determine the structure and degree of order of a crystal surface [15, 16]. A beam of monochromatic low energy electrons is incident normal to the sample. If the sample has a well ordered crystalline surface then for certain energies the impinging electron beam is elastically back-scattered by the Bragg planes of the crystal back onto a fluorescent screen, which displays the diffraction pattern of the surface.

The impinging electron beam may be regarded as a succession of electron waves incident on the crystalline sample. These waves will be scattered by the atoms of the crystal, as they are areas of high electron density. The atoms can be considered to act as point particles. A plane wave incident on an atom, or the atoms of a unit cell, will be scattered in all directions. However, for a crystal, interference between the scattered waves from neighbouring unit cells will restrict the net flux to those directions in which the scattered waves from all of the unit cells are in phase. This condition is met only when the scattered waves from neighbouring cells differ by an integral number of wavelengths, λ. For the simple case of a 1-D lattice this in-phase condition for constructive interference is met for all integers, n, that satisfy the condition:

$$a(cos\phi_n - cos\phi_o) = n\lambda \qquad (2.1)$$

where a is the distance between the scattering planes, λ is the wavelength of the incident wave, ϕ_o is the angle of the incident plane wave with respect to the plane of the crystal, and ϕ_n the angle of the emergent beam with respect to the plane of the crystal. This condition is known as the Bragg condition, and is illustrated schematically in figure 2.2. Describing the incident beam and the emergent beam as vectors, $\vec{s_o}$ and $\vec{s_n}$ respectively, this can be re-written as

$$\vec{a}.(\vec{s_n} - \vec{s_o}) = n\lambda \qquad (2.2)$$

or

$$\vec{a}.\Delta\vec{s_n} = n\lambda \qquad (2.3)$$

where

$$\Delta\vec{s_n} = \vec{s_n} - \vec{s_o} \qquad (2.4)$$

This is known as the Laue condition, which requires that the three vectors $\vec{s}$, $\vec{s_n}$ and $\Delta\vec{s_n}$ form a triangle with two identical sides. The diffracted beams are determined by $\Delta\vec{s_n}$ and, in the one dimensional case, they are given by integral multiples of the basic unit $(\lambda/\vec{a})$. This involves the reciprocal of the real space lattice vector, $\vec{a}$, and we thus define the reciprocal lattice vector, $\vec{a^*}=1/\vec{a}$.

For surface diffraction to occur in a 2D system, with translation vectors $\vec{h}$ and $\vec{l}$, the incoming electron beam must conserve both its energy and the component of its momentum parallel to the surface:

$$\vec{k_{\parallel}}^2 + \vec{k_{\perp}}^2 = \vec{k'_{\parallel}}^2 + \vec{k'_{\perp}}^2 \ , \quad \vec{k'_{\parallel}} = \vec{k_{\parallel}} + \vec{g_{hl}} \qquad (2.5)$$

where $\vec{k}_{\parallel}$ and $\vec{k}_{\perp}$ are the parallel and perpendicular momentum components of the incident beam, while $\vec{k}_{\parallel}'$ and $\vec{k}_{\perp}'$ are those of the diffracted beam. The reciprocal lattice vector, now labelled $\vec{g}_{hl}$, is related to the beam energy E_{eV}, the electron mass m_e, and the diffraction angle α by:

$$|\vec{g}_{hl}| = |h\vec{a^*} + l\vec{b^*}| = |\vec{k}|sin\alpha = \frac{\sqrt{2m_e E_{eV}}}{\hbar}sin\alpha \qquad (2.6)$$

where $\vec{a^*}$ and $\vec{b^*}$ are the reciprocal lattice primitive net vectors. These are related to the real space vectors $\vec{a}$ and $\vec{b}$ by [17]:

$$\vec{a}.\vec{a^*} = \vec{b}.\vec{b^*} = 2\pi \quad \vec{a}.\vec{b^*} = \vec{b}.\vec{a^*} = 0 \qquad (2.7)$$

This shows the direct correspondence between the observed diffraction pattern and the reciprocal lattice of the surface. The reciprocal lattice vector $\vec{g}_{hl}$ lies in a direction that is orthogonal to the plane of the real space lattice that is denoted by the Miller indices h and l. The Miller indices of the diffracting planes are used to index the diffraction spots of the LEED pattern.

In general, for LEED experiments, the sample is normal to the incoming beam. This means that $\vec{k}_{\parallel} = 0$ for the incident electrons. Therefore the observed diffraction pattern will be an image of the reciprocal lattice of the surface. LEED patterns of surfaces are taken at energies ranges between 20 and 500 eV. In this energy range the de Broglie wavelength of electrons have the same order of magnitude as the interatomic distances of crystals. The electron mean free path is of the order of $\sim$ 5 - 10 Å, meaning that this technique is sensitive only to the surface layers.

2.1.3 Scanning Tunneling Microscopy

The scanning tunneling microscope (STM), invented in 1981, revolutionised the field of surface science [18]. For the first time it allowed the "real space"

imaging of the surface structure of conducting and semiconducting samples, down to the atomic scale. However, as is explained below, in reality the technique probes the electronic structure of the surface, rather than the actual topographical structure. Detailed descriptions of the technique and its uses are found in references [19, 20].

Tunneling Theory

The STM is based on the principle of quantum mechanical tunneling. According to classical mechanics the probability of an electron tunneling through a potential barrier is zero. However, according to quantum mechanics the electron has a non-zero probability of tunneling through the barrier. The dynamics of the free electron model of a metal-vacuum contact are described by the Schrödinger equation:

$$-\frac{\hbar^2}{2m}\frac{d^2}{dz^2}\psi(z) + U(z)\psi(z) = E\psi(z) \tag{2.8}$$

where m is the electron mass and $\hbar = h/2\pi$ (where h is Planck's constant). In the classically allowed region where $E > U(z)$, this equation has solutions of the form:

$$\psi(z) = \psi(0)e^{\pm ikz}, \quad k = \frac{\sqrt{2m(E-U)}}{\hbar} \tag{2.9}$$

where the electron can move in either the positive or negative sense of direction.

In the classically forbidden barrier region where $E < U(z)$, the Schrödinger equation has the solution:

$$\psi(z) = \psi(0)e^{-\kappa z}, \quad \kappa = \frac{\sqrt{2m(U-E)}}{\hbar} \tag{2.10}$$

The κ term describes the decay of the electron wavefunction within the barrier region. For a finite potential $U(z)$, there is a non-zero probability P of

finding the electron at a position z inside the barrier region, which is given by:

$$P \propto \mid \psi(0) \mid^2 e^{-2\kappa z} \tag{2.11}$$

Consequently, if the width of the tunnel barrier is sufficiently narrow, there is a finite probability that the electron can tunnel through the classically forbidden barrier region.

It is this electron tunneling that the STM exploits. An STM junction [Fig. 2.3(b)] consists of a sharp metallic tip, stabilised at a distance of a few Å from a conducting sample. The height of the tunnel barrier is determined by the work function ϕ of both the tip and the sample. The work function is the minimum energy necessary to remove an electron from the metal to vacuum. For convenience the work function of tip and sample are considered to be identical in the following discussion of the technique. Those electrons with Fermi energy $E_f = -\phi$ have the greatest tunneling probability, since by definition the Fermi level, E_f, denotes the upper limit of electron occupancy. In the absence of an applied bias, electrons have an equal probability of tunneling through the barrier in either direction, and so there is no net tunnel current. On the application of an external bias voltage V, electrons in the sample (or tip, depending on polarity) within the energy range $E_F - eV \leq E \leq E_F$ have an increased probability of tunneling through the barrier. If eV $\ll \phi$, then only electron states very near to the Fermi level are probed.

The probability that an electron in the nth electron state will tunnel through a barrier of width W is then given by:

$$P \propto \mid \psi_n(0) \mid^2 e^{-2\kappa W}, \quad \kappa = \frac{\sqrt{2m\phi}}{\hbar} \tag{2.12}$$

Considering all of the states in the energy range probed, $E_F - eV \leq E \leq E_F$,
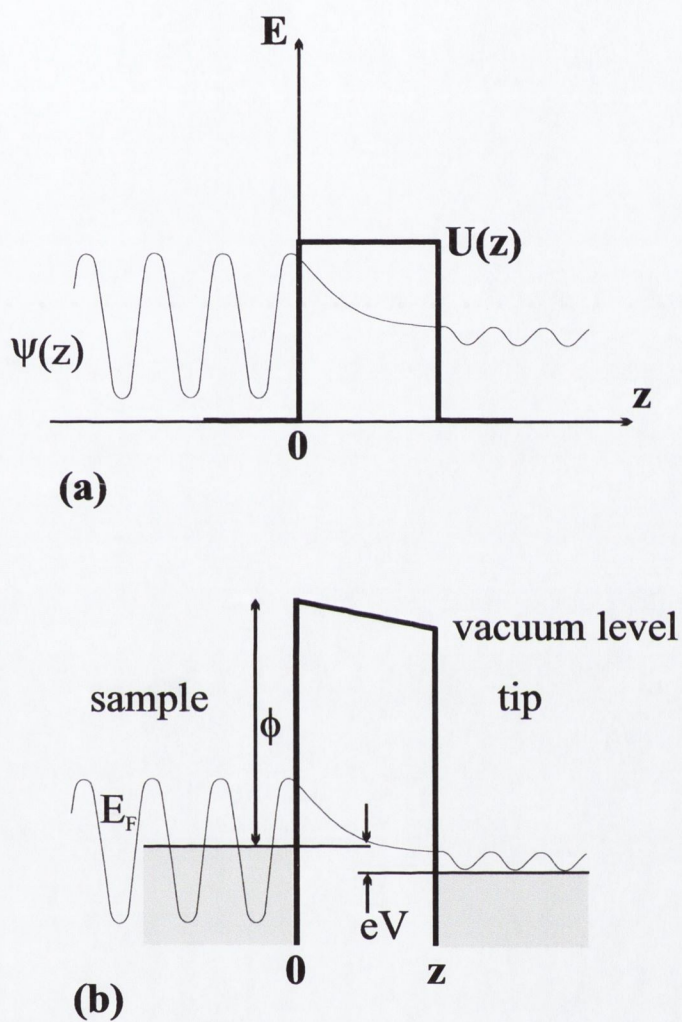
Figure 2.3: Schematic representations of (a) an electron described by the wavefunction $\psi(z)$ travelling in a one-dimensional potential U(z) and (b) a STM junction under an applied bias V.

the tunnel current is:

$$I_t \propto \sum_{E=E_F-eV}^{E_F} \mid \psi(0) \mid^2 e^{-2\kappa W} \tag{2.13}$$

Rewriting this equation, in terms of the local density of states (LDOS), at E_f, of the sample surface, $\rho_s(0, E_F)$:

$$I_t \propto V\rho_s(0, E_F)e^{-2\kappa W} \tag{2.14}$$

From this equation one can see that; (i) the tunnel current is directly proportional to the bias voltage applied across the tunnel junction, and (ii), the tunnel current decays exponentially as the width of the tunnel barrier (i.e tip-sample separation) increases. The tunneling current is also dependent on the LDOS of the tunneling tip. The significance of the tip contribution can be accounted for through a time dependent perturbation model of metal-insulator-metal tunneling, proposed by Bardeen [21]. In this approach a Transfer Hamiltonian H_T is used to describe the tunneling of an electron, from a sample state ψ, to a tip state χ. The tunnel current is a convolution of the sample LDOS ρ_s and the tip LDOS ρ_t.

$$I_t = \frac{4\pi e}{\hbar} \int_0^{eV} \rho_s(E_F - eV + E)\rho_t(E_F - E) \mid M \mid^2 dE \tag{2.15}$$

The tunnel current I_t also includes a tunneling matrix element M, which describes the amplitude of electron transfer across the tunneling barrier, as a function of the overlap between sample states (ψ) and tip states (χ).

$$M = \frac{\hbar}{2m} \int (\chi^* \frac{\partial \psi}{\partial z} - \psi \frac{\partial \chi^*}{\partial z})dS \tag{2.16}$$

It is determined by a surface integral on the medium separating the two electrodes. If M is constant over the voltage range probed, the tunnel current

is determined by a convolution of the LDOS of the two electrodes, the tip, and the sample.

Spin Polarized Tunneling

The above treatment shows that the tunnel current between the tip and the sample depends on the width of the tunnel barrier W, the local barrier height ϕ, and the applied sample bias V:

$$I = I(W, \phi, V) \tag{2.17}$$

However, if magnetic electrodes are involved there is an additional, spin-dependant, contribution to the tunneling current:

$$I = I(W, \phi, V, \uparrow) \tag{2.18}$$

Spin-dependant tunneling was first demonstrated by Tedrow and Merservey, using planar ferromagnetic-oxide-superconductor tunnel junctions [22]. Within the Stoner model of ferromagnetism, the spin-up and spin-down parts of the spin-dependent density of states of the ferromagnetic electrode are shifted relative to each other by the exchange energy. As a result, the spin-up and spin-down parts of the DOS have different magnitudes at E_f. Due to the differing DOS of the two spin species the current-voltage characteristics of the junction were observed to be asymmetric.

Spin-dependent tunneling has also been observed in ferromagnet-insulator-ferromagnet junctions [23]. This case was theoretically treated by Slonczewski [24]. He considered a tunnel junction with two identical ferromagnetic electrodes, labelled f, separated by an insulating barrier b, where the directions of the internal magnetic fields of the electrodes differ by an angle θ. Within the free electron model, and in the limit of small applied
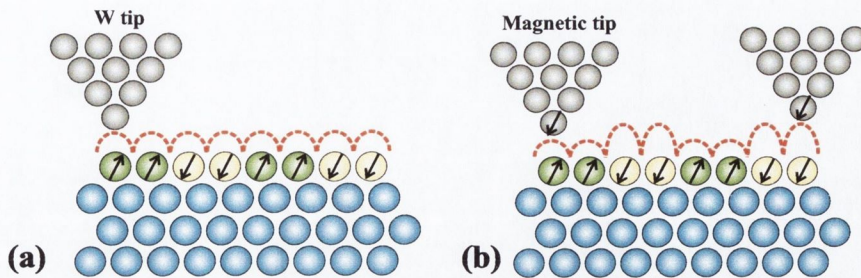
Figure 2.4: Schematic of spin polarised scanning tunneling microscopy. (a): Using a W tip, which does not have a spin split density of states, all atoms are imaged as equivalent. (b): Using a tip made from magnetic material, which has a spin split density of states, results in enhanced tunneling for one spin type over the other, allowing one to resolve atoms with different spin configurations.

bias, Slonczewski found the following expression for the conductance of the junction:

$$\sigma = \sigma_{fbf}(1 + P_{fb}^2 cos\theta), \mid P_{fb} \leq 1 \tag{2.19}$$

In this equation, P_{fb} is the effective spin polarization of the ferromagnetic-barrier interface and σ_{fbf} is a mean conductance, which is proportional to exp(-2κz). For differing ferromagnetic electrodes the conductance is:

$$\sigma = \sigma_{fbf}(1 + P_{fb}P_{f'b})cos\theta, \mid P_{fb} \leq 1 \tag{2.20}$$

For the two cases where the internal magnetic fields of the junction electrodes are parallel and anti-parallel:

$$\sigma_{\uparrow\uparrow} = \sigma_{fbf}(1 + P_{fb}P_{f'b}) \tag{2.21}$$

$$\sigma_{\uparrow\downarrow} = \sigma_{fbf}(1 - P_{fb}P_{f'b}) \tag{2.22}$$

The effective spin polarization for the whole junction is then found to be:

$$P_{fbf'} = P_{fb}P_{f'b} = \frac{\sigma_{\uparrow\uparrow} - \sigma_{\uparrow\downarrow}}{\sigma_{\uparrow\uparrow} + \sigma_{\uparrow\downarrow}} \tag{2.23}$$

The use of a magnetic STM tip to image a magnetic sample can therefore yield information on the magnetic structure of the sample [Fig.2.4]. However, some aspects of this technique are still not well understood, such as separating the magnetic and electronic contributions to the tunnel current and the magnetization direction, and degree of spin polarization, of the tips used for the experiments. A recent review of the technique is found in reference [25].

Scanning Tunneling Spectroscopy

As has already been discussed, the tunnel current in a tunneling junction is dependent on the barrier width, the local barrier height and the applied bias voltage. When tunneling between metallic electrodes in the low bias limit ($\sim$ mV), the tunnel current varies linearly with bias voltage. However, for higher bias the tunnel current generally does not exhibit Ohmic behaviour, and the image obtained with STM can vary greatly with junction bias. This is particularly true for semiconductor surfaces. Scanning tunneling spectroscopy (STS) allows one to examine how the tunnel current varies with voltage by acquiring I(V) curves of the tip-sample tunnel junction [19]. In general, the feedback loop is interrupted for a few hundred microseconds so that the tip sample distance remains constant during the curve acquisition. There is a delay to allow the sample-tip distance to stabilise. Due to the exponential dependence of tip-sample distance on the tunnel current it is vital that this distance remains constant during the curve aquisition. The bias voltage is then ramped through the desired range and the I(V) characteristic of the junction measured. The feedback loop is then re-engaged and scanning continues. Curves can be taken at a single point, or a grid I(V) map of the

surface can be obtained. As the tunnelling current is a convolution of the tip and sample DOS the measurement will only contain meaningful information about the sample DOS if the tip DOS is constant over the voltage range used:

$$\rho_t(E) = const \qquad (2.24)$$

and again using the assumption that the tunnelling matrix element M is constant over the voltage range probed, then from equation 2.15:

$$\frac{dI}{dV} \propto \rho_s(E_f - E_v + E) \qquad (2.25)$$

This equation essentially means that, assuming the validity of the above assumptions, a measure of the sample DOS can be obtained from the derivative of the I(V) curve. However, it must be borne in mind that, in reality, the assumption of a constant M does not hold. The tunnelling probability is always highest for states at the Fermi level. Therefore when tunnelling from the tip to the sample, most of the tunneling electrons will come from the Fermi level of the tip, and will probe the empty states of the sample. However, when tunnelling from sample to tip most of the tunneling electron will come from the Fermi level of the sample, therefore offering limited information on the occupied states of the sample. A data normalization process, first proposed by J. Stroscio et al. [26] and N.D. Lang [27] can help solve this problem. From equation 2.15:

$$I_t \propto \int_0^{eV} \rho(E)D(E)dE \qquad (2.26)$$

where D(E) is the transmission probability for an electron.

$$\frac{dI/dV}{I/V} \approx \frac{dlnI}{dlnV} \approx \frac{\rho(eV)D(eV)}{\frac{1}{eV}\int_0^{eV} \rho(E)D(E)dE} + \dots \qquad (2.27)$$

Then, to a first order approximation, the transmission probability cancels and the normalised conductivity is approximately proportional to the DOS;

$$\frac{dI/dV}{I/V} \approx \frac{\rho(eV)}{\frac{1}{eV}\int_0^{eV}\rho(E)dE} \tag{2.28}$$

The inherent weakness of STS as a spectroscopic technique is that it only maps the electronic states that protrude from the sample and significantly overlap with the tip wavefunction, essentially resulting in a negative penetration depth [19].

2.2 Experimental Set-up

The original ultra high vacuum (UHV) system was designed and constructed by Professor I.V. Shvets, Dr. A. Quinn and Dr. J. Osing. It consists of three main chambers, the preparation chamber, the room-temperature STM (RT-STM) chamber and the low-temperature STM (LTSTM) chamber. The layout of this system is shown schematically in figure 2.5. A full description of the construction and operation of the RTSTM is given by Quinn [28]. The LTSTM description can be found in reference [29], while a detailed description of the preparation chamber is found in reference [30].

Each chamber can be valved off from the rest of the system via a series of UHV gate valves (VAT [31]) and brought to atmospheric pressure for maintenance without breaking vacuum in the rest of the system. A fast entry loadlock is connected to the preparation chamber by a gate valve, allowing the introduction of samples and tips without breaking vacuum. When not in use, this loadlock is usually maintained in the low 10^{-7} mbarr range by a 20 L.s^{-1} differential ion-pump (Perkin-Elmer [32]). Tip and sample transfer throughout the system is facilitated by a series of wobblesticks and

0.5 m

RTSTM chamber

LEED/AES optics

220 ls^{-1}ion pump

Gate valve

Loadlock with 20 ls^{-1} ion pump

220 ls^{-1}ion pump

Preparation chamber

240 ls^{-1}ion pump

LTSTM chamber

260 ls^{-1} turbomolecular pump
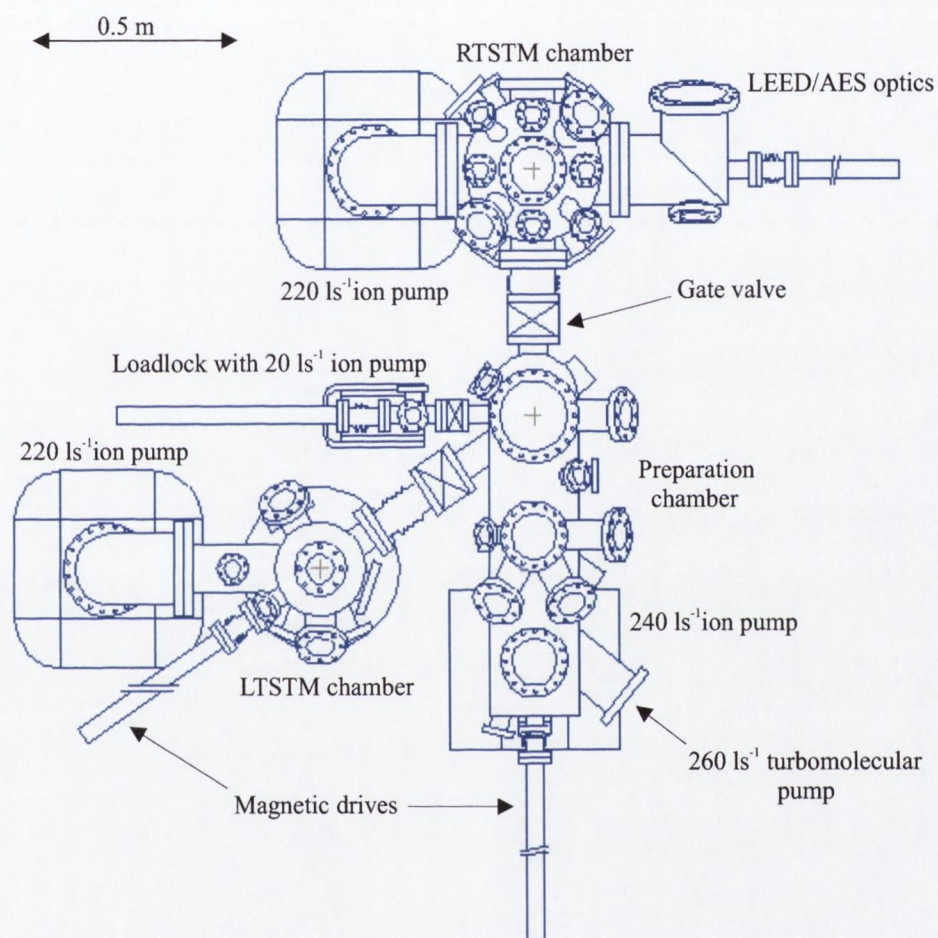
Magnetic drives

Figure 2.5: Top view schematic of the UHV system.

magnetically-coupled linear drives (Vacuum Generators Ltd. [33]) which can access each sample stage. The pressure in each chamber is monitored using nude Bayard-Alpert type ionisation gauges (Perkin-Elmer [32]). The entire system is supported on a stainless steel box-section frame which can be floated on pneumatic dampers to isolate the system from building vibrations during STM operation. The box-section is filled with gravel to minimise hollow pipe vibrations.

2.2.1   The Preparation Chamber

The preparation chamber was design by Dr. S. Murphy [30] and manufactured by Caburn-MDC Ltd. [34]. To achieve UHV the chamber is usually baked for 3 days at ~150°C. A base pressure of ~ 1.33×10^{-10} mbar is obtained in this chamber after baking out.

A number of pumps are used to achieve UHV conditions in the chamber. Firstly a 260 L.s^{-1} turbomolecular pump (Pfeiffer Vacuum [35]), which is backed by a 0.7 L.s^{-1} two-stage rotary vane pump. A double-ended 240 L.s^{-1} differential ion-pump (Physical Electronics [32]) is used to maintain UHV conditions. A liquid nitrogen cryoshroud is inserted in the base flange of the ion-pump, which houses a titanium sublimation pump (TSP). Finally a non-evaporable getter pump (NEG), from SAES Getters [36], is positioned mid-way along the chamber.

The chamber contains facilities for in-situ tip and sample preparation: a resistive heater, an Ar$^+$ ion gun, precision leak valves for the introduction of high purity gases, a triple evaporator with integral flux monitor (Omicron [37]) and a quartz crystal deposition monitor (Inficon [38]). In addition, the preparation chamber also contains a cylindrical mirror analyser (CMA) based Auger electron spectroscopy subsystem (Perkin-Elmer [32]). A detailed

description of the main sample preparation facilities used for the preparation and analysis of samples is given below.

The Resistive Heater

The resistive heater was designed by C. Kempf. A schematic of the resistive heater set-up can be seen in figure 2.6. It also acts as a sample stage for Ar^+ ion etching and thin film deposition. It consists of an alumina crucible with a spiral groove machined along its circumference, along which a $\phi = 0.2$ mm W wire is wrapped. The sample holder sits inside a Ta insert, which fits inside the crucible. The sample holder consists of a Ta cap that screws onto a Mo body. Both the crucible and the Ta insert have concentric apertures machined in their bases to facilitate film depositions. The sample can be inserted face-down for film depositions, or face-up for Ar^+ ion bombardment. The crucible fits inside a stainless steel can, which is attached to a feedthrough for the quartz crystal monitor. This feedthrough comprises two water cooling pipes and a BNC feedthrough to carry the signal from the in-situ quartz crystal to the ex-situ monitor. A separate feedthrough carries the connections to the heater filament and a K-type (Omega) thermocouple which is spot-welded to the Ta insert. This thermocouple allows calibration of the resistive heater each time the W filament is replaced. The heater is calibrated for temperature (K) versus filament power (W), with the thermocouple placed in a sample-holder mounted face-down in the heater. Samples can be heated in a temperature range of $\sim$ 350 K to $\sim$ 900 K using this heater.
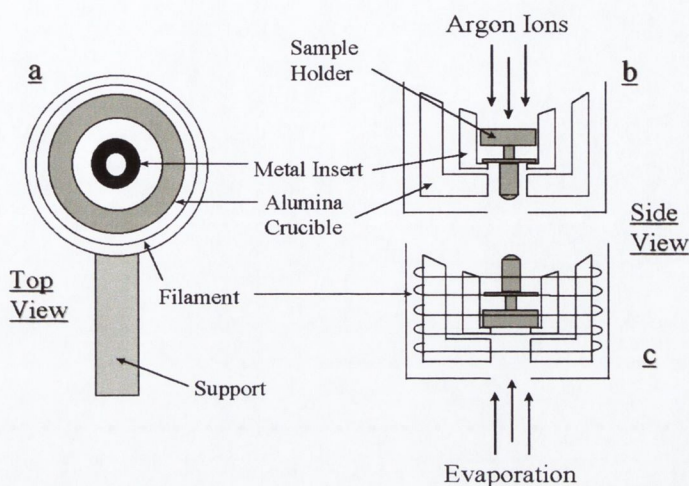
Figure 2.6: Schematic illustration of the resistive heater. The sample can sit face-down in the heater for evaporation experiments. Alternatively, the sample (or tip) is inserted face-up for ion-etching. Reproduced from [39].

The e⁻-beam Heater

The preparation chamber is also equipped with an electron beam heater, for higher temperature preparation procedures. The electron beam heater was designed and assembled by Dr. J. Osing [29]. The sample holder is mounted into a Ta stage which is held at a potential of +1 kV. A current ($1.5 \text{ A} \leq \text{I} \leq 4.5 \text{ A}$) is passed through a grounded thoriated tungsten filament ($\phi = 0.15$ mm, 1 % Th), which generates thermionic emission of electrons. These electrons are accelerated towards the cap of the sample holder, whereupon collision, their kinetic energy is transferred to the sample as heat. Because the filament is situated to one side of the sample there is a temperature gradient across the sample. Surface temperatures are measured from outside the chamber using an infra-red pyrometer (Altimex UX-20/600 [40]) operating in the 1 μm range, which gives a transmission of 95%

through the Kodial window. Due to the low annealing temperatures neccesary for the samples in this study the e$^-$-beam heater was not generally used.

The Ar$^+$ Ion Gun

The preparation chamber is fitted with an inert sputter ion source (PSP vacuum technology [41]) for Ar$^+$ ion etching of STM tips and in-situ cleaning of samples. There are two tungsten filaments, through which typical filament currents of 2.6 A run. The argon gas is introduced through a leak-valve, directly into the gas-cell of the ion-gun, and ionised by electron bombardment. A bias voltage of 0.5 to 2 keV is applied to the sample or tip to be sputtered. Discharge currents vary from 30-40 mA. The target diameter is taken as 11 mm, which is the diameter of the circular Ta insert in the resistive heater, into which the sample/tip is mounted for ion-etching. This insert is isolated from ground by the surrounding ceramic crucible. The thermocouple spot-welded to this insert allows the target current to be measured. This is typically of the order of $8.0 \leq I \leq 20.0$ μA for a 0.5-2 keV beam energy and an Ar pressure of 6.65×10^{-6} mbar.

The Triple Evaporator

Thin film depositions are performed using an Omicron EFM3T UHV triple evaporator, with integral flux monitor [37]. This is a three cell electron beam evaporator. The evaporant can be evaporated from an ultrapure metal rod, or from a crucible containing small pieces of the desired material. The evaporation of the source is achieved by electron bombardment heating, whereby the bombarding electron beam induces a temperature rise of the source. The instrument allows high precision sub-monolayer or multi-layer deposition. The

flux monitor consists of an ion collector at the beam exit column. At a given electron emission current and e^--beam energy, the ion flux measured is directly proportional to the flux of the evaporated atoms. A shutter is present at the beam outlet, allowing precise control of evaporation times. The evaporation cell itself is contained in a water-cooled copper cylinder which, along with the highly localised heating of the evaporant, helps maintain UHV conditions during evaporation.

2.2.2 Auger Electron Spectroscopy Set-up

The Auger analyser is a cylindrical mirror analyser (CMA, model 10-155A Physical Electronics [32]). A schematic of the Auger analyser is seen in figure 2.7. The primary electron beam is generated from a hot filament source, and accelerated through a potential V_2. The beam current can be varied by changing the extraction potential V_1. The electron gun is within two concentric cylinders. The inner cylinder is grounded, while a deflecting potential is applied to the outer cylinder. The deflecting potential is chosen such that only electrons of a particular energy will pass through the exit aperture. The analyser current is given by the number of electrons that pass through this aperture. Between the exit aperture and the collector an electron multiplier is used to amplify the analyser current. Primary electrons of known energy, which are reflected from the sample surface, are used to optimise the signal intensity to find the analyzed spot, and calibrate the analyser. A full description of the operation of the Auger analyser can be found in [15]. A beam energy of 3 keV was used for all measurements. The filament and emission currents were 3.2 A and 0.4 mA respectively, giving a target current of ~ 8 μA. A SR 850 DSP lock-in amplifier from Stanford Research Systems [42] was used to output a 0.5 V_{rms} sinusoidal signal of frequency 12 kHz to modulate
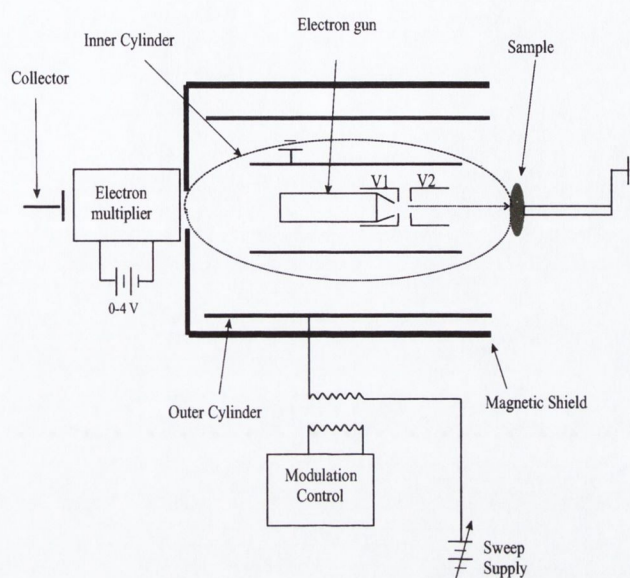
Figure 2.7: Schematic of cylindrical mirror Auger analyser

the deflecting voltage applied to the outer cylinder. A lock-in sensitivity of $100\ \mu V$ was then used to detect the Auger signal. The scan speed was always set at $1\ eV.s^{-1}$.

2.2.3   Low Energy Electron Diffraction Set-up

The RVLO 900 four-grid reverse view optics used in the experiments described here were manufactured by VG Microtech [43]. The optics are mounted on a O.D. 200 mm CF custom elbow which is tilted at an angle of 30° to the horizontal. The sample sits in the transfer fork of a magnetic drive, which is grounded by a stainless steel braid to an OFHC copper block at the bottom of the LEED annex. The sample is rotated in this drive so that its surface faces the electron gun. Scattered electrons are collected by the grids and screen located behind the gun.
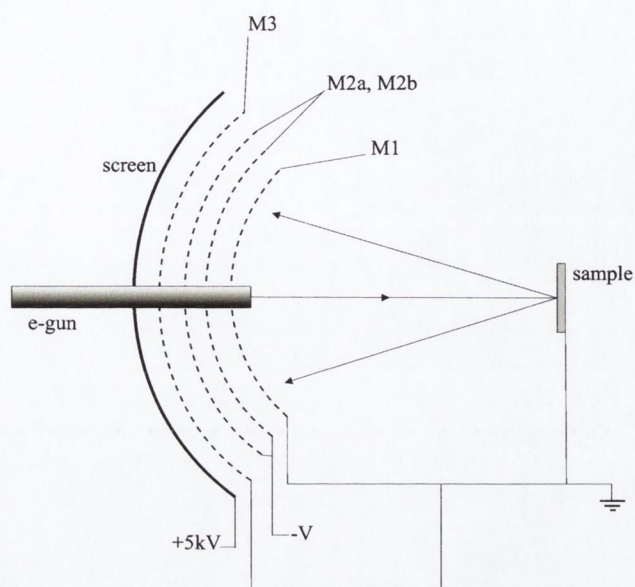
Figure 2.8: Schematic of four-grid optics operating in LEED mode (*c.f.* reference [17]).

A schematic illustration of a four-grid LEED apparatus is shown in figure 2.8. It consists of an electron gun, providing a collimated beam of electrons, and a hemi-spherical fluorescent screen on which the diffracted electrons are observed. The grid nearest the sample, M1, is earthed, so that electrons scattered by the sample initially travel in field-free space. A negative potential is applied to the two centre grids, M2a and M2b, to suppress inelastically scattered electrons, while elastically scattered electrons are accelerated towards the phosphorescent screen by its +5 keV potential. The fourth mesh M3 is also grounded to reduce the field penetration of the suppressing grids by the screen.
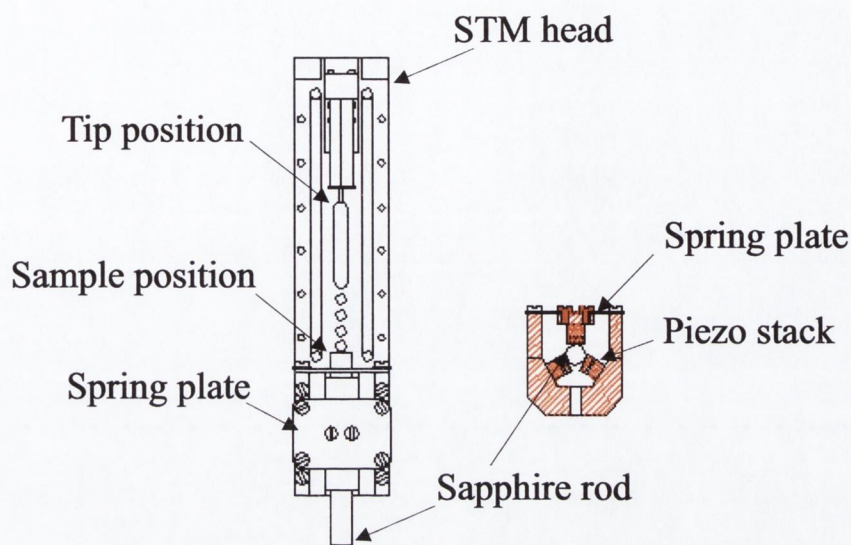
Figure 2.9: Schematic representation of a STM head similar to the RTSTM used. A front view and cross-section of the fine approach walker are shown.

2.2.4   STM Design and Operation

The room temperature STM head is constructed of macor and comprises of a piezo tube scanner and a fine approach walker [Fig.2.9]. It is based upon the system developed by Dr. S.H. Pan at the University of Basel, Switzerland [44]. In this design the sample is mounted on top of a cylindrically polished sapphire rod. The rod is clamped between a set of six piezo stacks, mounted in a triangular fashion. One pair of piezo stacks is spring-loaded against the sapphire rod. The motion of the sapphire rod occurs in two steps. First the stacks rapidly shear simultaneously so that the rod remains fixed as the stacks slip along the rod. All six piezo stacks are then allowed to relax simultaneously, such that the rod is dragged in the direction opposite to the original shear direction.

The piezoelectric tube scanner has four separate electrodes, of equal area,

parallel to the axis of the tube. The inner electrode is grounded, so that when a voltage is applied to one of the outer electrodes the tube scanner bends away from that electrode. The scanner has a dynamic range of $\pm$ 13000 Å in the z-direction and $\pm$ 20600 Å in the x- and y- directions. These directions were calibrated on Cu(100) monatomic steps and HOPG atomic resolution images respectively. The STM head is isolated from vibrations by a two-stage spring system [28] which works in conjunction with the pneumatic dampers on the system frame.

For the STM used in this study the junction bias voltage is applied to the sample. Therefore stated junction bias values, V_b, are for the sample with respect to the tip. The STM controller used for these experiments is a SCALA system by Omicron [37]. This controller allows the user to compensate for the thermal drift using a topographic feature of the STM image as a reference point. The accompanying software provides functions for data analysis. Data was also analysed using commercial software from Nanotec Electrica S.L. [45]

2.2.5 STM Tips

Atomically sharp and stable tips are vital in order to obtain atomic scale resolution using STM. For this reason tungsten is the most widely used material for tip preparation. It is relatively hard, making it a stable probe material, and it can be electrochemically etched, allowing the preparation of atomically sharp tips [19].

For SPSTM, described in section 2.1.3, it is necessary to use a material with a spin split DOS. Initial studies used bulk ferromagnetic tips [46]. However, the stray magnetic field of these materials can alter the magnetic properties of the sample one is attempting to characterise. One method to prevent this is the evaporation of thin films of magnetic material onto W

tips. However, this does not generally result in atomically sharp probes. The other is the use of antiferromagnetic materials, such as Cr or MnNi, which do not have a stray field [47]. STM was performed with tips prepared from a range of materials in the course of this work; tungsten, platinum iridium, manganese nickel and chromium. Except where stated the STM images in this thesis were obtained with W tips. Tips were usually prepared using a chemical etching procedure and their preparation is described in detail in [48].

W Tips

These tips are prepared from $\phi = 0.5$ mm W wire. The wire is cut into small rods and a small insulating layer, a PTFE tube, is place on the end of the rod. The rod is then clamped into a modified micrometer screw, which allows precise positioning of the rod in a beaker of 2.0 M NaOH solution. The W wire acts as the anode while a submerged metal foil acts as the cathode. Under an applied 4 V dc bias chemical etching occurs at the air/electrolyte interface. The W oxidises to form soluble WO_4^{2-}, which flows away from the active etching region. This leads to a thinning of the wire at the interface region, and eventually the submerged section of the wire falls off under it own weight. During the etching process the PTFE acts to physically restrict the active etching region [49] and also protects the tip that falls into the beaker [50]. This tip etching setup is shown in figure 2.10. The tips are then rinsed with propanol-2-ol, placed in tips holders and inserted into UHV. The tips are then etched with Ar^+ ions to remove the WO_4^{2-} present from the chemical etch process. This process produces stable, atomically sharp tips.
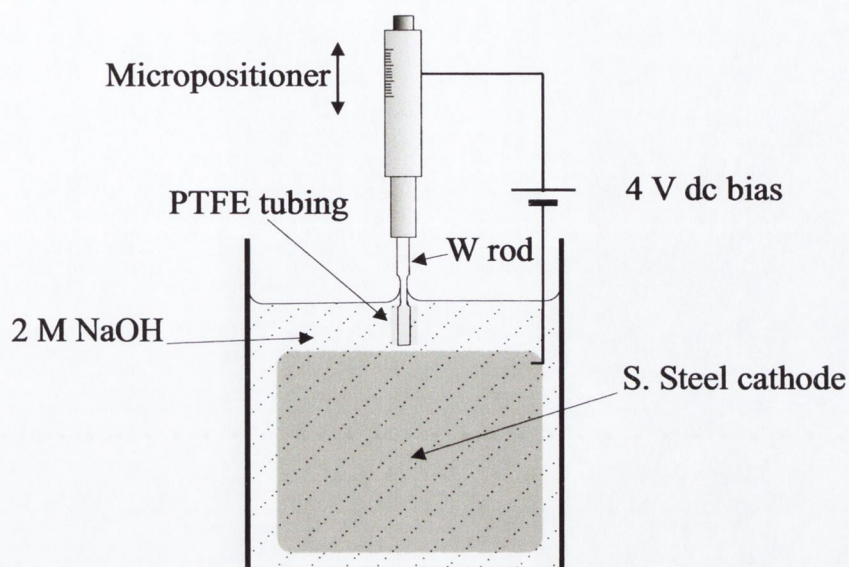
Figure 2.10: Electrochemical etching set-up used to prepare STM tips from W, MnNi and Cr rods.

PtIr Tips

Platinum Iridium tips were prepared by mechanical shearing of a $\phi = 0.25$ mm $Pt_{80}Ir_{20}$ wire. The wire is pulled and cut simultaneously using snips. PtIr does not oxidise and does therefore not require in-situ UHV Ar^+ ion etching. This method does not result in the same reproducibility as chemical etching and these tips were mainly used for testing of microscopes in air.

MnNi Tips

MnNi tips were prepared in a manner similar to that described for W. Cylindrical rods, of roughly $\phi = 0.5$ mm are prepared from an ingot. They are then chemically etched, again using PTFE tubing, in 0.5 M HCl solution. Following chemical etching they are inserted into UHV and subjected to Ar^+ ion bombardment. These tips are again very sharp and stable. MnNi has a

very high Néel temperature of ~ 900 K, meaning it is suitable for room temperature SPSTM experiments. The main problem that arises with the use of MnNi tips is that the composition of the apex is uncertain [51]. For example, the electrochemical etching could be preferential to one of the elements, resulting in a Mn or Ni rich apex. Magnetic contrast has been achieved using these tips on the well characterised Mn/Fe(001) system [51].

Cr Tips

Cr tips were etched, again using the PTFE insulation method, using 2 M NaOH solution. The cylindrical rods were prepared from a high purity Cr ingot. Again, sharp tips (50-100 nm tip apexes), with a low aspect ratio, were obtained. The fact that elemental Cr is used for these tips removes the problem of identifying the tip apex composition, however the low Néel temperature of this material makes it more suitable for experiments below room temperature.

Chapter 3

Magnetite (001)

3.1 Introduction

Magnetite, Fe_3O_4, also known as lodestone, is the oldest known magnetic material [52]. It exhibits a metal-insulator transition, known as the Verwey transition, at $T_v \sim 120$ K [53,54], which has led to much research into understanding the nature of this transition [55]. Furthermore, interest in magnetite has intensified recently due to the fact that its conduction electrons are expected to be 100% spin polarised, even at room temperature [9]. This spin polarisation of the charge carriers means that magnetite is a candidate material for devices that exploit the spin of the electron, such as magnetic tunnel junctions, a field which has seen much recent interest [56,57]. This chapter explains the structure and properties of magnetite, and gives an overview of recent work.
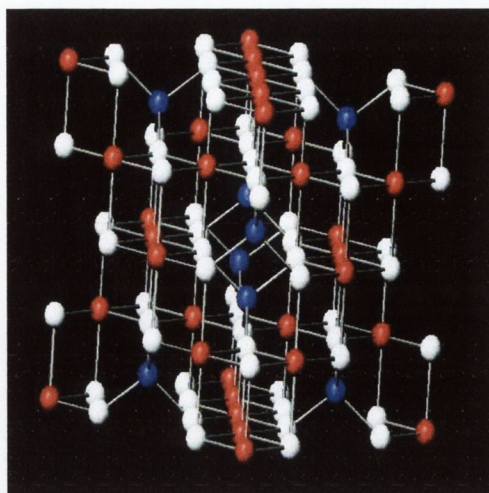
Figure 3.1: Ball and stick model of the magnetite unit cell. The blue ions represent Fe^{3+}_{tetra} cations, the red $Fe^{2.5+}_{oct}$ cations, and the white O^{2-} anions. It can be seen that the structure forms alternating planes of octahedrally and tetrahedrally co-ordinated Fe ions.

3.2   Bulk Structure

Magnetite crystallises in an inverse spinel structure, containing 32 O^{2-} anions arranged in a face centered cubic lattice. This O^{2-} lattice results in the formation of 64 tetrahedral interstices (denoted A-sites) and 32 octahedral interstices (denoted B-sites). Consecutive A- and B- planes are separated by 1.05 Å. Fe^{3+} cations occupy 8 of the 64 A-sites, whereas the B-plane forms a mixed valence plane with 8 Fe^{2+} ions and 8 Fe^{3+} ions. The unit cell has a lattice constant of 8.3963 Å. The Fe ions of the octahedral plane form rows running along the <110> directions. These Fe_{oct} ions have a periodicity of 3 Å along these directions, and the rows that they form are separated by 6 Å. The direction of these Fe rows rotate by 90° between successive octahedral planes. The tetrahedral plane has a four fold symmetry. The Fe ions of the

A- and B- planes are arranged in a ferrimagnetic order, with the spins of the Fe^{3+} ions on the A-plane antiparallel to the spins of the Fe^{2+} and Fe^{3+} ions on the B-plane.

3.3 The Verwey Transition

The Verwey transition is a class of metal insulator transition, classified as a spontaneous intercorrelated change of both lattice symmetry and electric conductivity in certain ionic crystals at a critical temperature. It was first observed in magnetite [53,54]. Magnetite has a relatively high conductivity at room temperature ($\sim 200~\Omega^{-1}cm^{-1}$) which is attributed to the ability of electrons to hop between the Fe^{2+} and Fe^{3+} sites of the octahedral planes. This electron hopping is frozen out at low temperatures, and at 120 K magnetite undergoes a metal-insulator transition where the electron hopping is completely inhibited and the crystal symmetry is lowered [53,54]. It was generally thought that the transition leads to an ordering of the Fe^{2+} and Fe^{3+} ions on the octahedral sites, although the exact nature of this ordering was not agreed upon. Originally, Verwey proposed that the Fe^{2+} and Fe^{3+} ions occupied alternate planes. Later studies demonstrated that ordering of the Fe^{2+} and Fe^{3+} cations on the same octahedral planes is more likely. Nuclear magnetic resonance [58,59], high energy transmission electron diffraction [60], and high resolution neutron and synchrotron x-ray powder diffraction experiments [61] all found evidence for two structurally distinguishable B-sites below T_v. However, recent x-ray resonant scattering studies by Garcia *et al.* [62] and Subias *et al.* [63] provide evidence that, below T_v, charge ordering of the Fe ions does not in fact occur and suggest that a charge disproportionation of at most 25% occurs. They suggest that the entire concept of the transition as

an electronic ordering of the Fe_{oct} ions needs to be reconsidered, and that it is better explained in terms of a condensation of phonons [63]. They specifically disagree with models that suggest a complete disproportion of charge into Fe^{2+} and Fe^{3+} ions, such as the original Verwey model, and the later patterns proposed by Mizoguchi [59]. Further evidence of this idea is given by the fact that more recent NMR studies by Mizoguchi [64] have found evidence for 16 distinguishable Fe_{oct} sites in the magnetite unit cell below T_v. It is clear that despite decades of intensive research the electronic properties of magnetite, and in particular the mechanism of the Verwey transition, are still not well understood.

3.4 Half Metallic Ferromagnet

Much of the recent interest in magnetite centres on the fact that it is predicted to be a half metallic ferromagnet, with 100% spin polarisation of the charge carriers at E_f [Fig. 3.2]. Augmented plane wave (APW) calculations by Yanase and Siratori [9] show a gap in the majority spin band at E_f, but no such gap in the minority spin band. Later band structure calculations using the local spin density approximation by Zhang and Sathapy [65], generally agree with the earlier APW calculations. The calculated DOS from reference [65] is shown in figure 3.3. It shows the majority spin up band to be semiconducting, whereas the minority spin down band is metallic, at E_f. Only spin down electrons, occupying the t_{2g} level, are present at the Fermi level, and these have a predominantly Fe(B) character. It is also evident that the O_{2p} levels lie far below the Fermi level.

Both calculations are in agreement with earlier photoelectron spectroscopy (PES) experiments by Alvarado [66]. Experimental data, more re-
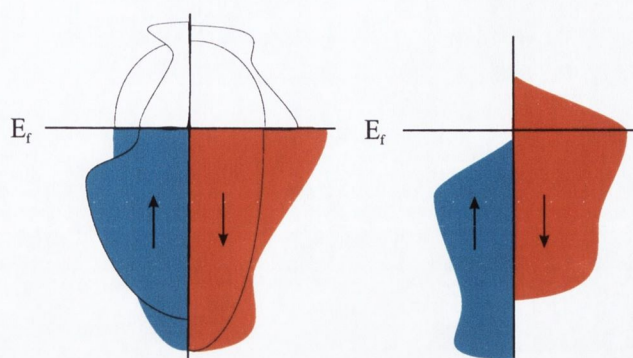
Figure 3.2: Left: Schematic of total density of states for a ferromagnet. Spin polarised 3d electron are present at the Fermi level, along with unpolarised 4s electron. Right: Schematic density of states of a half metal, only one spin polarised sub-band is occupied at the Fermi energy.

cent than the PES experiments of Alvarado, also support the half metallic nature of magnetite suggested from these band structure calculations. Dedkov *et al.* have performed PES on epitaxial magnetite (111) on W (110) at room temperature [67]. The spectra obtained were found to be in general agreement with the aforementioned calculations. A spin polarisation of -80 $\pm$ 5% was found near the Fermi energy. A similar experiment, by the same group, for magnetite (111) on Al_2O_3, found a slightly smaller value of $\sim$ - 65% spin polarisation [68]. Furthermore, devices have been fabricated, using magnetite electrodes, that confirm some degree of spin polarisation, although much less than the predicted 100%. For example, the magnetoresistance of epitaxial trilayer junctions composed of magnetite and doped manganite $La_{0.7}Sr_{0.3}MnO_3$ have been shown to exhibit an inverse magnetoresistance, consistent with a negative spin polarisation of 25% [69].
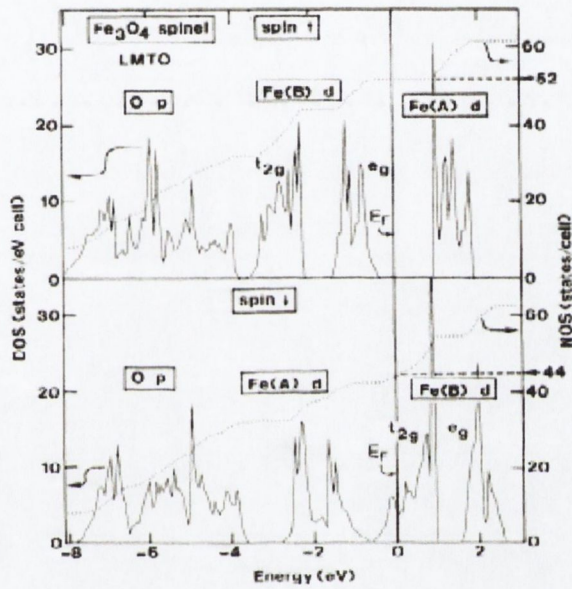
Figure 3.3: The calculated DOS of magnetite, from reference [65]. It can be seen that only spin down electrons of the t_{2g} level are present at the Fermi level, resulting to 100% spin polarisation of the electrons at E_f. It is also seen that the O_{2p} levels lie far below E_f.

(a): Ideal tetrahedral termination   **(b): Ideal octahedral termination**

● Fe³⁺ tetrahedral (surface plane)

○ Oxygen (second plane)

○ Fe²·⁵ octahedral (second plane)

○ Fe³⁺ tetrahedral (third plane)

○ Oxygen (surface plane)

○ Fe²·⁵ octahedral (surface plane)

○ Fe³⁺ tetrahedral (second plane)
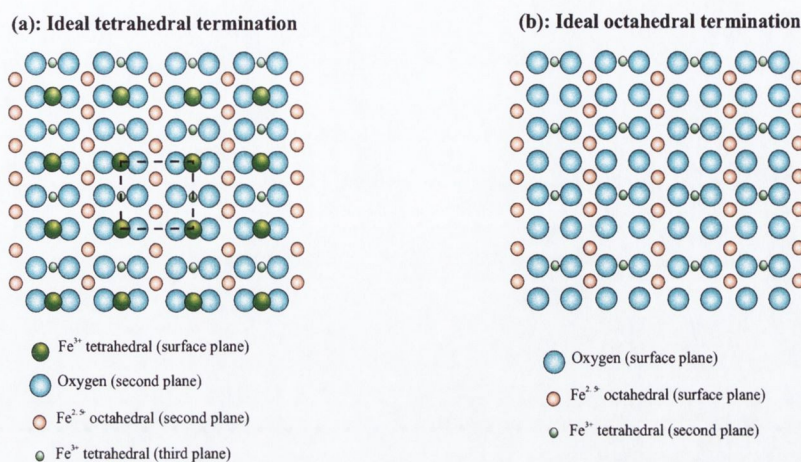
Figure 3.4: Ideal, unreconstructed, magnetite (001) surface terminations. Left: Tetrahedral termination, consists solely of Fe^{3+}_{tetra} cations. Right: Octahedral termination. This termination is a mixed plane of $Fe^{2.5+}_{oct}$ cations and O^{2-} anions. The (6×6) Å^2 surface unit cell of unreconstructed magnetite (001) is shown by the dashed square.

3.5 The Fe_3O_4(001) Surface

3.5.1 Ideal Tetrahedral and Octahedral Terminated Surfaces.

The work presented here concentrates on the (001) surface of magnetite. Along the <100> direction, the crystal can be considered as a stack of two alternating layers. This can be seen from the ball and stick model of the crystal, in figure 3.1. Ideally the crystal can terminate at either of two bulk planes. The A-plane, containing only Fe^{3+} ions in tetrahedral interstices or the B-plane, containing $Fe^{2.5+}$ cations and O^{2-} anions. These ideal bulk terminated planes are shown in figure 3.4. However, magnetite (001) is a polar

surface, which means that these bulk terminations are not stable against reconstruction.

3.5.2 The Electrostatic Model of Polar Surfaces

The electrostatic model of polar surfaces was proposed by Tasker and provides a classification of crystal surfaces which allows one to determine whether or not they will reconstruct [70]. Within this model, which applies to ionic or partially ionic crystals, there are three surface types, which are illustrated in figure 3.5.

The crystal is visualised as being built up from repeat planes perpendicular to the surface. Type I is neutral, having equal numbers of anions and cations of the same charge in each repeat plane. The repeat units have zero charge, σ, and zero dipole moment, μ. Type II surfaces have a non-zero charge in the repeat unit, but due to the symmetrical stacking sequence of the repeat unit have zero dipole moment. Type III surfaces have a non-zero charge and also have a non-zero dipole moment in each repeat unit of the crystal. Type III surfaces therefore have a diverging electrostatic surface energy. Such a surface is not stable, in an ideal bulk termination, and must reconstruct. The surface reconstruction is such that the charge of the surface plane is halved, resulting in the cancelation of the electrostatic energy due to the surface layers. This is achieved through the formation of an ordered array of vacancies on the surface. There are two other possibilities for the cancellation of surface polarity; surface contamination, or a compensation by electron redistribution in response to the electrostatic field. Surface relaxations alone do not suffice to cancel the field [71].

Within the electrostatic model, magnetite (001) is classified as a type III crystal. Using $(\sqrt{2} \times \sqrt{2})R45°$ surface unit cells the repeat unit consists of
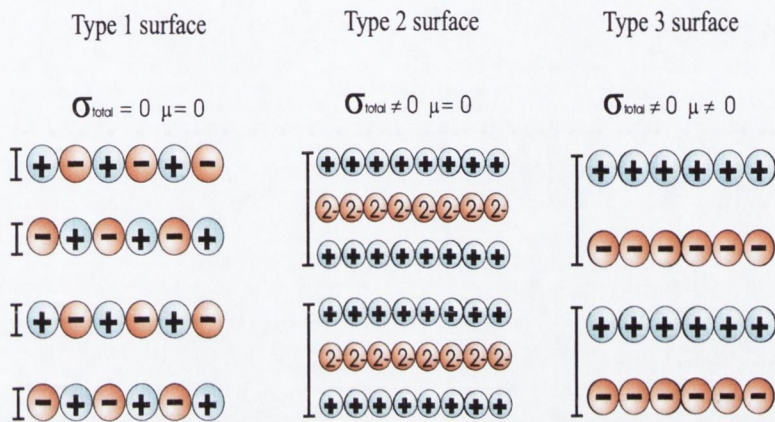
Figure 3.5: The electrostatic model of polar surfaces. Repeat unit of each denoted by a bracket. Type 1; repeat unit contains equal numbers of anions and cations in a single plane, each plane has zero charge. Therefore no net dipole moment. Type 2; planes are charged, however as they are in a symmetrical configuration there is no net dipole moment perpendicular to the planes. Type 3; planes are charged and repeat unit is not symmetrical. Therefore each repeat unit has a net dipole moment perpendicular to the surface.

a tetrahedral unit cell plane, which has an overall charge of + 6, and an octahedral unit cell plane that has an overall charge of - 6. Therefore, each repeat unit that forms the crystal has a non-zero dipole moment. As the crystal is built up, the electrostatic energy due to the surface diverges and the surface energy becomes infinite. To fully cancel this electrostatic field the surface layers only must reduce their charge to + 3 for a tetrahedral termination, or - 3 for an octahedral termination. Therefore the surface must reconstruct.

3.6 Previous Studies of Magnetite (001) Using Surface Sensitive Techniques

The (001) surface of magnetite has been extensively studied using surface sensitive techniques, AES [72], low energy ion spectroscopy [73], X-ray photoelectron spectroscopy (XPS) [66], spin resolved PES [67,68], angle-resolved PES [74] and STM [46,75–83]. Recently, DFT calculations have been carried out to ascertain the most favourable surface termination [84,85].

3.6.1 Topographic STM Studies

For STM studies of the clean surface, the $(\sqrt{2} \times \sqrt{2})R45°$ reconstruction is by far the most widely reported [73, 76–83]. However, there is disagreement between these studies as to whether the surface is tetrahedrally or octahedrally terminated. Tarrach *et al.* [76], Gaines *et al.* [78, 79] and Chambers *et al.* [81] have proposed that the surface imaged is best explained in terms of a tetrahedrally terminated surface, with a $(\sqrt{2} \times \sqrt{2})R45°$ array of Fe vacancies. The array of vacancies is explained as resulting from the surface

reconstructing to lower its polarity. However, the studies by Voogt *et al.* [77], Stanka *et al.* [80], Koltun *et al.* [82], and Mariotto *et al.* [83] all show surfaces that are best explained in terms of octahedral termination. Again, due to electrostatic considerations, this termination is most often explained in terms of a surface with a $(\sqrt{2} \times \sqrt{2})R45°$ array of O^{2-} vacancies. It is also worth noting that both Koltun *et al.* and Mariotto *et al.* suggest that the surface is in fact a bulk octahedral termination, and that a charge ordered dimer formation gives rise to the $(\sqrt{2} \times \sqrt{2})R45°$ symmetry.

3.6.2 Spin Polarised STM Studies

As already seen in section 3.4, recent spin resolved PES experiments [67, 68] show that the observed spin resolved DOS at E_f are consistent with the surface of magnetite having a half metallic nature. This spin polarisation of the charge carriers suggests that magnetite is a suitable surface for spin polarised STM experiments. Furthermore, as maintenance of a high degree of spin polarisation at the surface is essential for future devices, studies that improve understanding of the electronic and magnetic structure of the surface are vital. In what was one of the first SPSTM experiments, Wiesendanger *et al.* [46, 75] imaged the (001) surface of magnetite with both W and Fe tips. When scanning with a W tip they observed a 3 Å periodicity along the Fe rows, consistent with bulk termination. However, when scanning with a Fe tip they instead observed a 12 Å periodicity along the rows. This imaging of a non bulk periodicity with a ferromagnetic probe was explained as follows; the bulk 3 Å periodicity is replaced by a 6 Å periodicity due to the formation of Fe^{2+}-Fe^{2+} and Fe^{3+}-Fe^{3+} dimers along the rows. Tunneling with the Fe tip results in an extra spin-down ($\downarrow$) contribution to the tunnel current when tunneling from the Fe^{2+}-Fe^{2+} dimers, thus replacing the expected 6 Å

periodicity with the imaged 12 Å periodicity. This experiment was recently repeated by Koltun *et al.* [82] and again a 12 Å periodicity was imaged with a Fe tip. However, attempts to image the surface with W tips were unsuccessful. This result was again explained in terms of dimer formation and an enhanced imaging ability of the Fe tip, due to spin polarised tunneling, in agreement with the experiment of Wiesendanger *et al.*. Finally, in the study by Mariotto *et al.* [83], mentioned in the previous section, the surface was imaged with MnNi tips. Fe dimers were once again imaged on the surface, said to be consistent with the formation Fe^{2+}-Fe^{2+} and Fe^{3+}-Fe^{3+} dimers along the Fe rows. Once again, the surface was not imaged with non-magnetic tips for comparison.

3.6.3 DFT Calculations

A recent addition to work on the magnetite (001) surface has been first principle calculations, within density functional theory (DFT) [84, 85]. Cheng studied 4 possible surface terminations of $Fe_3O_4(001)$ [85]. These are unreconstructed A-plane, A-plane with a $(\sqrt{2} \times \sqrt{2})R45°$ array of Fe^{3+} vacancies, unreconstructed B-plane, and finally B-plane with a $(\sqrt{2} \times \sqrt{2})R45°$ array of O^{2-} vacancies. This study found that the latter two, an unreconstructed B-plane termination, and a B-plane with a $(\sqrt{2} \times \sqrt{2})R45°$ array of oxygen vacancies, are both more energetically favourable than either A-plane termination. Furthermore, it was found that both the unreconstructed B-plane and B-plane with O_{vac} terminations decrease their energy in an O rich environment, with the unreconstructed surface becoming more favourable in O rich atmospheres. This result is not reconciled with the theory of polar surfaces.

In a similar study, Pentcheva *et al.* have investigated the possibility of a

stable bulk surface termination [84]. This study again suggests that a bulk octahedral (B-plane) termination is in fact energetically favourable. The study also shows that both B-plane terminations, either with or without oxygen vacancies, are more stable than A-plane terminations. It is interesting to note that both studies show that for B-plane termination, with or without oxygen vacancies, the magnetite surface maintains the half metallic character of the bulk.

It is worth noting that the slab used to model the surface by Cheng consists of 17 atomic layers, and that used by Pentcheva *et al.* consists of 5 B-layers and either 4 or 6 A-layers. In terms of the polar model of surfaces, energy divergence at the surface arises as the number of repeat units with a dipole moment increases [70]. It is therefore unclear as to whether a slab representing only 4-8 repeat units can give rise to energy divergence at the surface. Furthermore, the modelled cells are clearly not charge balance, and therefore their applicability to real magnetite surfaces is questionable.

Chapter 4

Characterisation and Surface Preparation of Magnetite (001) Single Crystal

4.1   Introduction

In this chapter the characterisation of the the single crystal magnetite ingot used in the experiments is discussed. The purity of the crystal is proven by the presence of the Verwey transition. The surface contamination induced due to the diffusion of bulk impurities following annealing in UHV is briefly discussed. Finally, the preparation procedure used to obtain a clean magnetite surface is outlined, and AES and LEED of the clean surface presented.

4.2   Sample Characterisation

The magnetite sample used in this study was grown using the skull melting technique by Prof J. Honig [86]. The crystals were cut along the <010> direc-
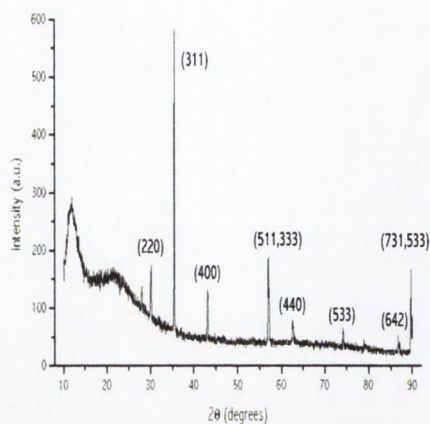
Figure 4.1: X-ray diffractogram of the magnetite single crystal.

tion, aligned to an accuracy of 0.5°. X-ray measurements were taken using a powder diffractometer [Fig. 4.1]. A CuKα wavelength was used, corresponding to $\lambda = 1.541$ Å. The diffractogram obtained was found to be in good agreement with the expected crystalographic structure of magnetite [87].

The most conclusive confirmation that the crystal is actually magnetite is the presence of the Verwey transition. For non-contaminated, stoichiometric, magnetite the transition temperature is found at $\sim$ 120 K. If the crystal is contaminated or cation deficient, $Fe_{(3(1-\delta))}O_4$, the transition temperature is found to be lower [88]. Indeed, for cation deficiency of only δC=0.0039 the transition is found to disappear completely [89]. Through resistivity versus temperature measurements the crystal used in these experiments was found to have a T_v of $\sim$ 110 K, as seen in figure 4.2. This confirms the crystal to be magnetite, but shows it to be slightly substoichiometric, either due to contamination or cation deficiency.
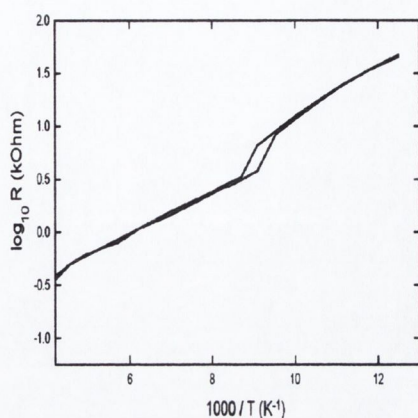
Figure 4.2: The resistivity versus temperature curve for the magnetite single crystal used in these experiments. The Verwey transition temperature T_v is found to be $\sim$ 110 K.

4.3   Initial Annealing: Diffusion of Ca and K

The surface of the magnetite crystal was prepared, ex-situ, by mechanically polishing the sample surface, using diamond paste of decreasing grain size, down to a grain size of 0.1 μm. The sample was then cleaned with ethanol, using an ultrasonic bath. It was then secured in a Ta/Mo sample holder and inserted into the UHV system.

Following insertion into the UHV system, the magnetite (001) sample was initially outgassed at $\sim$ 450 K for 24 hours in the resistive heater. It was then subject to extended periods of annealing in UHV at 800 K. The minimum anneal times were 4 hours, up to a maximum of 80 hours continuous annealing. This results in the diffusion of calcium and potassium contaminants from the bulk of the crystal to the surface [90]. For the crystal used in these studies Ca is by far the largest contaminant. This can be seen from the Auger spectra in figure 4.3, which was taken following 20 hours of annealing at 800 K, in

(a)

(b)

(c)
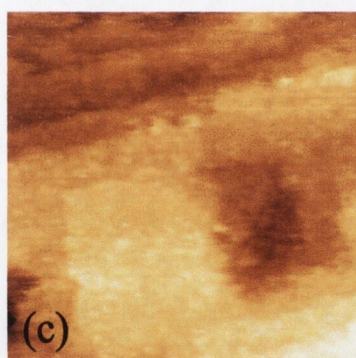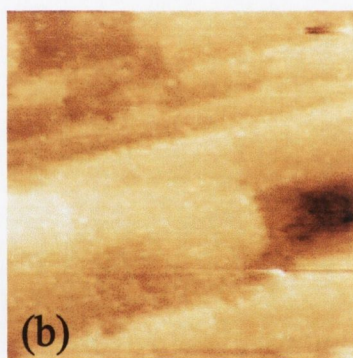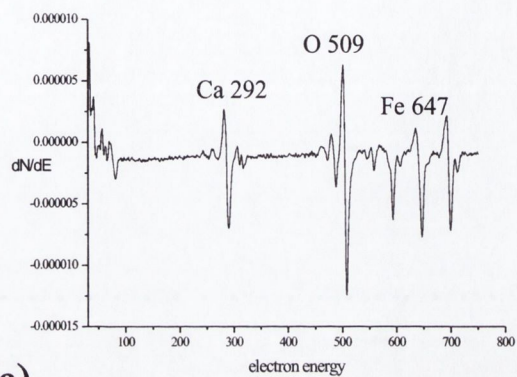
Figure 4.3: (a): Auger electron spectrum of the magnetite surface following initial insertion into UHV and annealing for prolonged periods at ~ 800 K, in UHV. Calcium contaminants diffuse from the bulk, as is evident from Ca concentration of 16% in this spectra. (b) and (c): (120×120) Å^2 and (90×90) Å^2 STM images of magnetite (001) surface with $\sim 10\%$ Ca concentration, as measured in AES. Tunnel current set-point, $I_t = 0.1$ nA and junction bias voltage, $V_b = +1$ V.

UHV. The surface has a 16% Ca concentration. It is clear from this spectra that the most likely reason the crystal has a Verwey transition temperature of 110 K, rather than 120 K as expected for stoichiometric crystals, is the presence of Ca contamination, which suppresses the transition temperature. When such large Ca concentrations are present at the surface it is highly disordered. This is clear from the fact that the surface exhibits either no LEED mesh at all, or at best, faint and blurred (1×1) diffraction spots. STM of the surface also reveals a highly disordered surface. This is evident from the STM images presented in figure 4.3. These images are of a surface with ∼ 10% Ca concentration in Auger spectra. Ill-defined terraces are formed, with evidence of a large concentration of surface contamination.

For lower concentrations of Ca contamination (1∼8%) ordered surface reconstructions can occur. These reconstructions consist of trench-like formations of the Ca contaminants on the terraces of the surface. Ceballos *et al.* [90] have shown that for Ca concentrations of 1-3% a p(1×2) reconstruction occurs, for 3-6% a p(1×3) reconstruction, and for 6-8% a p(1×4) reconstruction. Figure 4.4 shows a LEED mesh and STM image of the magnetite (001) surface with ∼ 6% Ca concentration, as measured by AES. The LEED mesh shows some quarter order spots, indicated by the red arrows. STM shows that terraces are formed on the surface, with edges aligned along the [110] and [1$\bar{1}$0] directions. These terraces are separated in height by multiples of 2.1 Å. As the separation between octahedral and tetrahedral planes is 1.05 Å, the imaged step heights correspond to surface termination at either the octahedral or tetrahedral plane, but not a combination of both. On the imaged terraces rows are formed, as seen in figure 4.5. They are separated by 24 Å and have a periodicity of 6 Å along the rows. As unreconstructed magnetite has a (6×6) Å^2 surface unit cell, the imaged reconstruction corresponds to
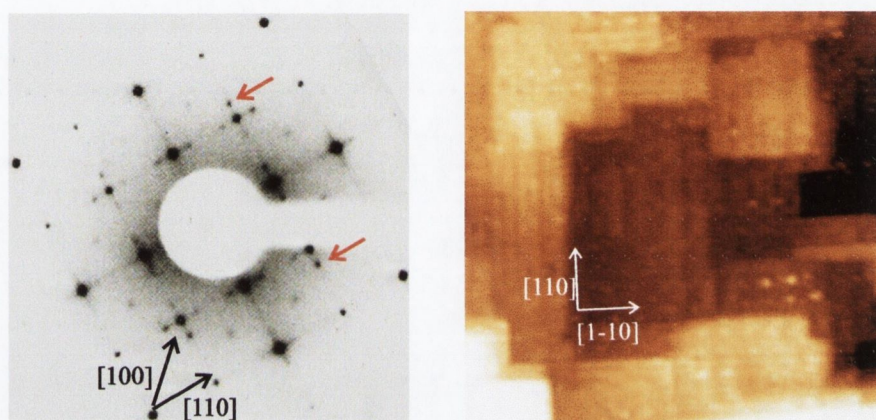
Figure 4.4: LEED mesh of surface with $\sim 6\%$ Ca contamination, quarter order spots are seen, which are indicated by the red arrows. Also shown, a (700×700) Å^2 STM image of the magnetite (001) surface with 6% Ca contamination. $I_t = 0.1$ nA, $V_b = +1$ V. Rectangular terraces, with their edges aligned along the [110] and [1$\bar{1}$0] directions, are formed, on which the initial stages of formation of a p(1×4) surface reconstruction are imaged.

a p(1×4) symmetry. These rows are oriented along the [110] and [1$\bar{1}$0] directions, and have a two fold symmetry. They have an apparent corrugation height of $\sim$ 1 Å. The rows, forming the p(1×4) surface reconstruction, have been attributed to Ca row formation on the magnetite surface [90, 91]. The Auger spectra for such contaminated surfaces show that there is an increase in the oxygen to iron ratio of the surface as the concentration of Ca contamination increases. This has led to the suggestion that the reconstruction results from Ca ions replacing Fe ions, in a (4×1) pattern, at the magnetite surface [91].

4.4 Preparation of Clean Magnetite (001) Surface

It was first reported by Tarrach *et al.* that repeated cycles of Ar$^+$ ion etching an annealing in UHV results in an ordered magnetite surface, free from contamination [76]. The importance of annealing the sample in oxygen to achieve surface order was noted by Stanka *et al.* [80]. To eliminate surface contamination, and prepare the clean magnetite surface for the studies presented here, the sample was prepared as follows. Firstly the sample was annealed in an O_2 atmosphere at 2.66×10^{-6} mbar, at a temperature $\sim$ 800 K, for 30 min. It was then subject to Ar$^+$ ion etching, with an energy of 1 keV, for 15 min. This was followed by annealing in UHV, at $\sim$ 800 K, for periods of between four and twelve hours. The initial oxygen anneal was found to be necessary to maintain the surface O/Fe ratio, and annealing pre rather than post Ar$^+$ ion etching resulted in the most ordered surface. Four hours post etching UHV annealing was found to be the minimum time necessary for good surface order. Initially, following the annealing in UHV step, Ca again
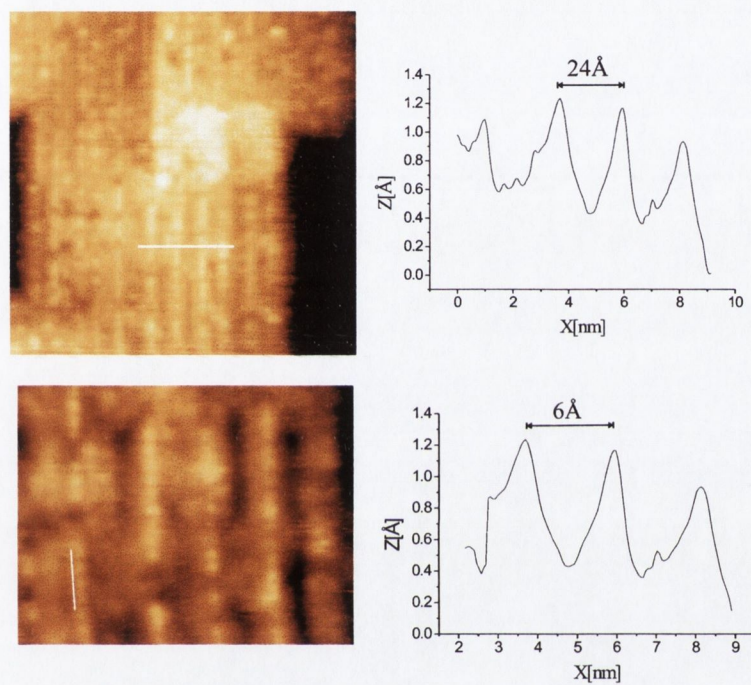
Figure 4.5: Top: (300×300) Å² STM image, I_t= 0.1 nA, V_b= +1 V. Accompanying line profile, shows the 24 Å periodicity across the rows. Bottom: (130×100) Å² STM image, with accompanying line profile, showing the 6 Å periodicity along the rows.
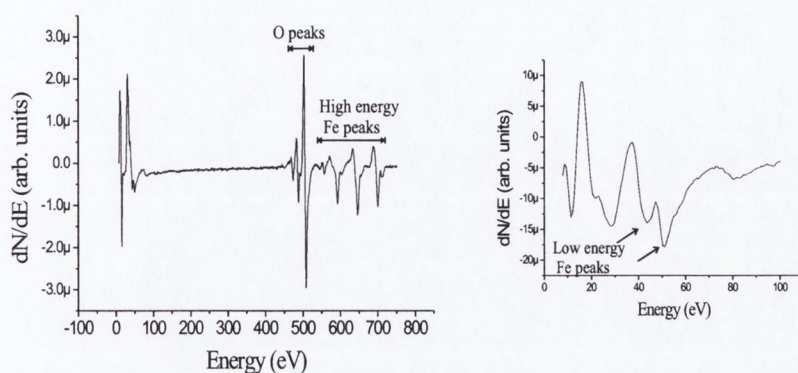
Figure 4.6: Auger spectrum of the surface following the preparation procedure described in text. Only O and Fe peaks are present, with the previous high concentration of Ca gone from the surface following the preparation.

diffused to the surface. However, repeated cycles of this preparation results in a clean surface, with contamination levels below the limit of detection of the AES set-up.

4.4.1 AES and LEED of the Clean Magnetite (001) Surface

An AES spectrum of the clean surface is shown in figure 4.6. The only peaks present are those of O and Fe, with no evidence for Ca contamination of the surface. It has been suggested that the low energy peaks of Auger spectra can be used as an indication of the type of iron oxide present at the surface [72, 92]. Low energy Fe peaks can be seen at 46 eV and 52 eV, with the amplitude of the latter being much larger than the former, consistent with the presence of an iron oxide at the surface. Seo *et al.* [72] suggest that these peaks are indicative of magnetite, however, later work by den Daas *et al.*
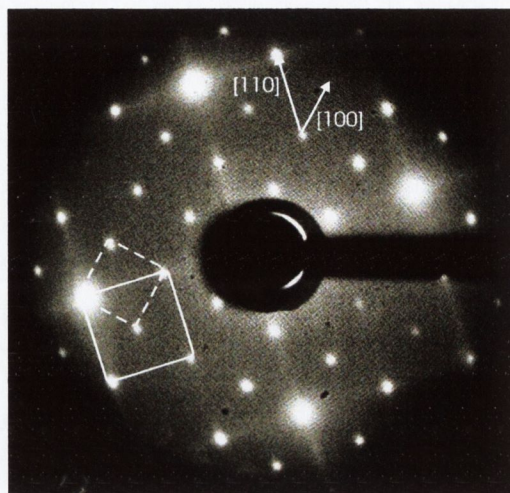
Figure 4.7: LEED pattern of the magnetite surface following the preparation procedure described in the text. The solid square indicates the p(1×1) cell, and the dashed square the $(\sqrt{2} \times \sqrt{2})R45°$ superlattice.

suggest it is not possible to use the low energy Auger peaks to distinguish the oxide type [93]. From Auger spectra, the O/Fe ratio of the $(\sqrt{2}\times\sqrt{2})R45°$ reconstructed magnetite surface is 1.5-1.7.

A typical LEED mesh of the clean magnetite (001) surface is shown in figure 4.7. It is taken using a primary electron energy of 56 eV and an emission current of 0.5 mA. The diffraction pattern shows fractional order spots, forming a $(\sqrt{2}\times\sqrt{2})R45°$ reconstruction. The unreconstructed primitive unit cell for the magnetite (001) surface is (6×6) Å^2, with the reconstructed unit cell being (8.48×8.48) Å^2. This LEED mesh has been observed in numerous studies of the $Fe_3O_4(001)$ surface. Tarrach *et al.* [76], Kim *et al.* [94] Gaines *et al.* [78,79] and Mariotto *et al.* [83] have all observed this pattern for the clean surface of (001) single crystals. Voogt *et al.* [77] observed this mesh for an MBE grown $Fe_3O_4(001)/MgO$ film. As noted in section 3.6.1, there have

been three possible surface structures put forward that would explain the observation of a $(\sqrt{2} \times \sqrt{2})R45°$ LEED mesh. Firstly a tetrahedrally terminated (A-plane) surface, with an array of Fe vacancies. Secondly an octahedrally terminated surface (B-plane) with an array of O vacancies. Both of these models are based on the need of the magnetite (001) surface to reconstruct due to the electrostatic considerations put forward by Tasker [70]. Thirdly, it has been proposed that the surface is not actually reconstructed; that is, there is no $(\sqrt{2} \times \sqrt{2})R45°$ vacancy structure on the surface. Wiesendanger *et al.* [46], Koltun *et al.* [82] and Mariotto *et al.* [83] have all suggested that their STM images are best explained in terms of a charge ordering of Fe^{2+}-Fe^{2+} and Fe^{3+}-Fe^{3+} dimers in a $(\sqrt{2} \times \sqrt{2})R45°$ symmetry. Following the observation of the $(\sqrt{2} \times \sqrt{2})R45°$ LEED mesh, STM was performed on the surface on a number of occasions. The results of this, and a consideration of which model best suits the observed structure, are presented in the next chapter.

Chapter 5

STM of the $(\sqrt{2} \times \sqrt{2})R45°$ Reconstructed Magnetite (001) Surface

5.1 Introduction

In this chapter STM images of the $(\sqrt{2} \times \sqrt{2})R45°$ reconstructed magnetite surface are presented. The surface was imaged with tips made from both antiferromagnetic MnNi and from W. The images obtained with MnNi offer an improved contrast of the surface, possibly due to a spin polarised effect. A model of the surface termination is put forward. Tunneling spectra of surface are presented. Finally, the breakdown of the $(\sqrt{2} \times \sqrt{2})R45°$ reconstruction due to UHV annealing of the sample is discussed.
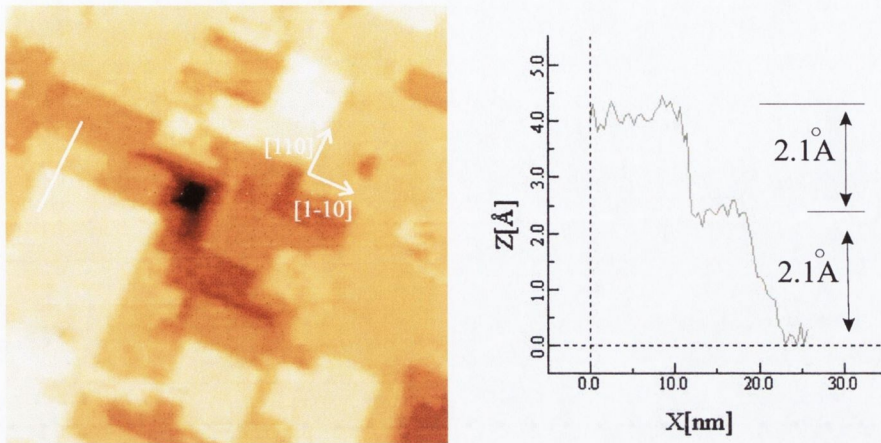
Figure 5.1: (1000×1000) Å² STM image, I_t= 0.1 nA, V_b= +1 V, obtained using W tip. A terraced magnetite (001) surface, following preparation procedure described in section 4.4, is imaged. Large rectangular terraces, with edges aligned along [110] and [1$\bar{1}$0] directions, are formed. All imaged step heights are 2.1 Å, or whole multiples of this.

5.2   Terrace Formation and Surface Termination

STM of the clean magnetite (001) surface, which exhibits the $(\sqrt{2} \times \sqrt{2})R45°$ LEED mesh reveals the formation of large rectangular terraces, with edges aligned along the [110] and [1$\bar{1}$0] directions, as seen in the image of figure 5.1. Step heights are always measured to be multiples of 2.1 Å. During the course of these experiments step heights of 1.05 Å, or odd multiples of this, have not been observed. The fact that only step height multiples of 2.1 Å are measured shows the surface to be terminated at either the octahedral plane, or the tetrahedral plane. The observation of of 1.05 Å step heights is necessary for the surface to be terminated by a mixture of octahedral and
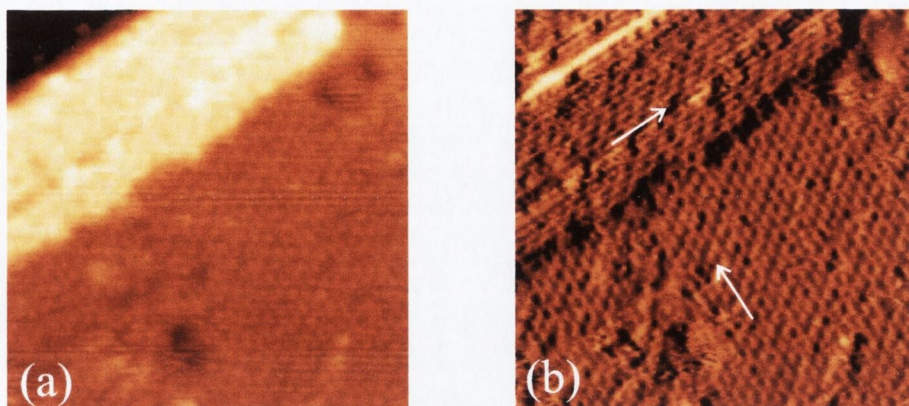
Figure 5.2: (a): (230×230) Å² STM image of magnetite (001) surface, obtained using MnNi tip, I_t= 0.1 nA, V_b= +1 V. The terraces imaged are separated in height by 2.1 Å. (b): Differentiated image showing more clearly that the atomic scale rows imaged on the terraces rotate by 90° from one terrace to the next. This symmetry is best explained in terms of termination at the octahedral plane (B-plane).

tetrahedral terraces. This can be seen by reference to the magnetite unit cell [Fig. 3.1], where the interplane distance is 1.05 Å. It is worth noting that it has been shown, in reference [90], that sample preparation involving annealing in H can give rise to some small terraces with 1.05 Å step heights.

Higher resolution images show atomic scale rows, oriented along the [110] direction, running along the terraces. These rows rotate by 90° on terraces separated by 2.1 Å, and odd multiples of 2.1 Å. Such an image is shown in figure 5.2. PES results, and first principle calculations, consistently show that the Fe ions dominate the DOS at E_f, and that the O_{2p} levels lie far below the Fermi level [9, 65, 66, 74]. This means that the dominant contribution to the tunnel current from magnetite will come from the Fe cations, as STM probes

the states near the Fermi level [19]. Therefore, the imaged atomic rows are Fe ions. The observed rotation of the atomic scale rows is consistent with the 2-fold symmetry of the octahedral rows of magnetite, and therefore indicates the surface to be terminated at the octahedral plane. The tetrahedral plane has a four fold symmetry and so one would not expect to see this rotation of rows between successive planes. Further in favour of surface termination at the octahedral plane is that the density of the imaged atoms, which is too dense to be the tetrahedral plane.

5.3   STM Imaging with MnNi Tips

A higher resolution image of the surface obtained with a MnNi tip, using sample bias of +1 V and tunnel current set-point of 0.1 nA, is shown in figure 5.3. The rows, oriented along the <110> directions, are formed from points of two different intensities, labelled α and β respectively in the figure. This differing intensity is clearly seen in the line profile taken along the $[1\bar{1}0]$ direction, shown in figure 5.3(c).

The α and β points form a $(\sqrt{2} \times \sqrt{2})R45°$ symmetry. The $(\sqrt{2} \times \sqrt{2})R45°$ unit cell is indicated by the dashed white square. Also imaged are local minima or depressions, labelled γ, which also form a $(\sqrt{2} \times \sqrt{2})R45°$ array on the surface. The α and β points are elongated along the [110] direction, and the distance between like points along this direction is 12 Å. From the bulk structure of the octahedral plane of magnetite, the expected periodicity along the Fe_{oct} rows is 3 Å. Therefore, given the large size of the imaged spots, and the doubling of the expected periodicity along the rows, this surface is best explained in terms of Fe-Fe dimer formation along the rows. The α and β points imaged with a MnNi tip represent Fe-Fe dimers in two different
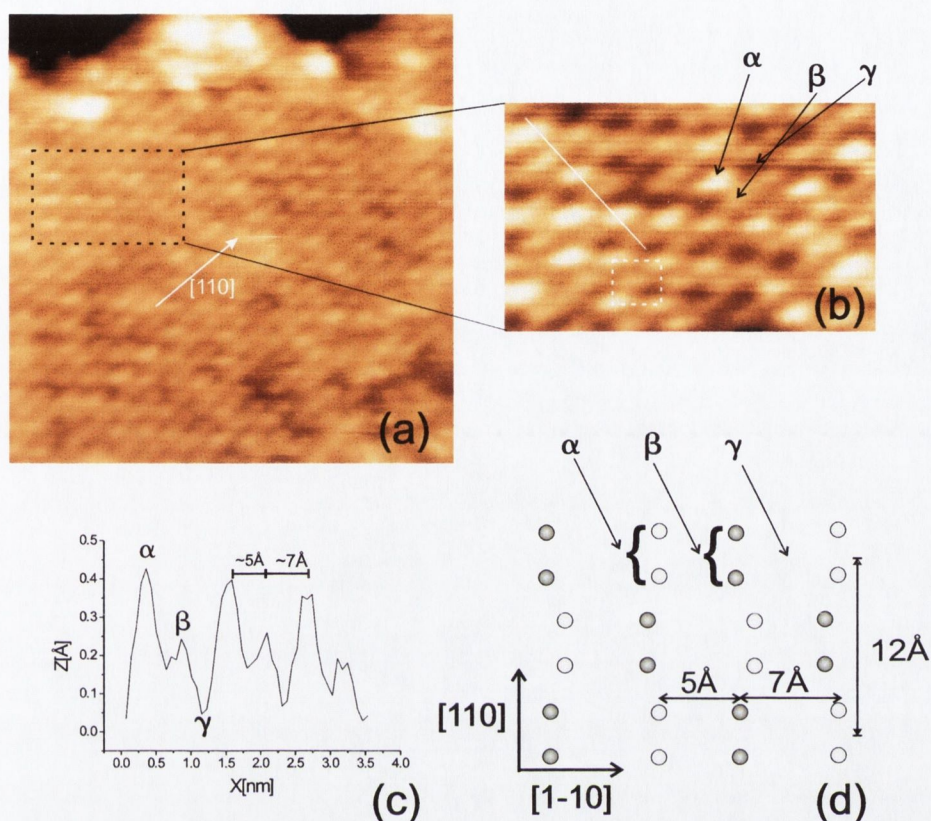
Figure 5.3: (a): (140×140) Å^2 STM image, I_t= 0.1 nA, V_b= +1 V, taken with a MnNi tip, showing the $(\sqrt{2} \times \sqrt{2})R45°$ reconstructed magnetite surface. (b): A (65×45) Å^2 zoom in, showing that spots of two different brightness levels are imaged, corresponding to two different charge states, possibly Fe^{3+}-Fe^{3+}, labelled α, and Fe^{2+}-Fe^{2+}, labelled β. Also imaged is an ordered array of local minima, labelled γ. All three features separately form a $(\sqrt{2} \times \sqrt{2})R45°$ symmetry. The surface unit cell of the structure is indicated by the dashed square, with a length of 8.4 Å. (c): Line profile along the solid white line in the STM image, illustrating the alternating periodicity, of 5 Å and 7 Å, along the $[1\bar{1}0]$ direction. This results in the Fe rows having a wavelike structure. (d): Schematic of the arrangement of the Fe ions as imaged with MnNi tips. The white spheres represent Fe^{3+} ions and the grey spheres Fe^{2+} ions.

charge states. Given that the formal charge of an Fe_{oct} ion in magnetite is $Fe^{2.5+}$, the α and β points are thought of as Fe^{3+}-Fe^{3+} and Fe^{2+}-Fe^{2+} dimers in the following discussion. However, the actual charge state of these surface dimers cannot be confirmed with STM, and given the difficulties in showing the existence of complete charge transfer below T_v for magnetite [62, 63], and surface polarity considerations, unit charge localisation on these surface dimers is not probable. Similar dimer formation schemes have previously been used to explain non bulk periodicities observed by STM using tips prepared from magnetic materials [75, 82, 83].

The imaged dimers do not form straight rows along the [110] direction. They instead have a wave-like appearance. The fact that the dimer rows are not straight is illustrated by the line profile along the $[1\bar{1}0]$ direction, which shows an alternating periodicity of 5 Å $\pm$ 0.5 Å and 7 Å $\pm$ 0.5 Å along this direction [Fig. 5.3(c)]. The wavelike structure of the [110] oriented rows can also be visualised by examining the $(\sqrt{2} \times \sqrt{2})R45°$ unit cell, outlined in figure 5.3(b). Four α points form a (8.4 $\times$ 8.4) Å^2 square cell. For the [110] oriented Fe_{oct} rows to be oriented in a straight line a β point must be at the centre of this cell. However, instead the β point is shifted in the $[1\bar{1}0]$ direction, and a local minima (γ) is also in the cell. This examination of the surface unit cell, clearly shows that the Fe rows have a wavelike structure along [110]. The imaged surface geometry is outlined in figure 5.3(d).

5.3.1 Stabilisation of the Charge Ordered Arrangement

Repeated scans of the same charge ordered areas, over time periods as long as $\sim$ 1 hour, show that the surface maintains the same charge ordered arrangement for such time periods. This shows the charge ordered $(\sqrt{2} \times \sqrt{2})R45°$

reconstruction to be an extremely stable arrangement for the clean magnetite (001) surface, at room temperature.

As stated in section 3.6.1 it has previously been proposed in numerous studies that the $(\sqrt{2} \times \sqrt{2})R45°$ symmetry can arise due purely to a charge ordering of the Fe ions, without any actual surface reconstruction [46,82–85]. This model is essentially a bulk octahedral termination, with Fe^{2+}-Fe^{2+} and Fe^{3+}-Fe^{3+} dimer formation in a $(\sqrt{2} \times \sqrt{2})R45°$ symmetry. It was used to explain the image obtained in reference [83], where there was no observable shift of the dimers away from the [110] direction. The charge ordering has been explained in terms of the reduced co-ordination of the Fe_{oct} ions at the surface, due to the absence of the apical oxygen of the bulk octahedron. It is suggested that this lowers the symmetry from cubic to tetragonal, which leads to a splitting of the t_{2g} levels, which induces the formation of rows of dimers along the [110] direction [95].

This bulk termination model does not however take into account the fact that the magnetite (001) surface is polar. It also does not take into account the wavelike formation of the dimers, imaged here, along the [110] direction. In view of the fact that magnetite (001) is a polar surface, it is favourable to create oxygen vacancies for an octahedrally terminated surface. A $(\sqrt{2} \times \sqrt{2})R45°$ network of oxygen vacancies was proposed by Voogt *et al.* as one possible surface reconstruction resulting in the $(\sqrt{2} \times \sqrt{2})R45°$ LEED mesh they observed on MBE grown magnetite (001), and later used by Stanka *et al.* to explain STM images of the surface obtained with W tips. With respect to the images presented here, this oxygen vacancy network would explain the observed local minima (labelled γ in the STM images). The repulsive effect that the virtual positive charge of the O^{2-} vacancy would have on the Fe cations would also explain the wavelike appearance of the Fe rows.

The observed charge ordering can also be accounted for by a O^{2-} vacancy network, as the Fe^{2+}-Fe^{2+} dimers would preferentially occupy the Fe_{oct} sites nearest the oxygen vacancies, due to the virtual positive charge of defect, as shown in figure 5.4.

Taking into account all considerations; the non-bulk periodicity of the Fe_{oct} rows along the [110] direction, the wavelike appearance of the Fe_{oct} rows along the [110] direction, the observed charge ordering, and finally surface polarity considerations, the STM images presented here are best explained in terms of an octahedrally terminated surface with a $(\sqrt{2} \times \sqrt{2})R45°$ array of O^{2-} that induces the formation of dimers of nominal charge Fe^{2+}-Fe^{2+} and Fe^{3+}-Fe^{3+}.

In this discussion of the proposed surface termination it is worth mentioning the very recent DFT calculations by Cheng [85] and Pentcheva *et al.* [84]. Both studies favour bulk B-layer termination. However, the fact that the B-terminated model, with no vacancies, was found to be favourable by these calculations may, firstly, be due to the small size of the slabs used to model the surface. As the surface energy that induces these vacancies (i.e. surface polarity) increases with slab thickness [70], the final result obviously depends drastically on the thickness of the slab used. Secondly, the slabs used in these calculations are not charged balanced, and make an unrealistic comparison to single crystal magnetite. Both studies found that the surface termination depends on oxygen partial pressure, which suggests that differing images of the $(\sqrt{2} \times \sqrt{2})R45°$ reconstructed magnetite surface obtained in different STM studies could possibly be explained in terms of the surface preparation procedure.
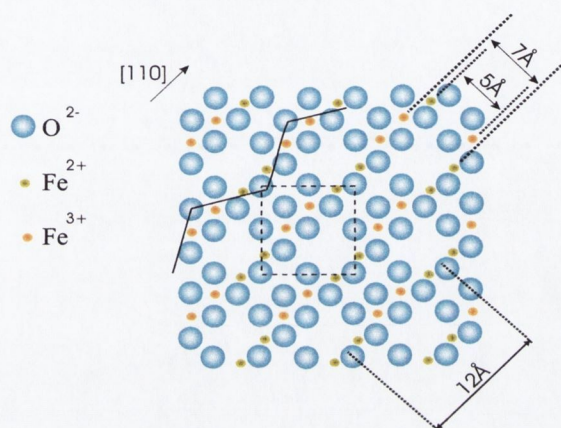
Figure 5.4: Model of the $(\sqrt{2} \times \sqrt{2})R45°$ reconstructed Fe_3O_4 (001) surface structure. A $(\sqrt{2} \times \sqrt{2})R45°$ ordered array of oxygen vacancies forms on the surface. This in turn results in dimer formation, due to alternate pairs of Fe_{oct} sites along the [110] direction being energetically inequivalent. Due to the virtual positive charge of the O^{2-} vacancy, the Fe^{2+}-Fe^{2+} dimers will preferentially occupy the pair of sites directly adjacent to it. The vacancy structure also explains the observed shifting of the dimers, perpendicular to the [110] direction.

5.4 STM Imaging with W tips

The $(\sqrt{2} \times \sqrt{2})R45°$ reconstructed magnetite surface has also been imaged with tips prepared from paramagnetic W. Figures 5.5(a) and 5.5(b) show atomic scale resolution images of the surface obtained with W tips, using the same tunnelling parameters as for the previously described images obtained with MnNi tips. The $(\sqrt{2} \times \sqrt{2})R45°$ symmetry is again clearly seen. However, the imaged surface now consists of only bright points, labelled δ, and local minima, again labelled γ. Both the bright points and local minima have a $(\sqrt{2} \times \sqrt{2})R45°$ symmetry, giving a 12 Å periodicity along [110] and [1$\bar{1}$0] directions. The bright points are elongated along the [1$\bar{1}$0] direction, with a full width at half maximum (FWHM) of 7.5 ± 0.5 Å, and have a FWHM of 5.0 ± 0.5 Å along the [110] direction. This corresponds to the combined value of the Fe^{2+}-Fe^{2+} and Fe^{3+}-Fe^{3+} dimers imaged with the MnNi tip. The $(\sqrt{2} \times \sqrt{2})R45°$ ordered array of minima, labelled γ, is imaged with both tip materials and these have the same dimensions with either tip. The large size of the imaged bright points δ, and the elongation along the [1$\bar{1}$0] direction, suggests that they correspond to two neighboring Fe-Fe dimers compressed together along the [1$\bar{1}$0] direction, as shown schematically in figure 5.5(d). The MnNi tip resolves this large bright point into two separate spots of differing intensity. Finally, we note that the images presented here are consistent with the images of the same surface obtained by Stanka *et al.* [80] using W tips, which also show no evidence for charge ordering.

5.4.1 Filled State Imaging

Filled state imaging of the $(\sqrt{2} \times \sqrt{2})R45°$ reconstructed magnetite surface, using a W tip, was also carried out. The same structure as for empty state
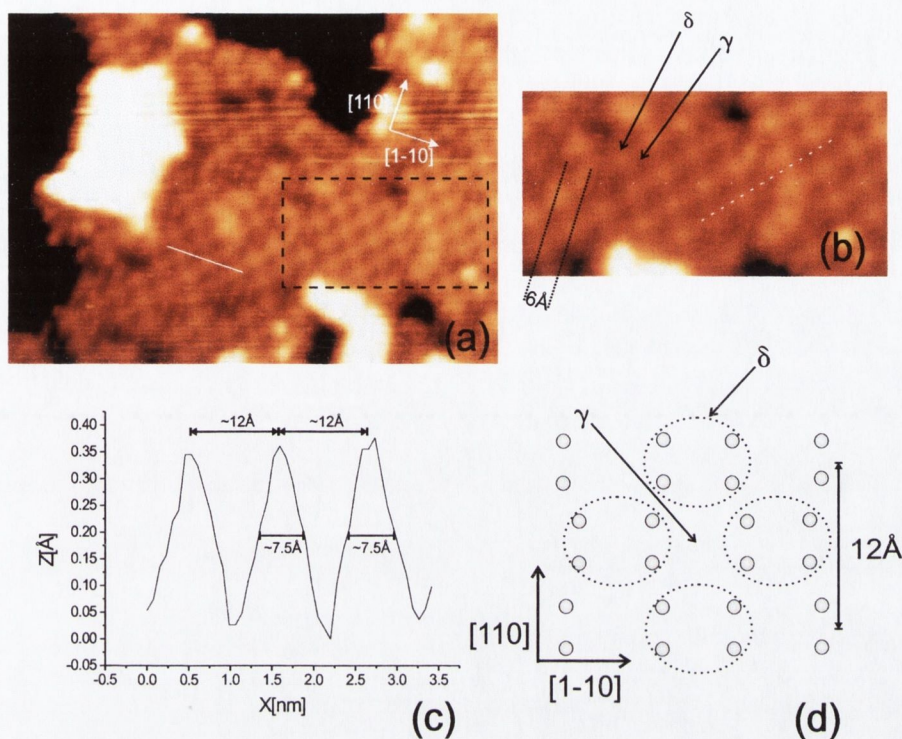
Figure 5.5: (a): A (190×140) Å^2 STM image, I_t= 0.1 nA, V_b= +1 V, taken with a W tip. Discrete bright spots (δ) and local minima (γ), each forming a $(\sqrt{2} \times \sqrt{2})R45°$ symmetry, are imaged. (b): A (90×50) Å^2 zoom in, for comparison with figure 5.3(b). The dashed white line illustrates the existence of an antiphase boundary, perpendicular to the line. (c): Line profile along the [1$\bar{1}$0] (solid white line) shows a 12 Å periodicity. The FWHM of a bright spot is $\sim 7.5 \pm 0.5$ Å along the [1$\bar{1}$0] direction and is $\sim 5 \pm 0.5$ Å along the [110] direction. The bright spots imaged here represent the combined value of both bright and grey spots imaged with a MnNi tip. (d): Schematic of the surface, as imaged with a W probe. The dashed ovals show the area on the surface where two neighboring dimers, shifted towards each other along the [1$\bar{1}$0] direction, are imaged together as a single bright spot, δ.
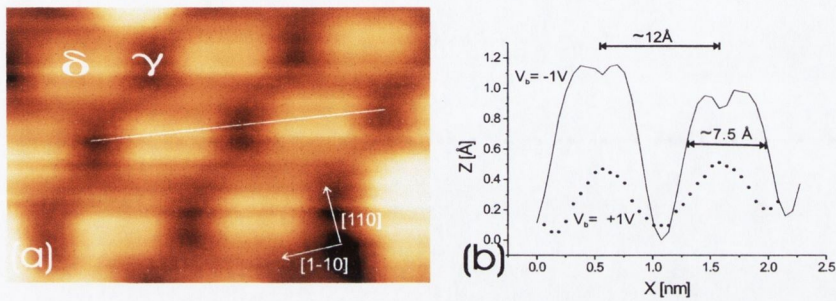
Figure 5.6: (35×22) Å^2 STM image, I$_t$= 0.1 nA, V$_b$= -1 V, taken with a W tip. This filled state image shows the same structure as empty state imaging, imaging large bright points δ and local minima γ. However the elongation of the bright points along the [1$\bar{1}$0] direction is more discretely resolved. Accompanying line profile shows the 12 Å periodicity giving rise to the $(\sqrt{2} \times \sqrt{2})R45°$ symmetry and also illustrates the large FWHM of the imaged bright point, supporting the model that it results from two dimers compressed together in the [1$\bar{1}$0] direction. The dotted curve corresponds to a line profile for +1 V bias, clearly showing that filled state imaging results in a much larger corrugation height of the Fe ions.

imaging is seen, however the bright points (δ) are more discreetly resolved, and the elongation of these bright points along the [1$\bar{1}$0] direction is more clearly seen, as evident from figure 5.6. The large size of the imaged bright points, and the elongation along the the [1$\bar{1}$0] direction further supports the suggestion that they correspond to two neighboring Fe-Fe dimers compressed together along the [1$\bar{1}$0] direction. A large change in the corrugation height of the bright points of the $(\sqrt{2} \times \sqrt{2})R45°$ reconstructed surface occurs when the polarity of the tunnel junction is switched. Figure 5.6(b) shows a comparative line profile for junction biases of +1 V and -1 V, with a tunnel current set-point of 0.1 nA. Tunnelling from the filled states of the magnetite (001) surface results in a much increased corrugation of the Fe ions. Whilst the structure is the same for either junction polarity, consisting of bright points (δ) and local minima (γ), the filled state images shows a more well defined structure of the dimer pair. This polarity dependent imaging shows the occupied orbitals of the $(\sqrt{2} \times \sqrt{2})R45°$ reconstructed surface to be more localized than the unoccupied orbitals. It is also worth briefly considering the asymmetry of the tunnel current implied by the large difference in the corrugation heights for positive and negative sample bias. As one would not expect such bias dependency for a metal-vacuum-metal junction, this illustrates that the complex DOS of bulk magnetite is maintained at the surface.

Also interesting with regard to the filled state imaging of the surface is that for the bright points at the edge of a reconstructed area there is an increased corrugation height in comparison to those bright points in the middle of the reconstructed area. This can be seen in figure 5.7 where, around the edge of the $(\sqrt{2} \times \sqrt{2})R45°$ reconstructed area, the bright points can be seen to be much higher. The corrugation height doubles for those bright points at the edge of the area, as can be seen from the line profile. It is also
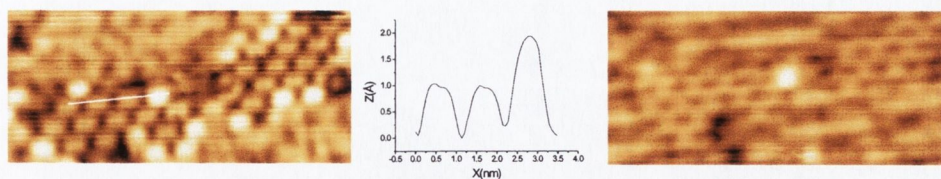
Figure 5.7: Left: (135×60) Å^2 STM image, I$_t$=0.1 nA, V$_b$= -1 V, taken with a W tip. Middle: Line profile across white line shown in STM image. The corrugation increase for bright points at edge of reconstructed area can clearly be seen. Right: Image as left, but with bias voltage switched to + 1 V. The difference in the corrugation of the edge bright points is no longer imaged, and it is also clear that the bright points are not as well resolved.

clear that this effect is not seen in the empty state image of the same area. The fact this effect is seen only when tunneling from the sample suggests that the increase in corrugation is due to an increased electron localisation at these points, which would be seen most clearly when electrons tunnel from the sample. This increased electron localisation is most likely induced by the reduced co-ordination of the Fe ions at the edge of the reconstruction, compared to those at the centre which are fully surface co-ordinated. This change in the local electronic properties of the surface, in a region of local disorder, clearly illustrates the importance of perfect surface order to the electronic properties of the magnetite (001) surface.

5.5 Improved Resolution of MnNi Tips: A Spin Polarised Effect?

Recalling section 3.6.2, there have been numerous SPSTM studies of the magnetite (001) surface. The initial study by Wiesendanger *et al.* [46] com-

pared images obtained with W tips and Fe tips. The W tips imaged a 3 Å periodicity, along the [110] oriented rows, whereas the Fe tips imaged a 12 Å periodicity. This was explained in terms of Fe^{2+}-Fe^{2+} and Fe^{3+}-Fe^{3+} dimer formation, doubling the periodicity to 6 Å. The imaged 12 Å periodicity was said to arise as the Fe tip only imaged the Fe^{2+}-Fe^{2+} dimers, due to the extra ($\downarrow$) contribution to the DOS. It was said the the Fe^{3+}-Fe^{3+} dimers were not actually imaged, but that they occupied points imaged as a local depression in the STM images. This experiment was repeated more recently by Koltun *et al.* [82], and again the Fe tip imaged a 12 Å periodicity. However, attempts to image the surface with W tips were not successful. The authors therefore assumed that the 12 Å periodicity imaged with an Fe probe is due to a spin polarised enhancement of the tunnel current.

It is clear from the STM images presented here that a 12 Å periodicity can be resolved with a W probe. Imaging this periodicity with a magnetic tip is therefore not a sufficient condition to be met in order to claim a spin polarised contribution to the tunnel current. It can arise solely due to topographical or electronic effects, rather than being due to spin polarised resolution.

Comparing the images obtained with W tips to those with MnNi tips clearly show that the MnNi tips offer improved resolution, imaging two distinct bright points whereas the W tips images these as one larger bright point. This enhanced resolution with MnNi tips can be explained in terms of a spin polarized contribution to the tunnel current. The contribution of the magnetite (001) surface to the tunnel current when scanning with a paramagnetic tip is dependent purely on the LDOS of the sample. When scanning with a tip prepared from magnetic material there is an extra, spin dependent component to the tunnel current. As the Fe^{2+}-Fe^{2+} and Fe^{3+}-Fe^{3+} dimers have a different spin configurations it should be possible to distinguish between them

with a magnetic tip [25]. Such a spin polarized contribution to the tunnel current is consistent with the recent spin-resolved PES experiments [67, 68] showing magnetite thin films to have a negative spin polarization of up to -80 ± 5% at room temperature. It is also possible that the differing contrast imaged with the MnNi tip is purely due to a differing LDOS of the Fe^{2+}-Fe^{2+} and Fe^{3+}-Fe^{3+} dimers, and is not a spin polarised contribution. However, one would then expect to also image the charge ordered arrangement with W tips. A further complication is that the electronic structure of the MnNi tip may differ from the W tip, allowing improved resolution, irrespective of any spin polarised concerns. The other possible explanation is that this alternating periodicity is a topographical effect, however, if this is so, the W tip would also resolve the spots of different brightness along the [110] oriented rows. Therefore, whilst other possible explantions must also be considered, a spin polarised effect provides a reasonable explanation for the surface structure imaged with MnNi tips, and differences between the images obtained with W and MnNi tips.

5.6 STS of the $(\sqrt{2} \times \sqrt{2})R45°$ Reconstructed Magnetite (001) Surface

Scanning tunneling spectroscopy was performed on the $(\sqrt{2} \times \sqrt{2})R45°$ reconstructed magnetite (001) surface at room temperature. Three normalised curves, which are representative of all those obtained on the surface are presented in figure 5.8. The presented curves are each the average of ~ 1000 curves taken at different points on a pre-defined grid of the scan area. Each are for different scanning sessions, with different W tips. All presented STS curves were obtained using the same current-voltage set points, 0.1 nA, +1 V.
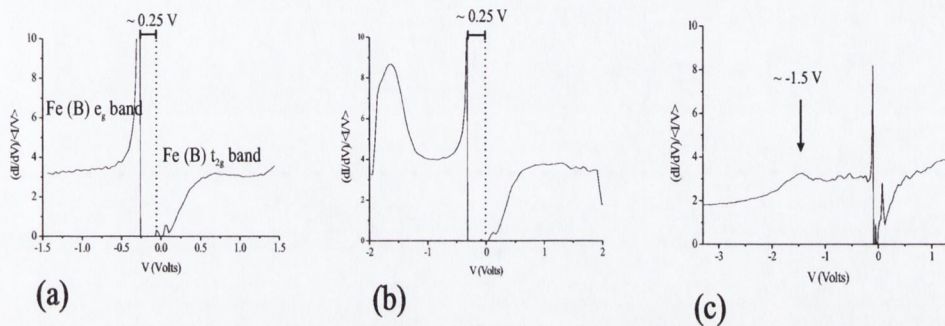
Figure 5.8: Tunneling spectra of the magnetite (001) $(\sqrt{2} \times \sqrt{2})R45°$ recon-structed surface. (a): Spectra in the range -1.5 V to +1.5 V, showing the features around E_f. A reproducible energy gap of $\sim$ 0.25 eV is measured in all spectra. The energy gap is measured from the FWHM of the peaks around E_f in the normalised spectra (b): Spectra in the range -2 V to +2 V. A distinct peak at -1.5 V is resolved. This peak has been resolved on numerous surface spectra. (c): Spectra in the range of -3 V to +1.5 V, again showing the peak at $\sim$ -1.5 V. Broad energy bands are formed on both sides of E_f which are generally featureless except for this broad peak in the occupied band at $\sim$ -1.5 $\pm$ 0.2 V, and a shoulder in the unoccupied band at $\sim$ +0.5 $\pm$ 0.1 V.

The curve features are reproducible for different current-voltage set-points. Points on the I(V) curves were taken at 0.02 V intervals, with an acquisition time of 320 μs per point. They are normalised as explained in section 2.1.3. The presented curves differ in that they are taken over different voltage ranges.

The normalised curves (a) and (b) clearly show that an energy gap is present between the filled and the empty states of the surface. This gap, measured from the FWHM of the peaks in the normalised spectra, is $\sim$ 0.25 eV wide. This is compared to an expected band gap of 0.1 eV for bulk magnetite [52]. Considering that it is a B-terminated magnetite (001) surface being probed here, the existence of states near E_f on the unoccupied side of the gap, seen in these spectra, is consistent with band structure calculations by both Yanase [9] and Zhang and Sathapy [65], the latter of which is shown in figure 3.3. In these calculations it was shown that the minority spin band ($\downarrow$) of the t_{2g} states of the B-sites cross over E_f, whereas the e_g majority spin band ($\uparrow$) on the occupied side does not cross over E_f.

Other than the presence of the energy gap, one can see a shoulder in the curves on the unoccupied side of the spectra at $\sim$ +0.5 V. These are the minority spin band ($\downarrow$) states. From the calculations of Yanase [9], and Zhang and Sathapy [65] this shoulder is in the energy region of the broad minority spin band of the t_{2g} states of the B-sites. On the occupied side of the spectra there is also a shoulder/peak at $\sim$ -0.25 V. A peak at $\sim$ -1.5 $\pm$ 0.2 V, seen very strongly in (b), is also resolved in many spectra of the surface. This peak is also seen in (c), which is over a larger voltage range. The shoulder at $\sim$ -0.25 eV represents the edge of the occupied band. The peak at $\sim$ -1.5 $\pm$ 0.2 V roughly corresponds to a peak in the majority spin e_g states of the Fe_{oct} B plane in the band structure calculations [9, 65]. The

observation of these B plane states with STS is consistent with the fact that the surface is terminated at the octahedral plane, as STS probes only those states present at the surface.

Comparing these spectra to other experiments, it is interesting to note that Wei *et al.* [96] measured tunneling spectra on magnetite(001)/MgO, below T_v, and found a gap of ~ 0.2 eV. That is similar to the magnitude of the gap measured here at room temperature. This is somewhat surprising, as one would expect a larger gap magnitude following the advent of the Verwey transition. One can explain this if electron hopping at the surface is already inhibited at room temperature due to the lack of co-ordinating Fe_{oct} ions above the surface layer, as proposed by Coey *et al.* [75] to explain the observation of surface charge ordering on magnetite (001) at room temperature. As the high room temperature conductivity of magnetite is attributed to electron hopping between Fe_{oct} sites, the absence of such sites above the surface is likely to inhibit this conduction mechanism. It was proposed that the surface will exhibit an energy gap, or mobility gap, in the DOS, above T_v [75], as seen in the STS spectra presented here. However, PES experiments by Chainani *et al.* show that for a magnetite single crystal, cleaved along [110], there is evidence of a metallic type density of states, on the occupied side of E_f, at room temperature [97]. Below T_v a gap of ~ 0.07 eV was found in the occupied band. The metallic state arises gradually with increasing temperature from below T_v. This metallic state, extending from the occupied side of the DOS, suggests that the Verwey transition is a metal-insulator transition as opposed to a semiconductor-insulator transition. It is not seen in the STS presented here. This can be explained in terms of the probing depth of PES compared to STS, with the former having an escape depth of ~ 5 Å, compared to only the states protruding from the surface

for the latter [16]. Furthermore, STS provides spectroscopic information on a highly localised area of the STM scan, as opposed to averaging over large sample areas when using PES. In their PES experiments Chainani *et al.* [97] resolved a state at -1.5 V, which is in agreement with the state resolved in our tunneling spectra. The resolution of this state on the octahedrally terminated surface with STS shows it to be one associated with the B-plane of magnetite.

5.7 Breakdown of $(\sqrt{2} \times \sqrt{2})R45°$ Reconstruction Due to UHV Annealing

5.7.1 Prolonged Annealing at ~ 800 K

Following prolonged annealing of 20-50 hours of the $(\sqrt{2} \times \sqrt{2})R45°$ reconstructed Fe_3O_4 surface in UHV conditions at ~ 800 K the O/Fe ratio of the Auger spectra of the surface reduces to 1.35 ± 0.05. This reduction in the O/Fe ratio of the surface, seen through AES, is accompanied by a breakdown of the $(\sqrt{2} \times \sqrt{2})R45°$ reconstruction. This is seen through both LEED and STM. In general the sharp $(\sqrt{2} \times \sqrt{2})R45°$ LEED is replaced by a blurred p(1×1) mesh [Fig. 5.9(a)]. Figure 5.9 shows STM images of a surface that was $(\sqrt{2} \times \sqrt{2})R45°$ reconstructed, following a 24 hour anneal in UHV at $\sim$ 800 K. The surface is characterised by the presence of large troughs. These can be 1.05 Å or 2.1 Å in depth. Generally the surface shows no atomic scale order, however on ocassion atomic scale rows are imaged on the surface, such as those in figure 5.9. The atomic scale rows do not have a $(\sqrt{2} \times \sqrt{2})R45°$ symmetry. Instead they form rows that are separated by ~ 12 Å. This is illustrated by the line profile in figure 5.9. There is no discernable corrugation
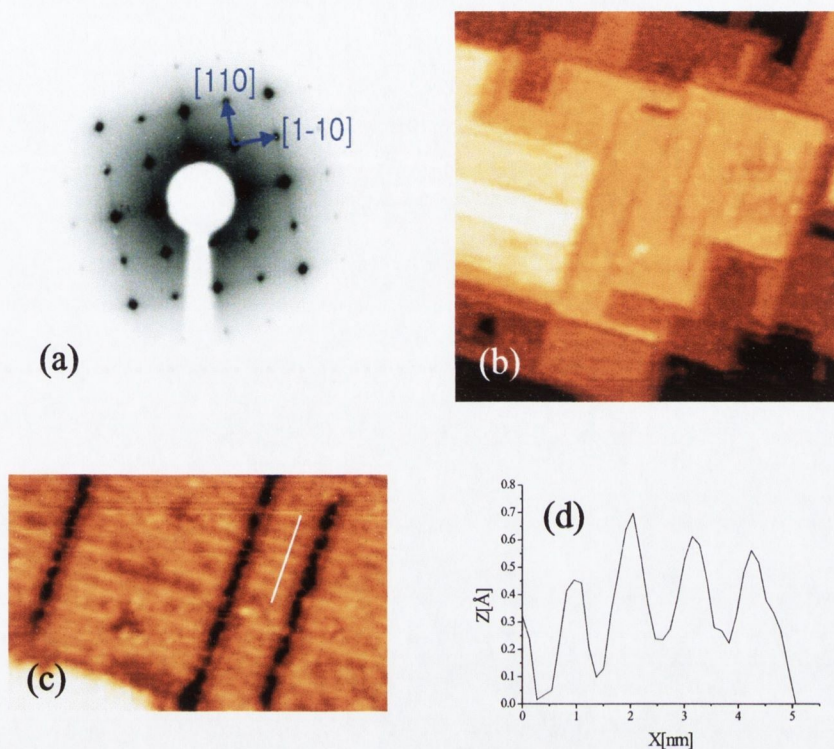
Figure 5.9: (a): LEED mesh of the magnetite (001) surface following prolonged annealing in UHV. The $(\sqrt{2} \times \sqrt{2})R45°$ reconstructed mesh is replaced by an unreconstructed p(1×1) mesh. (b): (700×700) Å^2 STM image, I_t= 0.1 nA, V_b= +1 V, taken with a W tip, and a (360×200) Å^2 zoom in on this surface. The $(\sqrt{2} \times \sqrt{2})R45°$ reconstruction is gone, and the terraces have begun to break down, with large troughs appearing on the terraces. Atomic scale rows are imaged on some parts of terraces, however long range atomic order has broken down. (c) and (d): Higher resolution STM image, and associated line profile, showing some local row formation, with a 12 Å periodicity.

along these rows, and it is clear to see from the image that they do not form a long range order on the surface. The large black troughs run perpendicular to the imaged atomic rows. Due to the decrease in the O/Fe ratio of the Auger spectra, it is likely that the troughs are a result of oxygen depletion of the surface, giving rise to line defects. Indeed this is pointed to by the fact that simply by annealing the sample in O at 2.66×10^{-6} mbar for 15 min results in the surface regaining the $(\sqrt{2} \times \sqrt{2})R45°$ structure. The fact that annealing in UHV can destroy the $(\sqrt{2} \times \sqrt{2})R45°$ order, and that by simply annealing the disordered sample in an oxygen environment can return the reconstruction shows the importance of the O/Fe ratio to the surface of magnetite, and specifically to the importance of the O/Fe ratio to the presence of the $(\sqrt{2} \times \sqrt{2})R45°$ reconstruction.

Chapter 6

Germanium (001)

6.1 Introduction

Germanium is a group four intrinsic semiconductor. It was the first semi-conductor to be used commercially, however despite this fact, silicon is now far more widely used than germanium in the semiconductor industry. This is because of the lower cost of Si, the higher temperature tolerance of Si devices, and the fact that unlike Ge its oxide is not water soluble, which is advantageous in processing of devices. Ge still finds use in low operating voltage devices and in power rectifiers. More recently, due to the use of epi-taxial Ge thin films grown on Si for bipolar transistors, which have proven faster and more efficient than existing Si transistors, interest in Ge has inten-sified dramatically [98]. Ge has also been studied in terms of the possibility of achieving a dilute magnetic semiconductor, through doping with magnetic elements, in the hope of combining magnetic and electric devices on a single chip [2, 4–6]. Furthermore, the possibility of using ferromagnetic metals as a source of spin polarised electrons for injection into semiconductors has led to interest in the growth of ferromagnetic layers on Ge [7, 8, 99–102]. More gen-
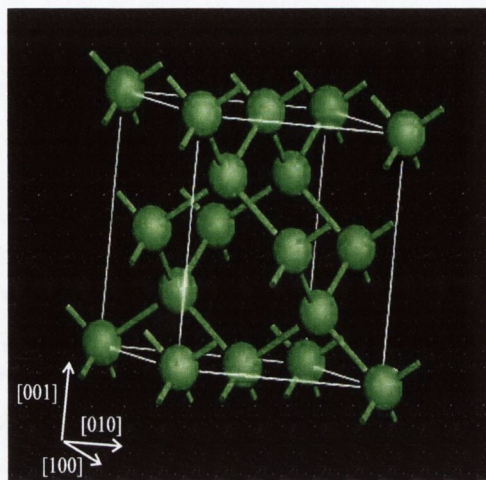
Figure 6.1: The Germanium unit cell. It crystallises in the diamond structure, which can be thought of as two interpenetrating fcc lattices. The lattice constant for Ge is 5.66 Å

erally, growing sub-monolayer metal films to obtain ordered clusters on semi-conducting substrates has also received much attention [103]. This chapter provides an introduction to the Ge(001) surface, and an overview of related work.

6.2   Surface Terminations of Ge(001)

Germanium crystallises in the diamond structure [Fig. 6.1]. It has a lattice constant of 5.66 Å. A calculated DOS for bulk germanium [104] is shown in figure 6.2. Around E_f a band gap ~ 0.7 eV is present, with a broad band centred on $\sim$ -1.1 eV found on the occupied side and one centred on $\sim + 0.75$ eV found on the unoccupied side. Cleaving the (001) face of a Ge crystal results in the formation of a surface with two dangling bond sp^3 hybrid orbitals per surface atom. As with the Si(001) surface, the Ge(001) surface
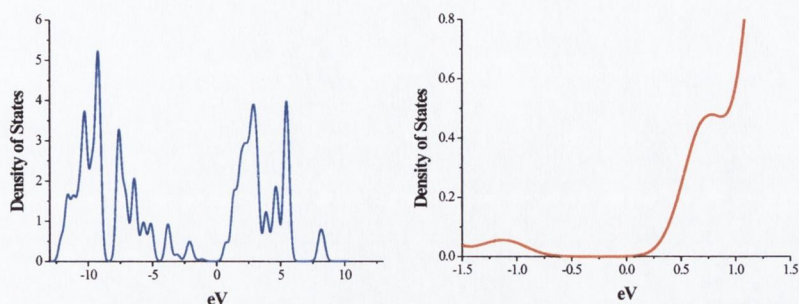
Figure 6.2: Calculated electronic density of states of germanium [104]. Left is from -12 eV to +12 eV. Right a zoom in on the area around E_f. A band gap of ~ 0.7 eV is calculated. An occupied state centred on $\sim$ -1.1 eV, and an unoccupied state centred on $\sim$ +0.75 are also found.

reconstructs through the pairing of nearest neighbour surface atoms, forming dimer rows orientated along the <1$\bar{1}$0> crystallographic directions [105]. This gives rise to the (2×1) surface reconstruction, which is the primary LEED mesh observed at room temperature [106].

(2×1) Surface Reconstruction

The original models for the (2×1) reconstructed surface were based on two schemes. The first was a symmetrical surface dimerisation, along the [1$\bar{1}$0] direction, which would lead to an odd number of unpaired electrons per surface atom and result in a half filled metallic surface state. The second was an asymmetrical surface dimerisation model, introduced by Chadi [107], essentially consisting of an energy saving buckling of the surface dimers, which would result in a semiconducting type surface state band. A schematic of these dimerisation schemes, and how it gives rise to the (2×1) reconstruction, can be seen in figure 6.3.
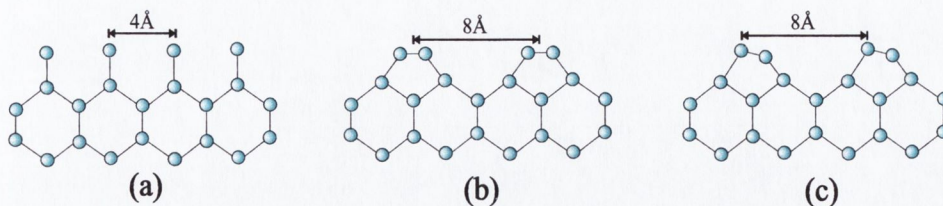
Figure 6.3: (a): Side view of bulk terminated (001) surface. Each surface atom has two dangling bonds. (b): The dimerisation that gives rise to the (2×1) surface reconstruction. The dimers shown here are symmetric. (c): Schematic of the asymmetric, or buckled dimer, found to be the lowest energy configuration by Chadi [107].

It is now accepted that the reconstruction is best explained by the latter model, with the formation of asymmetrically buckled dimer pairs along the $<1\bar{1}0>$ crystallographic directions. These buckled dimers flip-flop rapidly at room temperature between their two equivalent positions. The calculations by Chadi imposed no symmetry constraints on the dimers and found that the buckled dimer [Fig. 6.3(c)] forms spontaneously, and that the symmetric dimer is in fact unstable [107]. Later total energy calculations also favoured this model [108, 109]. The buckling results in a charge transfer between the two atoms of the dimer, with the buckled up dimer being electron rich and the buckled down dimer electron poor. First principle calculations by Kruger et al. [110] have determined the Ge(001) surface states, from the bulk states, for the asymmetric dimer model. A semiconducting gap of $\sim$ 0.8 V was calculated. They found 4 salient surface bands; the dimer bond band D_i, the dangling bond band D_{up}, the dangling bond band D_{down}, and the anti-bonding dimer bond band D_i^*. In addition there were found to be back-bond states of mainly sp character; B_i and s character; S_i. These were found to

be localised between the first and second layer, perpendicular to the surface. The D_{up} band was found to be a very broad peak from the edge of the gap region to -1.5 V. The D_{down} band was also a broad band, from the unoccupied edge of the gap to 1 V. A back-bond state was found at $\sim$ -1 V.

c(4×2) Surface Reconstruction

The c(4×2) reconstruction is also observed on the Ge(001) surface. At room temperature weak quarter order LEED spots have occasionally been observed on the surface, consistent with some localised 4× reconstruction [106]. The intensity of these quarter order spots have been shown to increase with decreasing temperature, until at $\sim$ 200 K only the c(4×2) mesh is observed, showing the (2×1)$\longleftrightarrow$(4×2) two-dimensional phase transition to be of the second order type [106]. The buckled dimer again forms the basis of the c(4×2) reconstruction. Unlike the (2×1) reconstruction the dimers are buckled out-of-phase (or anti-correlated) along the [110] oriented rows. They do not flip-flop between the two possible configurations of the dimer, as occurs for the (2×1) reconstruction, but are frozen in one buckled configuration. This model for the c(4×2) reconstruction was again proposed by Chadi [107]. This configuration was found to be true, using surface sensitive XRD, by Ferrer *et al.* [111]. The different buckling arrangement of the dimers in the (2×1) and c(4×2) reconstructions is more clearly seen in the schematic of figure 6.4.

Kevan and Stoffel [112] studied the (2×1)$\longleftrightarrow$c(4×2) transition using PES, and found the transition to be an order-disorder, metal-insulator transition. A metallic surface state was present for the room temperature (2×1) transition. This state gradually disappeared as the sample was cooled, and was absent for the low temperature c(4×2) phase. They suggested that the metallicity of the (2×1) phase is due to the flip-flopping of the dimers be-

tween their two equivalent buckled positions. Between these two buckled states they pass through a symmetric state, giving rise to a conductivity band not present for the frozen buckled dimers of the c(4×2) reconstructed surface.

p(2×2) Surface Reconstruction

Finally, a p(2×2) reconstruction can also occur on the surface. Like the c(4×2) reconstruction it arises due to frozen buckled dimers, however the buckling is in phase (or correlated) along the dimer rows. Needels *et al.* [113] calculated the p(2×2) and the c(4×2) reconstruction to be almost degenerate. Experimentally this reconstruction has not been widely observed for the Ge (001) surface, however it has been imaged using STM, for T ≤ 80 K, where it was found to co-exist with the c(4×2) reconstruction [114, 115].

6.3 Previous STM Characterisation of the Ge(001) Surface

6.3.1 The Clean Ge(001) Surface

STM imaging of the Ge(001) surface by Kubby *et al.* [116] imaged rows oriented along the $(1\bar{1}0)$ direction, separated by 8 Å along the (110) direction. The periodicity along the rows was 4 Å, corresponding to the (2×1) surface termination, confirming the earlier room temperature LEED mesh observed by Kevan [106]. The orientation of the dimer rows were found to rotate through 90° on terraces separated in height by 1.4 Å. This is due to the 90° rotation of the tetrahedral dangling bonds between these terraces. This domain structure on alternating terraces gives rise to the observed two
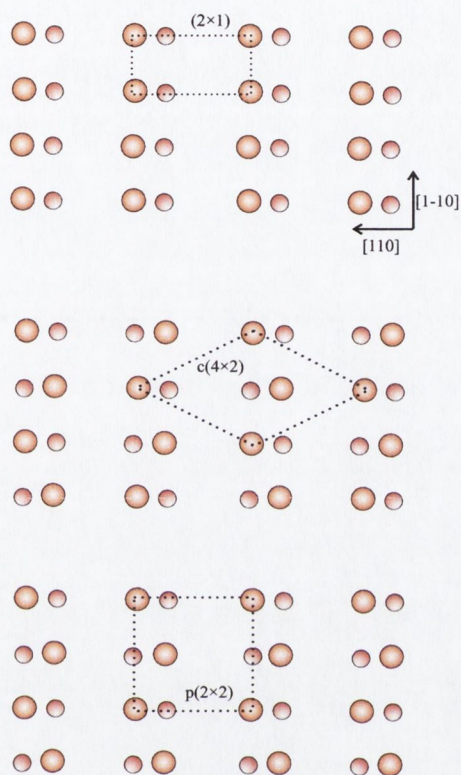
Figure 6.4: Top view of the surface reconstructions of the Ge(001) surface. The (2×1) reconstruction consists of rows of dimer pairs, oriented along the [1$\bar{1}$0] direction. The dimers are buckled asymmetrically out of the plane of the surface, as shown. The c(4×2) reconstruction again consists of dimer pairs, however they are frozen out-of-phase, as viewed along the [110] direction. Finally the p(2×2) reconstruction involves dimers frozen in phase along the [110] direction. It differs from the (2×1) reconstruction in that the direction of the dimer buckling alternates along the [1$\bar{1}$0] rows, as shown.

domain (2×1) LEED mesh. Areas exhibiting the c(4×2) reconstruction were also imaged, generally in the vicinity of defects and steps. The STM images of the surface show a large polarity dependence. As there is a higher electron density on the D_{up} electron of the dimer pair, when tunnelling from the tip into the sample one would expect to emphasise the states of the D_{down} band, whereas tunnelling from sample to tip one would expect to emphasise the states of the D_{up} band. This was found to be true, and was evident by a phase shift of the frozen dimers of the c(4×2) reconstructed areas when changing junction polarity. Surprisingly, even for the symmetric (2×1) surface, asymmetric behaviour could be imaged with STM. This was most easily seen through a clear phase shift along the dimer rows for positive and negative polarity images.

STS of the (2×1) surface was also carried out in the study by Kubby *et al.*, measuring an insulating gap of 0.9 eV. Surface states were resolved, with two filled state features at -1 eV and -2.6 eV, and one empty state feature at +0.9 eV. In line with the calculations by Kruger [110] the -1 eV band was labelled as the D_{up} band, and the +0.9 eV feature as being due to the D_{down} band. Both peaks have widths of ~1 eV. The feature at -2.6 eV was labelled as the D_i band. These results were said to be in general agreement with the ARPES results of Kevan and Stoffel [112], which found peaks at -0.6 and -1.3 V. The difference in energies of the resolved peaks between the two techniques was explained in terms of the increased sensitivity of STS to p_z like states of germanium, compared to PES.

Later STM studies have consistently shown that the (2×1) reconstruction dominates at room temperature, with areas of the c(4×2) reconstruction also present [117]. The presence of missing dimer defects and missing dimer complexes (such as twin missing dimers) on the terraces has also been consis-

tently noted, and it has been shown that such defects lead to a local freezing of the flip-flop motion of the (2×1) dimers in the vicinity of the defect, resulting in the presence of localised areas of the $c(4\times2)$ reconstruction around defects, at room temperature [118].

The formation of a striped domain pattern of (2×1) and $c(4\times2)$ domains at room temperature on extremely defect free surfaces has been imaged with STM at room temperature [119]. Whereas the defect induced domains decay over a length scale of $\sim$4-40 Å, these domains can be up to 80 Å wide and form a well ordered striped domain structure over the entire surface. The presence of even a low concentration of surface defects destroys this domain structure. The authors suggest that this domain formation at room temperature is driven by a strain relief mechanism. This property of the surface was recently used to examine the contrasting electronic properties of the (2×1) and $c(4\times2)$ reconstructions using STS by Gurlu *et al.* [120]. It was found that the (2×1) domains have states near E_f that are not resolved for the neighbouring $c(4\times2)$ domains. The presence of states in the semiconducting gap of the tunneling spectra was explained by Gurlu *et al.* using the same mechanism as previously proposed by Kevan and Stoffel [112]. i.e. The flip-flopping dimers of the (2×1) reconstruction pass through a symmetric state resulting in a conductivity band for the (2×1) domains that is not present for the $c(4\times2)$ domains.

6.3.2 Growth of Ultrathin Metal Films on the Ge(001) Surface

There has been much recent work focusing on the use of Ge(001) as a substrate for the deposition of metals. Due to superconducting characteristics below 2 K the Ag/Ge(001) system has been extensively studied using STM [121–123]. This work has focused on finding the most favourable adsorp-

tion sites for the metal adatoms, and whether the nucleation occurs normal or orthagonal to the dimer rows. The Pt/Ge(001) system has also been studied, again in relation to the initial nucleation sites of the deposited Pt atoms, and also with respect to the temperature dependence of the growth [124]. This system has also been shown to form 1-D Pt nanowires with metallic conductivity on the surface following high temperature (>1200 K) annealing in UHV [125].

Of particular interest has been the growth of magnetic elements, driven by the possibility of integrating magnetic devices and electronic devices on a single chip [2, 4–6]. One avenue explored with respect to this integration has been that of dilute magnetic semiconductors (DMS). It was predicted by Dietl *et al.* [126] that ferromagnetic order can be stabilised in the group four semiconductors. Some of the most promising results have come from Mn substituted Ge, which has yielded a $T_c = 116$ K for MBE grown films [5], and of 285 K for a single crystal [99]. This in turn has led to interest in the UHV growth of epitaxial Mn on both the (100) and (111) faces of Ge [100]. In terms of the formation of Ge based DMS, Choi *et al.* have shown that Cr and Fe doped crystals exhibit ferromagnetic behaviour, at 126 K and 233 K respectively [127, 128]. In these studies they found an increase in the lattice constant of the Fe doped Ge lattice, arguing that this shows the Fe is incorporated into the host lattice. However, despite the intensive research, the actual use of DMS in working devices languishes, due to the very low values of T_c and problems with integration into existing device technologies [7].

Alongside research into dilute magnetic semiconductors, the deposition of ferromagnetic metal films onto semiconductor substrates is also being actively studied. There are many advantages of using ferromagnetic metals as a source of spin polarised carriers [7]. Firstly, they are easily integrated into existing

processing technology. Secondly, they are a source of spin polarised electrons, whereas for many of the DMS discovered the spin polarised carriers are holes. This is advantageous because electrons have been shown to have long spin scattering lengths in semiconductors [129]. Thirdly, the electrons they provide are highly spin polarised. Finally, unlike DMS, the ferromagnetic metals have high T_c's, allowing their use in devices at practical temperatures.

Indeed, Fe has already been shown to be a suitable candidate for spin injection into semiconductors at room temperature by Zhu *et al.* [10]. The injection of spin polarised electrons into GaAs was demonstrated for a GaAs(001)/(In,Ga)As light emitting diode, covered with Fe. The degree of the emitted circularly polarised light was calculated to be consistent with a spin injection efficiency of 2%. The process was explained in terms of the formation of a Schottky barrier at the interface. This allows the tunneling of electrons through a depletion layer into the active region of the diode. This spin injection mechanism is not affected by the resistance mismatch of the metal and substrate [130].

The benefit of the Fe/GaAs(001) interface lies in the fact that, because of the low lattice mismatch between the two, Fe can be grown epitaxially on GaAs. This is also true for Ge and ZnSe substrates. Some previous studies on the deposition of Fe thin films onto the Ge(001) surface have been performed [102, 131, 132]. Much of the work has focused on the growth mode of the films, the degree of intermixing, and the extent of magnetic dead layers at the interface. It was initially reported, in reference [133], that Fe films grown on Ge at 150°C can have magnetically dead layers of up to 100 Å. However, more recent work suggests that the extent of magnetic dead layer is not as large as originally suggested. Ma and Norton [131] have performed a combined LEED, AES, ARAES and MOKE study on this system. They found the

initial nucleation to be disordered, with local order (as seen through LEED) commencing at seven monolayers of Fe. Contrary to reference [133] room temperature MOKE loops show hysterisis for films with thickness $\geq$ 4 ML. This suggested that the intermixing problem is less than previously thought, but still shows that the first 3-4 ML are either magnetically dead, or have an easy axis perpendicular to the film plane. Through the temperature dependence of the AES concentration of Fe they suggested that severe intermixing of the Fe with the Ge substrate commences at 160°C and that rapid diffusion of Fe into the bulk occurs at 400°C, with the Fe signal disappearing at this temperature, consistent with complete diffusion of Fe into the bulk. It is also interesting to note that they found that the Fe thin films lack the four fold magnetic symmetry of bulk α-Fe. There is a uniaxial magnetic anisotropy, with the [110] direction behaving as a hard axis, and the [1$\bar{1}$0] direction as a soft axis. Whilst Ma *et al.* do not offer an explanation for this anisotropy, Kneedler *et al.* have shown that for the similar Fe/GaAs(001) system the effect is less pronounced for thicker films, pointing to the interface as the origin of the effect [134].

Schleberger *et al.* have performed an XPS study on amorphous Fe-Ge nanostructures [135]. They observe chemical shifts of the core levels which, they say, excludes the formation of a sharp Fe/Ge interface. Nominal thicknesses of > 10 Å Fe had to be achieved for the formation of a pure Fe toplayer above the intermixed region. For the deposition of Ge onto an Fe substrate no significant shift is observed, suggesting a sharp interface is formed. However, a recent study by Cantoni *et al.*, again using XPS, shows that the intermixing of Ge in the Fe toplayer for room temperature grown films is less that 3% [102]. Furthermore, using MOKE, they detect the onset of room temperature ferromagnetism at 3 ML, indicating that there is virtually no magnetic

dead layer, consistent with the formation of an abrupt interface.

Finally, in relation to the Fe/Ge interface, it is worth noting that Freeland *et al.* have found direct evidence of an induced magnetic moment in Ge at the Fe/Ge interface using X-ray magnetic circular dichroism [101]. Spin polarised s states at E_f, and a d-component at higher energy were found to be present at the Ge interface layer, both oriented anti-parallel to the moment of the Fe layer, with a magnitude of 0.1 μ_b.

Chapter 7

Nucleation of Iron on Germanium (001)

7.1 Introduction

In this chapter, results on the initial nucleation of Fe on the Ge(001) surface are presented. STM and STS were carried out on the clean Ge(001) surface. The initial nucleation of Fe on this surface was studied using STM. Small clusters are found to form for deposition with the substrate at room temperature. These clusters are discussed in detail. The influence of elevated substrate temperature on the initial growth of Fe was also studied with STM. The effect of post annealing on the Fe-Ge interface, with respect to intermixing, was investigated with AES and STM. Finally, STS of the clusters that form on the Ge(001) surface has been obtained.

7.2   Clean Ge(001) Surface

7.2.1   Preparation of the Clean Ge(001) Surface

The Germanium samples used in these experiments were cleaved from a 3"
n-type (Sb doped, 25 $\Omega^{-1}cm^{-1}$) (001) oriented wafer. The samples were then
cleaned in ethanol using an ultrasonic bath. Following this they were mounted
into Ta/Mo sample holders and inserted into the UHV system. In-situ UHV
preparation of the Ge(001) surface is well documented [136]. The samples
are initially outgassed in UHV at 800 K. This is followed by repeated cycles
of Ar$^+$ ion etching and annealing in UHV. Samples were etched for 15 min,
using an ion energy of 1 keV. UHV annealing at temperatures in the 800-1000
K range for time periods $\sim$ 25 min was then carried out. This preparation
procedure has been shown to result in the formation of well ordered Ge
surfaces [116]. One problem associated with this preparation technique is
the presence very large protrusions on the surface. Generally, the number
of these defects are found to be greatly reduced as the number of etch and
anneal cycles is increased. These large defects have been explained in terms of
the diffusion of C contaminants from the bulk crystal to the surface [136,137].

An AES spectrum of the Ge(001) surface following repeated cycles of Ar$^+$
etching and annealing in UHV is presented in figure 7.1. Contamination of
the surface is below detection limit of the analyser, i.e. the only Auger peaks
present are those associated with Ge. Low energy peaks at 23, 47, 53, 89
and 108 eV, as well as the higher energy peaks, specifically the one at 1147,
are characteristic of the Ge surface. LEED shows that the surface exhibits
the well known (2×1) reconstruction, seen in figure 7.2, as expected for the
Ge(001) surface at room temperature [106].
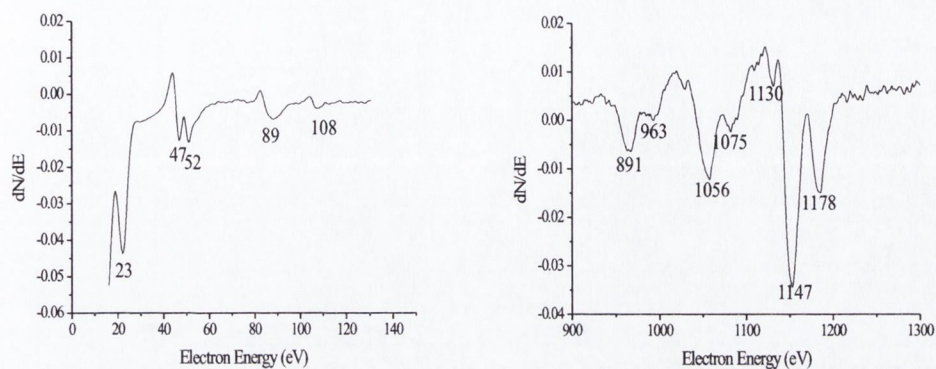
Figure 7.1: Auger electron spectrum of the clean Ge(001) surface. Graph left shows the low energy peaks, and right the high energy peaks. The peak at 1147 eV is used to calculated relative surface concentrations. After repeated etch and anneal cycles contamination is below the limit of the Auger set-up.
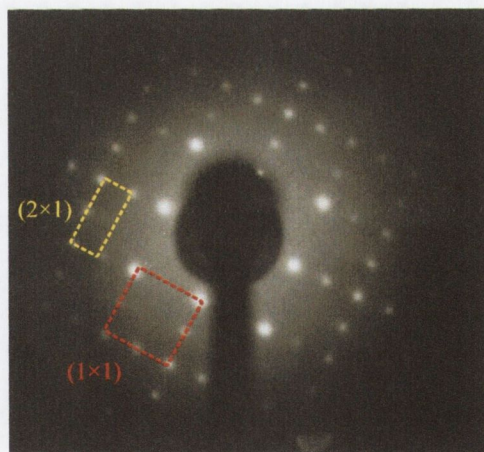
Figure 7.2: LEED mesh of the clean (2×1) reconstructed Ge(001) surface. The unreconstructed (1×1) unit cell is outlined with a red square, and the (2×1) superlattice is outlined by the yellow rectangle.

7.2.2 STM/STS of the Clean Ge(001) Surface

A STM image of the Ge(001) surface following repeated cycles of Ar^+ ion bombardment, and annealing in UHV, is shown in figure 7.3. The Ge dimer rows, oriented along the $[1\bar{1}0]$ direction, are imaged. These rows are separated by 8 Å in the [110] direction. As seen in previous STM studies [117], the (2×1) reconstruction forms a long range reconstruction on the surface and a (2×1) unit cell is outlined with a yellow rectangle [Fig. 7.3(b)]. Some examples of missing Ge dimer defects are also imaged, and these are marked by white circles [Fig. 7.3(c)]. The c(4×2) reconstruction is also evident on the surface, in the region of the missing Ge dimer defects. The c(4×2) surface unit cell is outlined with a red rectangle.

I(V) tunnelling spectra of the clean Ge surface were also obtained, using W tips. A representative I(V) curve of the surface, taken using tunnelling parameters of +1.97 V, 0.5 nA, is shown in figure 7.4. The curve is an average of 900 separate curves taken on the surface. Points were taken at 0.04 V intervals, from -2 V to +2 V, with an acquisition time of 320 μs per point, and a delay time of 100 μs. The curve on the right is a normalised version of the same I(V) curve, using the normalisation procedure described in section 2.1.3. A semiconducting gap of $\sim$ 0.8 eV is measured from the spectra. Two filled state peaks are resolved at -1.0 eV, -0.4 eV and an empty state peak is resolved at 0.75 eV. These states are within the region of the bulk bands found in figure 6.2, and are in broad agreement with previous tunnelling spectra of the clean Ge(001) surface [116, 120]. The semiconducting gap is in the same range as both previous studies; 0.9 eV by Kubby *et al.* [116], and 0.75-0.9 eV by Gurlu *at al.* [120]. In the study by Kubby *et al.* peaks at roughly -1 eV and 0.9 eV were resolved. These states are associated with the D_{up} band and D_{down} band of the surface dimer, and were found always
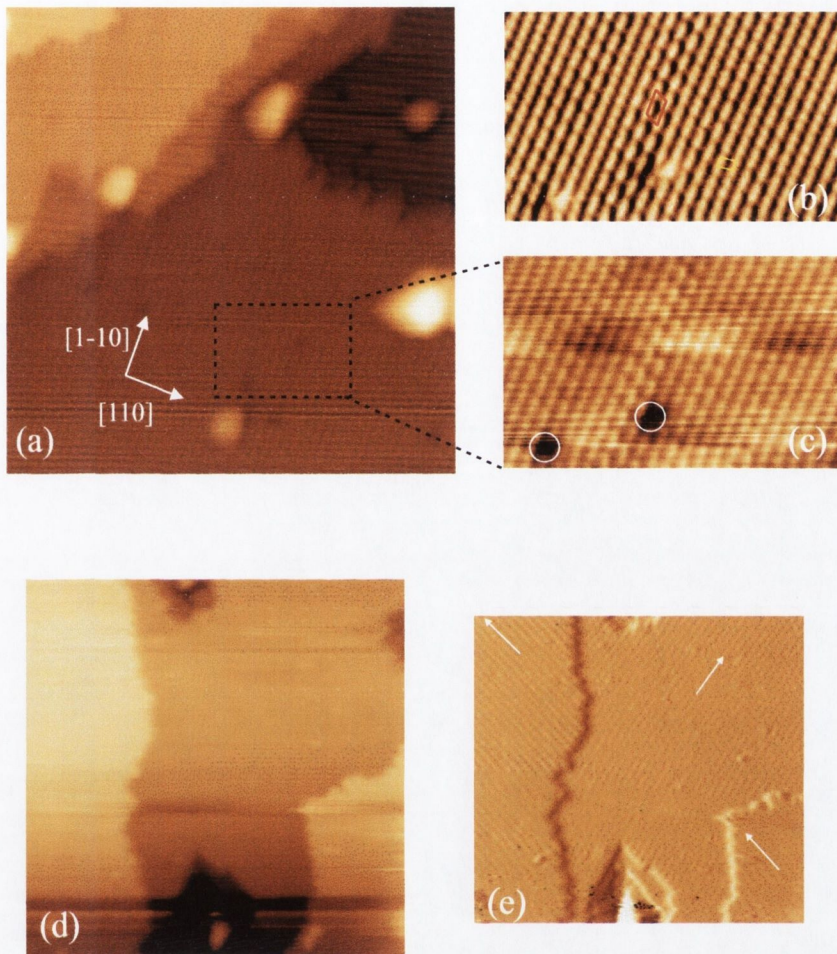
Figure 7.3: (a): (320×320) Å² STM image of Ge(001) surface following 5 cycles of etching and annealing in UHV. Terraces are formed, with both the (2×1) and c(4×2) reconstructions evident. Also imaged are white protrusion, associated with the diffusion of C contaminants from the wafer. (b) and (c): (150×90) Å² zoom-in and differentiated image of the zoom-in respectively. The c(4×2) surface unit cell is marked with a red and the (2×1) surface unit cell with a yellow rectangle. Also marked, with a white circle is a missing Ge dimer defect, associated with the formation of the c(4×2) reconstruction. (d): (500×500) Å² STM image of the clean surface, and (e): Derivative of a zoom-in, showing the 90° rotation of the dimer row direction from one terrace to the next. The (2×1) reconstruction forms over the entirety of the surface. All images here $I_t = 1$ nA, $V_b = $ -1 V.
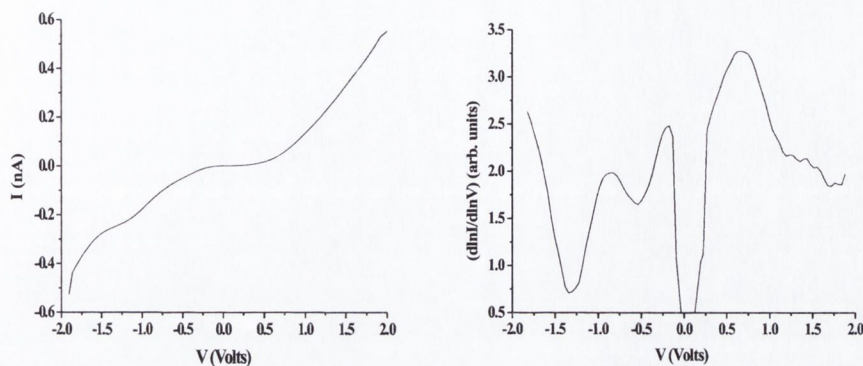
Figure 7.4: STS I(V) curve of the clean Ge(001) surface and normalised version of this curve, right. A semiconducting gap of ~ 0.8 eV is measured from the FWHM of the gap region. States are resolved at -1.0 eV, -0.4 eV and 0.75 eV.

to be present, regardless of whether the surface exhibits a (2×1) or c(4×2) reconstruction. The peak at -0.4 eV, seen in 7.4, was not resolved in the STS study by Kubby. However, in the spectra presented here, the peak is very strong. The presence of this peak is in agreement with PES studies of the Ge(001) surface by Nelson *et al.* [138], who resolve a state at -0.6 eV and by Hsieh *et al.* [139], who resolve a state at -0.5 eV. This state was found to be strongest for lower photon energy, which emphasises the p states, and weakest for higher photon energies, which emphasise s states. The strong presence of this peak at $\sim$ - 0.4 eV in the STS spectra is in agreement with this energy dependence, as STS emphasises the p-states of this surface over the s states. The presence of the peak in the STS spectra also confirms that the state is present on the surface of Ge(001), rather than it being solely a bulk contribution from the underlying layers that are also probed by PES. Gurlu *et al.* also resolved a peak in STS spectra at -0.5 eV in the study of

the $(2\times1)/c(4\times2)$ domain structure of the Ge(001) surface [120]. The peak was weak, and only resolved for the $c(4\times2)$ domains of the surface. They therefore suggested its presence is due to the more than half filled π states of the D_{up} band, which they say is present only for the $c(4\times2)$ reconstructed surface. However, in our work, the peak appears to be present for areas of the surface exhibiting the (2×1) reconstruction, suggesting it is not due to a state present only for the frozen dimers of the $c(4\times2)$ reconstruction. It is also worth recalling that in their work Gurlu *et al.* resolved states in the semiconducting gap, around E_f, for the (2×1) reconstructed surface, which they suggested was due to the flip-flop motion of the dimers in the (2×1) reconstruction [120]. We have not resolved such metallic surface states within the region of the semiconducting gap in the STS spectra obtained during the course of this work.

7.3 Nucleation of Fe Films on the Ge(001) Surface

7.3.1 Initial Nucleation of Fe on Ge(001) Surface at Room Temperature

Following the preparation of the clean Ge(001) surface, ultrathin films of Fe were immediately deposited onto the surface in UHV, at room temperature, using the Omicron EFT triple cell evaporator. A thoroughly de-gassed ultrapure Fe rod source was used. Generally 30 minutes of evaporation was necessary to stabilise the flux rate, and the Fe was then deposited at rates $\sim 1\text{Å/min}$. Nominal film thicknesses were measured using a quartz crystal balance. The chamber pressure did not rise above 1×10^{-9} mbar during de-
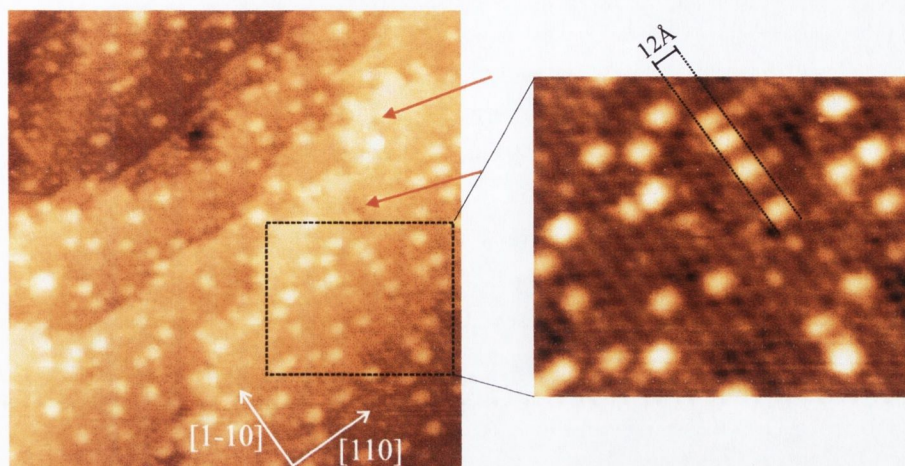
Figure 7.5: (a): Large scale, (378×378) Å² STM image of the clusters that form on Ge(001) following the deposition of Fe. $I_t = 0.1$ nA, $V_b = +1$ V. Two missing Ge dimer pair vacancies are pointed to by red arrows. (b): (146×123) Å² zoom-in of the image showing the clusters with respect to the substrate. While the Ge dimer rows are separated by 8 Å along the [110] direction, the clusters are 12 Å wide in this direction.

position. STM commenced within 30-60 minutes following deposition. The pressure in the STM chamber was 1.33×10^{-10} mbar .

An STM image which shows the initial stages of the room temperature growth is presented in figure 7.5. Assuming the imaged islands consist solely of Fe, the coverage corresponds to ~ 15 % of 1 ML. The surface is characterised by the formation of nanometre scale clusters. In the direction perpendicular to the Ge dimer rows, [110], virtually all of the clusters are 12 Å wide. In the direction parallel to the dimer rows, [1$\bar{1}$0], the clusters can be 12 Å wide, giving rise to square shaped clusters, or they can be 8 Å wide, giving rise to clusters that are slightly elongated perpendicular to the substrate
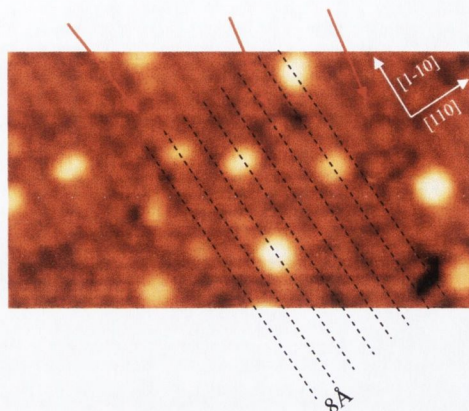
Figure 7.6: (143×76) Å^2 STM image, $I_t = 0.1$ nA, $V_b = +1$ V, of the clusters on Ge(001) showing the registry of the clusters with respect to the substrate. It is also clear from this that along the [110] direction the clusters are always separated by multiples of 8 Å.

dimer rows. The latter type are more common. For tunnelling set-points of $I_t \sim 0.1$ nA and $V_b = +0.7 \rightarrow +2$ V these clusters have highly reproducible apparent corrugation heights of 1.1 ± 0.1 Å, with respect to the underlying substrate, suggesting that they are a single monolayer high. It is clear that the growth process at room temperature is predominated by the formation of these 2D clusters. Some smaller protrusions are also imaged on the surface, and these will be discussed in detail later. It is also important to note that the missing Ge dimer defect density is extremely low. Two such defects are marked with red arrows in figure 7.5.

The exact registry of the clusters with respect to the Ge substrate can be seen from the STM image shown in figure 7.6. The substrate maintains the dimer row structure of Ge(001) and this can be used to ascertain the position of the clusters with respect to the substrate dimers. The dashed lines, along the [1$\bar{1}$0] oriented dimer rows, are separated by 8 Å. As a substrate

reference, it can be seen that these dashed lines pass through local apparent depressions on the substrate surface. As the sample is positively biased, these depressions correspond to the buckled up atoms of frozen Ge dimers, as these are electron rich [107]. The dashed lines always pass through the centre of the clusters, clearly showing that they only nucleate on sites that are 8 Å, or whole multiples of 8 Å, apart in the [110] direction. This periodicity means that they can only be occupying certain locations on the surface with respect to the c(4×2) reconstruction of the substrate. These two possible locations for the (8×12) Å^2 clusters, which in terms of the (2×1) reconstruction are in fact equivalent, are represented schematically on the left of figure 7.7(a). Shown on the right of figure 7.7(a) are the two possible sites for the (12×12) Å^2 clusters. Again these two sites are equivalent in terms of the (2×1) reconstructed surface. How the spacing of the clusters along the [110] direction arises is seen in figure 7.7(c).

Similarly, along the [1$\bar{1}$0] direction, due to the restrictions of the nucleation site, the clusters are spaced by whole multiples of 4 Å. Whether the clusters are 12 Å or 8 Å wide in the [1$\bar{1}$0] direction depends on how many substrate dimers the clusters nucleate across in this direction. The nucleation site is essentially the same for both, but for the 12 Å wide cluster nucleation occurs over three of the [110] oriented dimer rows, whereas for the 8 Å wide clusters nucleation occurs over two [110] oriented dimer rows. This point can be seen from figure 7.7(a).

The 12 Å width of the clusters in the [110] direction cannot be understood by looking only at the Ge surface dimers, which have an 8 Å periodicity along this direction. For the size of the clusters to be dictated by surface dimer rows of the substrate surface layer, one would expect the clusters to have widths that are multiples of 8 Å. The 12 Å width can only be understood if one takes
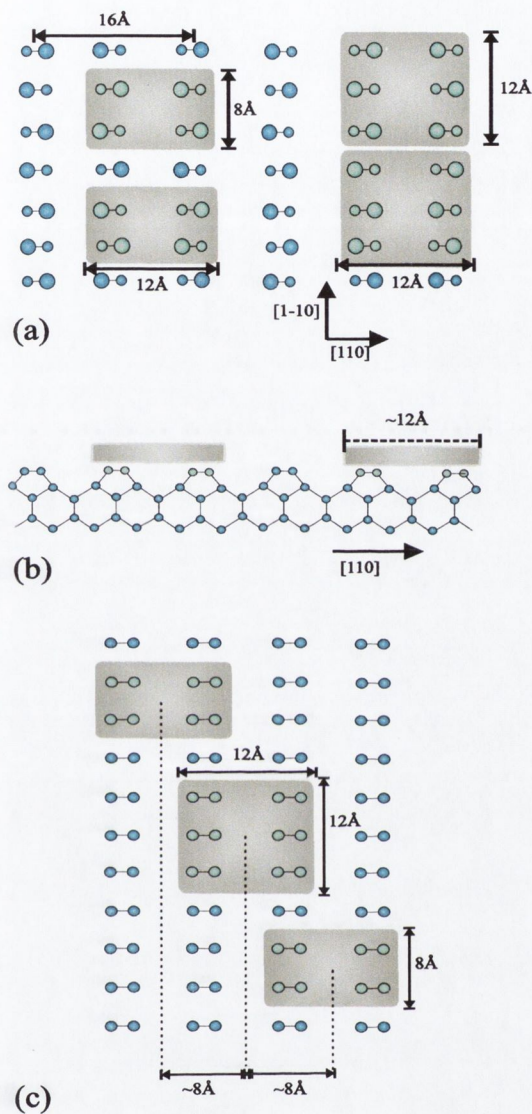
Figure 7.7: (a): Schematic of the clusters with respect to the c(4×2) reconstructed Ge(001) surface. The most common cluster is (12×8) Å^2. This nucleates on one of two possible sites, shown on the left of the figure. Both sites are equivalent for the (2×1) reconstructed surface. On the right are the two possible sites for the (12×12) Å^2 clusters, which are again equivalent for the (2×1) surface. (b): Side view of the nucleation of the clusters, showing the 12 Å width of the clusters relative to the substrate. (c): Schematic showing that the preferred nucleation site is only repeated at 8 Å intervals along the [110] direction, as observed in the STM images.
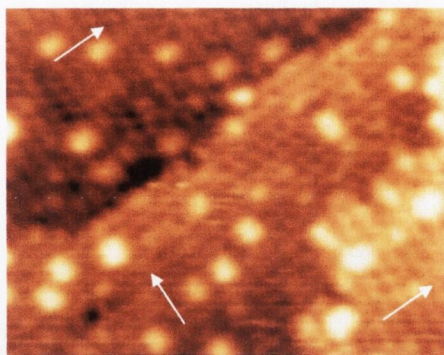
Figure 7.8: (180×140) Å^2 STM image, $I_t = 0.1$ nA, $V_b = +1$ V, showing the rotation by 90° of the clusters from one terrace to the next. The white arrows on each terrace point in the direction of the elongation of the clusters, the [110] direction.

into account the bulk periodicity of Ge. This is shown schematically in figure 7.7(b). The cluster size in the [110] direction is dictated by the periodicity of the second Ge layer, and not by the periodicity of the surface dimers. This indicates that the atoms of the clusters interact not only with the Ge dimers of the surface, but also with those of the subsurface layer.

With regard to the initial nucleation process, it is also worth noting that the (12×8) Å^2 clusters, which are elongated along the [110] direction, can be seen to rotate by 90° between alternating terraces, in keeping with the fact that the dimer rows of the Ge substrate rotate in the same manner. This can be seen in figure 7.8, and illustrates the preference for growth across the dimer row direction, as opposed to along the rows, showing initial nucleation of the islands in the [110] direction to be energetically favourable compared to nucleation along the [1$\bar{1}$0] direction.

7.3.2 Interaction of the Fe Film with the Ge(001) Substrate

Effect of the Fe Film on the Substrate Reconstruction

Following the deposition of the Fe film, the long range (2×1) reconstruction appears to break down somewhat. From the STM image of figure 7.9, it can be seen that the surface does not exhibit any one long range reconstruction. Instead the substrate locally exhibits differing reconstructions over very short ranges. As has previously been mentioned there is an extremely low density of missing Ge dimer defects on the surface, as is evident from STM image figure 7.5. This shows that any breakdown in the (2×1) order is not due to the presence of large numbers of such defects. In the STM image of figure 7.9 small areas of the (2×1) reconstruction can be seen. Other than these small areas, the surface has no long range order, with local areas of the surface that can neither be defined as (2×1) or $c(4\times2)$. For clarity red arrows mark some such disordered areas. Such a disordered surface has never been imaged for the clean, defect free, Ge surface. It is therefore reasonable to suggest that this disorder is due to the presence of the Fe film and that the film is, in some way, pinning the flip-flopping Ge dimers in a manner similar to that of the missing Ge dimer defects, causing local changes in the surface reconstruction. This adsorbate induced changing of the reconstruction is consistent with work by Alverez *et al.* who, using XRD, found that surface contamination (from residual gas, in their experiments) leads to increased temperatures for the $(2\times1)\leftrightarrow(4\times2)$ phase transition, and to a rounding of the transition [140]. Given the dependence of the electronic structure of the Ge(001) surface on the reconstruction that it exhibits, this altering of the Ge surface by the Fe film will undoubtedly effect the electronic properties of the Ge surface and
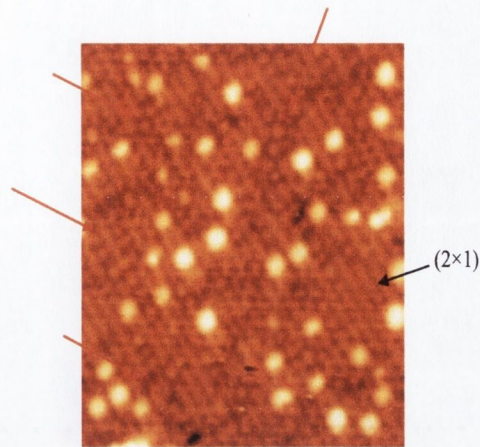
Figure 7.9: (200×250) Å^2 STM image, $I_t = 0.1$ nA, $V_b = +1$ V, of the initial nucleation of Fe on the Ge(001) surface. The surface exhibits regions of disorder, having neither the (2×1) or (4×2) reconstructions. Some of these areas are pointed to with red arrows.

the Fe/Ge(001) interface as a whole.

Fe/Ge Interface: Abrupt or Intermixed?

One of the most important points to be addressed in terms of the Fe/Ge(001) interface is the degree of intermixing in the system. The degree of inter-mixing present greatly influences the properties of spin transport across the interface [7]. Previous surface studies have suggested varying degrees of re-activity of the interface at room temperature, from severe [133, 135], to low level [102, 131]. While the quality of the actual Fe/Ge(001) interface cannot be assessed using STM, some properties of the surface following Fe nucle-ation can be used as an indication of the extent of reactivity. For example, as had already been shown, the corrugation height of the imaged clusters is as expected for a monolayer of Fe on the Ge(001) surface. For intermixing of the

islands with the Ge(001) substrate one would expect a reduced corrugation. Secondly, the Ge substrate maintains its general structure in the areas surrounding the clusters, however with changes in the local reconstruction of the surface evident, as outlined in the previous section. Previous STM studies of metal clusters on Si(111) have shown the formation of very large voids when intermixing occurs [141]. Possible evidence for intermixing between substrate and film is present in the STM images. As mentioned in section 7.3.1, there are some small protrusions imaged on the surface, alongside the clusters. A zoom in on part of a terrace is shown in figure 7.10. Again the characteristic square and rectangular clusters can be seen on the surface. Also imaged are these small protrusions, mostly occupying positions above the [1$\bar{1}$0] oriented Ge dimer rows. They are slightly elongated along the dimer row direction and have an apparent corrugation height of 0.75 Å. For clarity some of these are circled on the STM image. These small protrusions have not been imaged on the clean Ge substrate prior to deposition.

The protrusion have two likely explanations. The first is that they are Fe ad-dimers on the surface. However, given the obvious stability of the larger structure it is unclear why Fe ad-dimers, occupying sites very close to each other, would not go on to form the larger clusters. The second possibility is that they are Ge ad-dimers on the surface. The protrusions imaged here are similar to those imaged in a previous STM study, where Ge was deposited by evaporation onto the Ge(001) surface and Ge ad-dimers formed [142]. The most stable configuration was for ad-dimers occupy sites above the dimer row, with the ad-dimer elongated along the [1$\bar{1}$0] direction. If the protrusions imaged here are Ge, it would suggest a degree of intermixing at the interface. As there are few missing Ge dimer defects imaged on the substrate, the most likely source of the Ge would be that it has been ejected from the
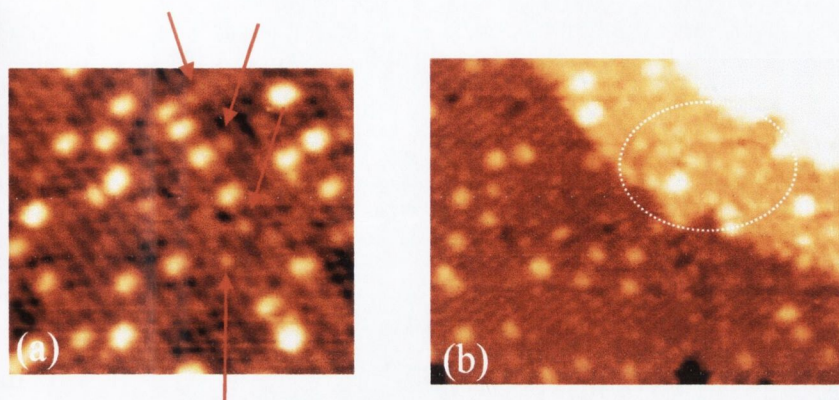
Figure 7.10: (a): (143×123) Å^2 STM image, as in Fig.7.5. The small protrusions imaged on the surface are pointed to by red arrows. (b): (210×170) Å^2 STM image, $I_t = 0.1$ nA, $V_b = +1$ V. An area with a very high concentration of these protrusions, and few of the (12×8) Å^2 clusters is circled.

substrate following deposition of the film. This would result in Ge vacancy sites, or the substitution of Fe for Ge. As there are few such vacancy sites imaged, if they exist they must be beneath the imaged islands. The similarity with previously imaged Ge ad-dimers points towards these being the same. However, as seen in the circled area of figure 7.10(b), the concentration of these protrusions can be very high in areas with few of the (12×8) Å^2 clusters. If the Fe is causing Ge to be ejected from the substrate, one would not expect a high concentration of them in an area with few of the (12×8) Å^2 clusters. Unfortunately, it is not possible to conclusively show whether these small protrusions are Fe or Ge.

In summary the STM images show that the Ge substrate maintains its structure in the areas surrounding the (12×8) Å^2 clusters. No large voids are imaged and the clusters have apparent heights consistent with a single monolayer of Fe. However, localised intermixing in the immediate area of the
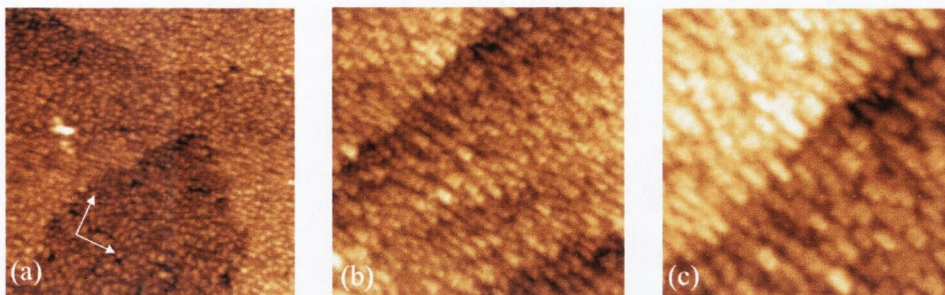
Figure 7.11: (a): (1300×1300) Å^2 STM image showing the Ge(001) surface following the deposition of Fe film of nominal thickness 0.7 Å. The STM image is consistent with the formation of ∼ 0.8 - 1 ML Fe film. A preference for growth of the islands along the [110] and [1$\bar{1}$0] directions, indicated with arrows, can be discerned. (b): (810×810) Å^2 STM image of the same surface. This shows that the Fe film has preferential growth in one direction in this area of the surface. (c): (500×500) Å^2 STM image showing the nucleation of the Fe film across a step edge. All images I_t = 0.1 nA, V_b = -1.8 V.

imaged clusters, resulting in a Fe-Ge alloy, cannot be ruled out.

7.3.3   Increased Fe Film Thickness

We have shown that the initial stages of Fe nucleation on Ge(001) at room temperature results in the formation of well ordered clusters, with a definite registry with respect to the Ge(001) substrate. This extremely well ordered nucleation is seen for very low deposition thickness. STM images of the Ge(001) surface following the deposition of a 0.65 Å thick Fe film at room temperature are shown in figure 7.11. From the image, this corresponds to a ∼ 0.8 - 1 ML Fe film. A closed film is not formed, instead islands having heights of 1.1 and 2.2 Å, with the latter in the majority, are imaged, and the bare Ge(001) surface is imaged between these islands. These directions form
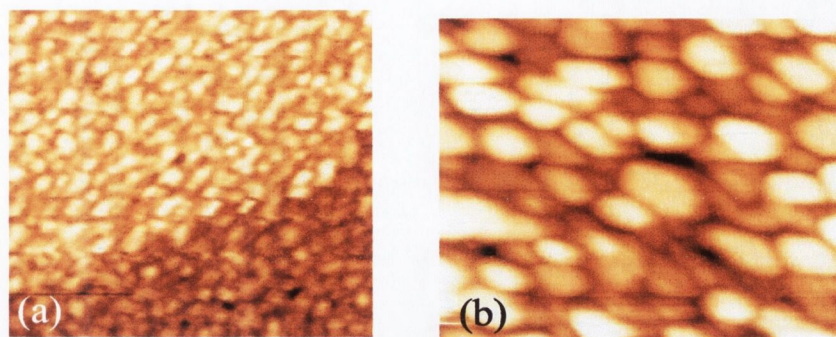
Figure 7.12: (a): (440×420) Å^2 STM image, $I_t = 0.1$ nA, $V_b = +1$ V, showing the Ge(001) surface following the deposition of Fe film of nominal thickness 1 Å, which is ~ 1.2 ML (b): (480×420) Å^2 STM image, $I_t = 0.1$ nA, $V_b = +1$ V, following deposition of film of nominal thickness 2 Å, which is ~ 2.4 ML.

the terrace edges of the Ge(001) surface, as denoted by the white arrows in figure 7.11(a), and it can be clearly seen from this STM image that the film preferentially nucleates in either of these two directions. From figure 7.11(b) it is clear that the preferred growth direction of the islands does not rotate direction by 90 ° from one terrace to the next. This indicates that for Fe films of thickness ~ 0.8 - 1 ML, while the islands do show a preference to nucleate in either the [110] or [1$\bar{1}$0] directions, they do not show a preference for one direction above the other. Indeed in the STM image of figure 7.11(c) the Fe film can be seen to continue nucleating in the same direction across a terrace step.

STM images of films of nominal thickness 1 Å and 2 Å are shown in figure 7.12(a) and (b) respectively. Again a closed Fe film is not formed on the surface, consistent with Volmer-Weber growth, and the Ge substrate can be seen underneath the Fe islands at all stages of film nucleation imaged. The 2 Å film results a very rough surface, with the presence of large islands

with heights up to 6.6 Å. The two STM images are of similar size, showing that as the Fe coverage is increased the average Fe island size is larger.

The imaged growth mode for these films offers an explanation as to why Ma *et al.* [131] and Cantoni *et al.* [102] have found the first monolayers of Fe on Ge(001) to be magnetically dead at room temperature. STM reveals that the initial growth is of the Volmer Weber type, which is not conducive to long range magnetic order of the Fe thin films at room temperature.

7.4   Deposition of Fe at Elevated Substrate Temperature of 200°C

Sub-monolayer growth of Fe onto the Ge(001) surface at elevated substrate temperature of 200°C has also been studied. Repeating the deposition of $\sim$ 0.15 - 0.35 ML Fe films for elevated substrate temperature, it was found that the 12 Å wide clusters that form at room temperature do not form. Instead, the most common structure is a beaded, or chain-like island, elongated perpendicular to the dimer row direction. Rectangular islands, which are higher than the chain-like islands, also form on the surface. STM images of the type of structure that form on the surface are shown in figure 7.13. For tunnelling conditions $I_t \sim 0.1$ nA and $V_b = +0.7 \rightarrow +2$ V, the chains, a zoom in of which shown in figure 7.13(c), can have corrugation heights of 1.1 and 2.2 Å, consistent with 1 and 2 ML of Fe respectively. Along the [110] direction there is a 16 Å periodicity and in this direction the FWHM of the component clusters that form these islands is $\sim$ 12 Å. In the [1$\bar{1}$0] direction the islands are either 12 Å or 24 Å wide. It is clear that the clusters making up the chain island are similar those that form at room temperature, suggesting that the elongated islands that form at elevated substrate temperature are made up of
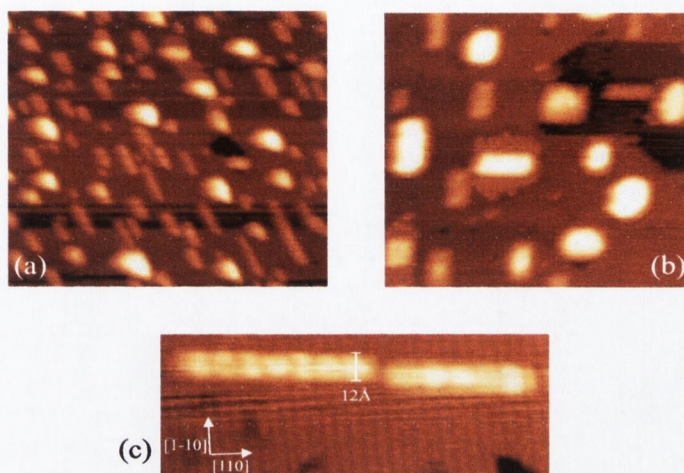
Figure 7.13: (a): (780×740) Å^2 STM image showing nucleation of Fe at el-evated substrate temperature. Chain-like islands nucleate on the surface. These are 1 or 2 ML high. Higher islands (seen brighter in the image) are not as elongated. (b): (320×320) Å^2 STM image showing the rectangular islands that also form for elevated substrate temperature. These islands are higher than the chains, forming for 3-6 ML of Fe. It can be seen that there is a preference for elongation across the dimer rows. (c): (200×80) Å^2 STM high resolution zoom-in of one of the chain-like islands. It can be seen that the islands nucleate across the dimer row direction. In the [1$\bar{1}$0] direction the islands are 12 Å wide, and the periodicity of clusters that form the islands is 16 Å along the [110] direction. All images I$_t$ = 0.5 nA, V$_b$ = -1.8 V.
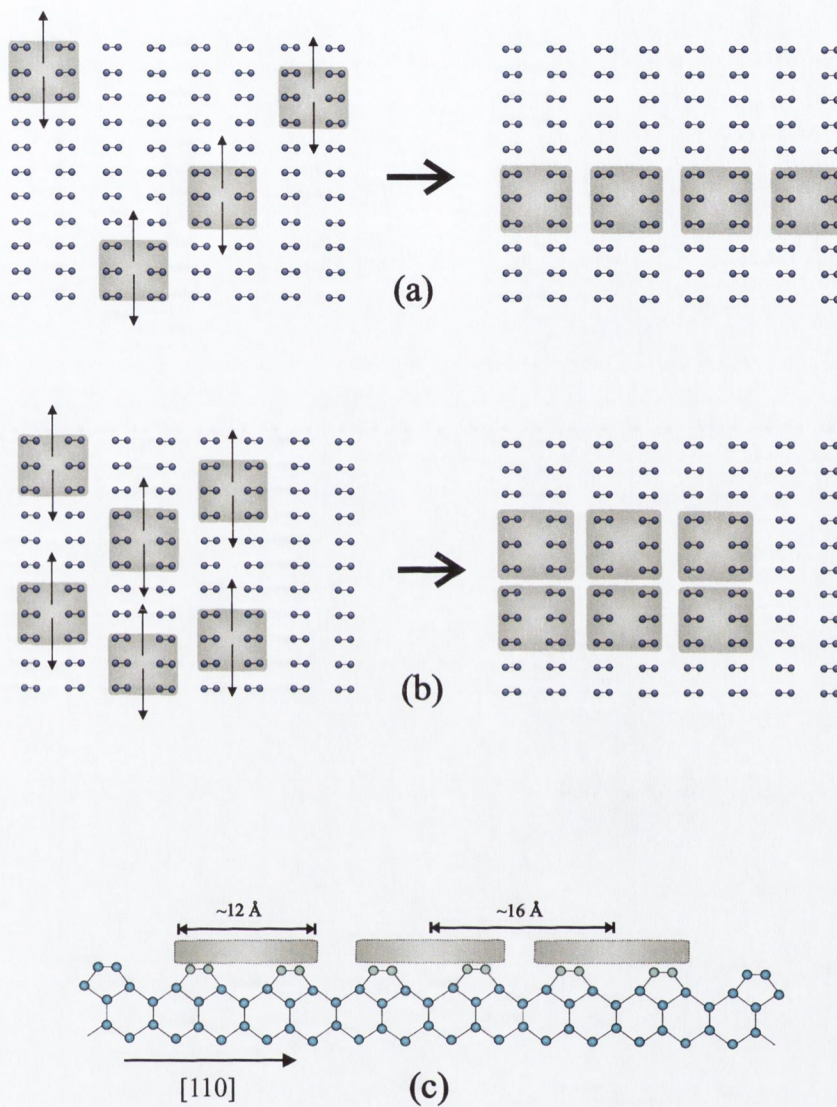
Figure 7.14: (a): Formation mechanism of the elongated chains. The 12 Å wide clusters nucleate together to form the islands elongated along the [110] direction. (b): Formation mechanism of the rectangular islands. The shape of the island depends on the local concentration of the 12 Å wide clusters. (c): Side view of the chains, showing how the 16 Å periodicity along the [110] direction arises due to the registry of the constituent 12 Å clusters.

these smaller cluster. As the islands are elongated along the [110] direction, it appears that the formation mechanism involves anisotropic diffusion of the 12 Å wide clusters on the surface, with a preference for diffusion along the [1$\bar{1}$0] direction. The chains form when the diffusing clusters meet neighbouring clusters, which must constitute a barrier to further diffusion. Whether chains or the rectangular islands form then depends on the local concentration of the (12×8) Å^2 clusters. A model of the formation mechanism of the islands, and the registry of the chain like islands, is shown in figure 7.14. It can be seen from this how the 16 Å periodicity in the [110] direction arises from the merging of the smaller 12 Å wide clusters.

The rectangular islands, which can be seen in the STM image of figure 7.13(b), still show a preference for growth along the [110] direction, but with a much reduced aspect ratio compared to the chain-like islands. Whereas the chain-like islands have apparent corrugation heights of 1.1 and 2.2 Å, the rectangular islands have heights of 3.3 - 6.6 Å, in multiples of 1.1 Å. This increased height of the more rectangular island is obvious from the STM images, as the aspect ratio of the brighter islands is clearly reduced with respect to the less bright (and thus lower) islands. In summary, for Ge(001) substrate temperature of 200°C, Fe islands of 1 to 2 monolayers high form chain-like islands, whereas for islands of 3 - 6 monolayers in height the aspect ratio reduces and 3D islands are more energetically favourable. Both island types show a preference for growth in the [110] direction, i.e. across the Ge dimer rows, which suggests anisotropic diffusion of the constituent clusters.
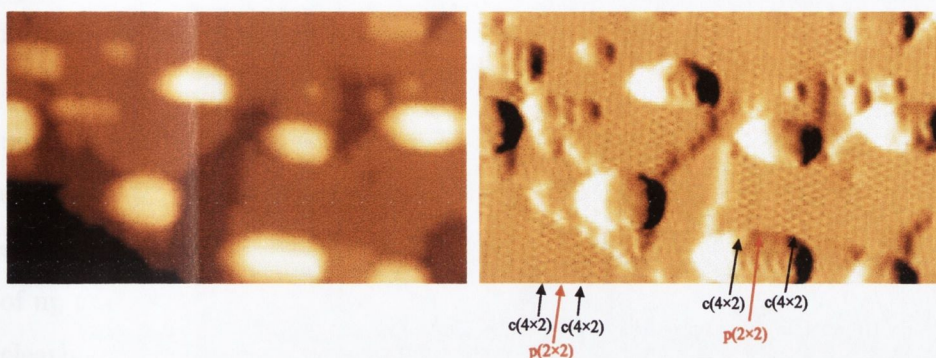
Figure 7.15: (360×200) Å^2 STM image, I_t = 0.5 nA, V_b = -1.5 V, of the Ge(001) surface following the deposition of $\sim$ 0.35 ML of Fe at substrate temperature of 200°C. The derivative of the image is shown, right. The Ge substrate forms a domain structure with neighbouring areas of p(2×2) and c(4×2) reconstructions, some of which are marked with arrows.

7.4.1 Influence of Fe Deposited at Elevated Substrate Temperature on the Ge(001) Surface

For room temperature deposition it was shown that the Fe film can alter the reconstruction of the underlying Ge substrate and result in the appearance ad-dimer protrusion type defects on the surface. The appearance of these ad-dimers could possibly be due to intermixing at the interface. If intermixing does occur at room temperature, one would expect it to be more evident at elevated temperature. It is therefore of interest to analyse the Fe films deposited at elevated substrate temperature in terms of Fe interaction with the substrate.

In terms of this, the first point of interest is that, from the images presented in figure 7.13, it is clear that the area of the Ge substrate not covered with islands maintains its general structure following deposition of the Fe film at a substrate temperature of 200°C. The Ge dimer rows are still clearly

imaged following the deposition of the Fe film. Indeed, the substrate appears more ordered than for room temperature deposition of films of similar thickness. This point is even more evident in the STM image of figure 7.15, which shows the Ge(001) surface following the deposition of ~ 0.35 ML of Fe at substrate temperature of 200°C. Rectangular islands, with corrugation heights of up to ~ 6.6 Å, form on the surface. The dimer rows of the Ge surface are clearly seen alongside the islands, and the Ge substrate is virtually defect free, with only one missing Ge dimer type defect imaged. This extremely low concentration of substrate defects is not consistent with intermixing over the entirety of the substrate, however, once again it is possible that the area of the islands themselves are an intermixed phase.

Most interestingly, the dimer rows of the Ge substrate do not exhibit the (2×1) reconstruction expected for the surface at room temperature. Instead it exhibits a striped domain pattern, seen more clearly in the differentiated image. The pattern forms over the the entirety of the STM image. We recall, from section 6.3.1 that a striped domain pattern, with alternating domains of the (2×1) and $c(4 \times 2)$ reconstructions, has been imaged by Zandvliet *et al.* [119] at room temperature, on a surface with an extremely low defect density. Indeed, the presence of less than 0.05% surface defects (number of vacancies and adclusters divided by number of surface atoms) was found to destroy it. However, the striped domain pattern imaged here differs markedly from that imaged by Zandvliet *et al.*, firstly in that the domains form over much smaller distances, and secondly, in that the (2×1) reconstruction is not present at all. The $c(4 \times 2)$ reconstruction is most evident, and between the $c(4 \times 2)$ areas domain boundaries form. The area of the domain boundaries have a $p(2 \times 2)$ symmetry, however due to their small size it is debatable whether the areas can actually be called a $p(2 \times 2)$ reconstructed surface.

The c(4×2) reconstruction, and also the p(2×2) reconstruction, are associated with the Ge(001) surface at low temperature, when the Ge dimers no longer have enough energy to flip-flop back and forth between the two degenerate buckled configurations and the dimers are thus frozen in these patterns. As the surface imaged here is at room temperature, one would not expect to image such an arrangement. Indeed, to our knowledge the p(2×2) reconstruction has only been imaged at T< 200 K [114]. Despite calculations suggesting the c(4×2) and p(2×2) reconstructions are degenerate [113], the fact that the c(4×2) reconstruction dominates here is consistent with its observation at room temperature which suggests that it forms more readily than the p(2×2) reconstruction. The most reasonable suggestion for the existence of this mixed domain surface at room temperature is that the imaged islands interact with the Ge dimers to inhibit the flip-flopping motion associated with the (2×1) reconstruction. This freezing of the dimers results in the observation of surface reconstruction usually observed at low temperature. The fact that the surface exhibits the domain structure over the entirety of the imaged surface suggests that the Fe islands interact with the Ge(001) substrate over reasonably long length scales.

Whilst the islands formed at elevated substrate temperature clearly influence the substrate reconstruction over long ranges, the Ge(001) surface still maintains its dimer row structure, and exhibits known reconstructions. Even in very close proximity of the islands the substrate is well ordered. The possibility of the substrate surface consisting of an ordered Fe-Ge phase following deposition is highly unlikely as the surface structure, atomic corrugation heights and surface band gap is as for clean Ge(001). Furthermore the substrate does not exhibit an increase in the defect density compared to pre deposition surfaces. This suggests that, while it is still possible that the

islands themselves consist of an intermixed phase, the surrounding substrate is not affected, even for a substrate deposition temperature of 200°C.

7.5 Effect of Post Annealing on the Fe/Ge(001) Interface

7.5.1 AES Data

A 3 Å Fe film was deposited onto a clean Ge(001) sample, using the parameters outlined in section **??**. Auger spectroscopy was performed on the sample following RT temperature deposition and then following UHV annealing for 15 minutes at 150°C, 300°C, 450°C and 600°C. Each AES scan took ∼ 30 minutes in total. Following each AES scan the sample was immediately annealed at the next temperature and AES performed again. The background pressure was 4.66×10^{-10} mbar , rising to 8×10^{-10} mbar during the annealing cycles. The spectra are presented in figure 7.16. It is clear that there is a large decrease in the Fe concentrate at the surface following annealing at 150°C. The concentration is then relatively stable, with only slight reductions in the Fe concentration following each temperature increase, until annealing at 600°C results in the Fe concentration at the surface almost disappearing. This is similar to what has been described by Ma *et al.* [131], and they propose that the rapid decrease in Fe concentration at 160°C, that they observed, is due to interdiffusion.

7.5.2 STM Data

As already stated, the stability of the Fe/Ge(001) interface at elevated temperature is an important issue, especially with regard to the onset of inter-
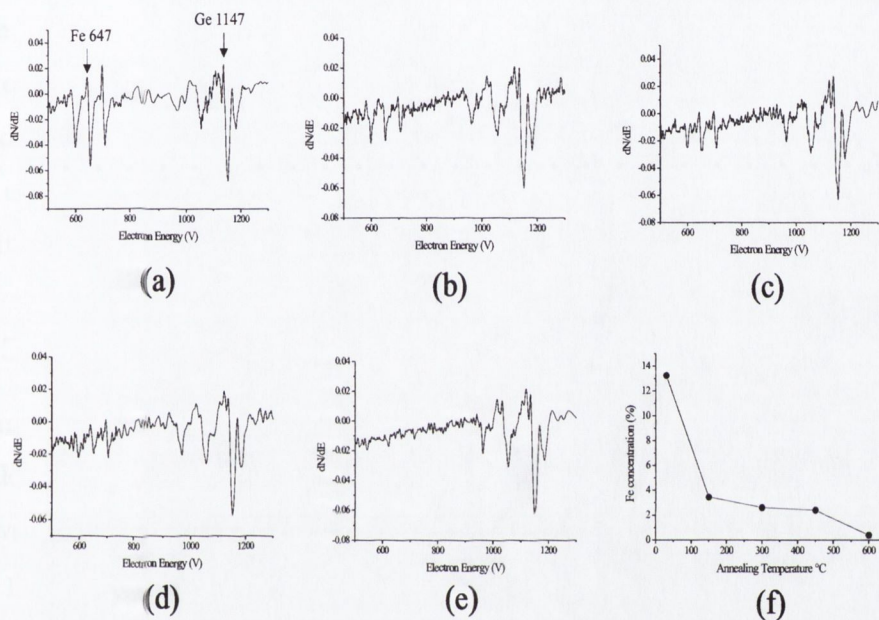
Figure 7.16: Auger spectra for step-wise annealing of 3 Å film on Ge(001). Spectra (a) is for RT, (b) through (e) are following step-wise annealing at increasing temperatures of 150°C, 300°C, 450°C and 600°C. Graph (f) gives an overview on the effect of aggregate annealing on the Fe surface concentration as measured by AES.

mixing or interface degradation. AES does not provide conclusive evidence that the concentration changes are due to intermixing, as such an increase can also be explained in terms of 3D island formation following annealing. Therefore the stability of the interface to annealing was investigated with STM. A 0.5 Å Fe film was deposited onto the clean Ge(001) surface, with the substrate at room temperature. An STM image of a similar surface has already been shown in 7.11(a), showing the deposited Fe to form small 1.1 Å and 2.2 Å high islands on the surface. The sample was post annealed step-wise at elevated temperature and after each anneal the sample was characterised using STM.

7.5.3 Annealing to 350°C

Firstly, the sample was annealed at 160°C for 15 minutes. An STM image following this anneal is shown in figure 7.17(a). Merging of the Fe islands is very evident, with a large increase in the exposed Ge substrate compared to prior to annealing. There is no evidence in STM images for large scale intermixing occurring at this temperature, showing instead that the increase in the AES Ge/Fe ratio is in fact due to the Fe islands coalescing to form larger islands than are present following evaporation at room temperature.

For post-annealing of the sample at temperatures up to 350°C, STM reveals a continuous merging of the Fe islands, a transition from 2D to 3D islands, which can be associated to the increase in the Ge/Fe ratio of AES. This is evident from the STM image of figure 7.17(b), which shows the surface following a 15 minute anneal at 350°C. The Fe islands have further merged, forming rectangular 3D islands of up to 10 ML in height. The characteristic dimer rows of the Ge(001) surface is still seen on this type of surface, showing that the structure of the Ge(001) surface is maintained, and suggesting
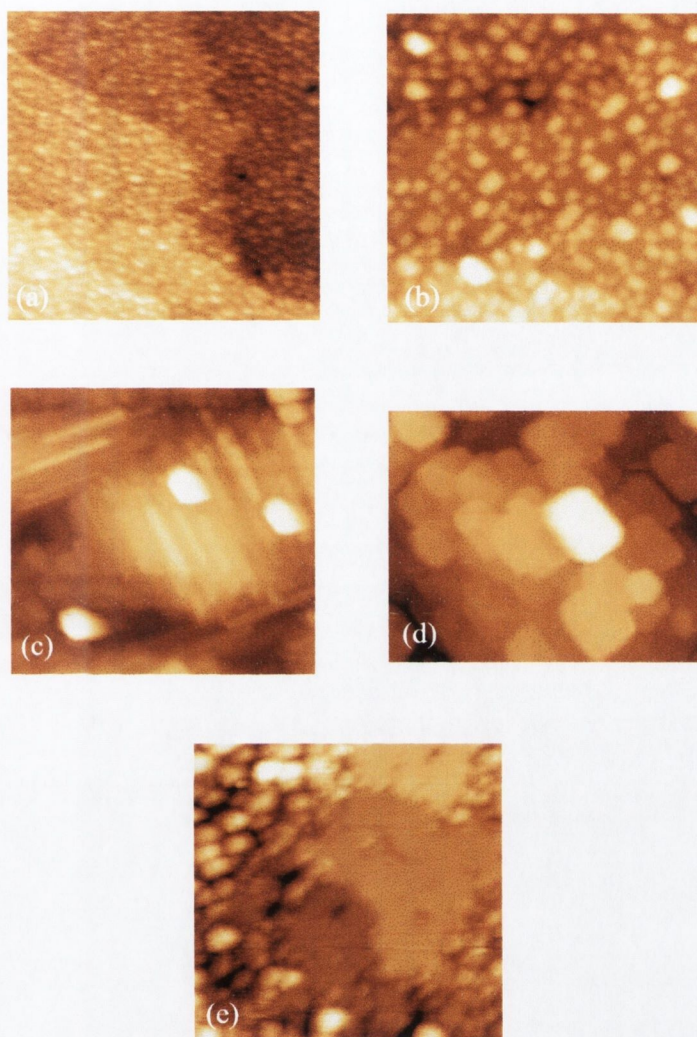
Figure 7.17: (a): (520×520) Å² STM image of 0.5 Å Fe film on Ge(001) following 15 minute anneal at 160°C in UHV. I_t = 0.1 nA, Vb = -1.8 V. (b): (530×530) Å² STM image of the same film, following 15 minute anneal at 350°C in UHV. I_t = 0.1 nA, Vb = -1.8 V. A merging of the Fe islands to form larger 3D islands is evident. (c): (710×680) Å² STM image of the surface following annealing in UHV for 15 minutes at 450°C. I_t = 1 nA, Vb = +1 V. A dramatic change in the surface, consistent with the formation of an intermixed surface layer, is imaged. (d): (550×450) Å² STM image showing a different area of the intermixed surface formed following annealing at 450°C. I_t = 1 nA, Vb = +1 V. (e): (370×370) Å² STM image of the surface following 15 min anneal at 600°C. I_t = 0.1 nA, Vb = -1.8 V. A highly defective Ge dimer row surface re-emerges, suggesting that the Fe has diffused into the bulk.

large scale Fe-Ge intermixing still has not occurred. Throughout these post annealing experiments the surface still exhibits the (2×1) LEED mesh. It is also interesting to note that following this annealing step the Fe islands show some preference for elongation across the dimer row direction. This can be seen from figure 7.17(b), where the elongation direction of many of the islands rotate by 90° from one terrace to the next. This elongation of the rectangular Fe islands is the same as was seen for the islands formed following Fe evaporation at an elevated substrate temperature in section 7.4.

7.5.4   Annealing at 600°C

The sample was then annealed for 15 minutes at 450°C. AES shows the Ge/Fe ratio to be similar before and after this annealing step. STM images of the surface following this anneal are shown in figure 7.17(c) and (d). The surface has completely changed from previous images. All evidence of the Fe islands, on a well formed Ge(001) substrate is gone. Instead large rectangular disordered islands are imaged. They do not form terraces, but the island edges are aligned at 90° to each other, in-keeping with the cubic symmetry of the Ge substrate. This transformation of the surface as seen by STM is also accompanied by a streaking, primarily along the [110] and [1$\bar{1}$0] directions, of a previously sharp (2×1) LEED mesh. Due to the low coverage of deposited Fe, it is impossible that these islands are pure Fe. Therefore the surface is best explained in terms of the formation of Fe-Ge intermixed phase at the surface following annealing temperatures of $\sim$ 450°C.

Further annealing of the sample, at 600°C for 15 minutes, results in another transformation of the surface. The dimer rows of the Ge surface reappear, however, as seen in figure 7.17(e) the terraces formed are small and the surface highly defective. The Fe/Ge concentration of the AES has de-

creased to a stage where it is only slightly above the detection limit of the analyser. This consistent with diffusion of Fe into the bulk Ge causing the reappearance of the Ge dimer rows. The (2×1) LEED mesh returns following this high temperature annealing. Even at this temperature there still remains some small areas consistent with an amorphous intermixed phase, as seen on the left side of figure 7.17(e). This suggests that if complete diffusion of Fe into the bulk Ge does occur then annealing temperatures of $> 600°C$ are necessary.

7.6 Scanning Tunnelling Spectroscopy of the Fe/Ge(001) Surface

7.6.1 STS of Fe Clusters Formed During Initial Nucleation at Room Temperature

Scanning tunnelling spectroscopy has been performed on the surface following the initial nucleation of the clusters described in section 7.3.1. For data presented here the tip sample distance was determined by $V_b = + 1.8$ V, and $I_t = 0.1$nA. A I(V) spectrum, taken on the surface shown in figure 7.5, of both the (12×12) Å^2 and (12×8) Å^2 clusters nucleating on the Ge substrate, is shown in figure 7.18. The differentiated curve is also presented. The curve representing the clusters is an average of ~ 400 curves taken on top of the (12×12) Å^2 and (12×8) Å^2 clusters, and the one representing the Ge substrate is also an average of 400 curves. From the tunnelling spectra, it is clear that these monolayer high clusters are not metallic at room temperature. From the STS spectra they have a conductivity gap similar to that of the Ge substrate itself, with at most a reduction of the gap to ~ 0.7 eV
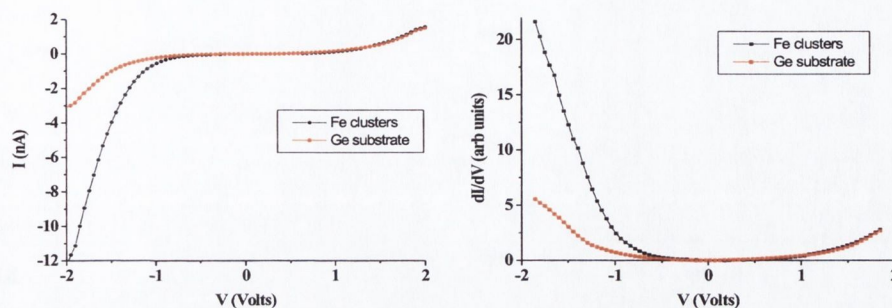
Figure 7.18: Tunneling I(V) spectrum of the (12×12) Å^2 and (12×8) Å^2 clusters on the Ge(001) surface (black), and the underlying substrate (red). The clusters have a conductivity gap of ~ 0.7 eV, and are highly asymmetric. The asymmetry is consistent with a Schottky diode behaviour. The derivative of the curve is also shown.

compared to ~ 0.8 eV measured for the Ge(001) surface. This gap value is measured from the FWHM of the normalised spectra. It is clear the the clusters are not yet metallic, and the similarity of the band gap they exhibit with that of the substrate suggest that the surrounding semiconductor dictates the measured gap. Non-metallicity of nanoscale clusters of metal materials on semiconducting substrates has been observed in references [143, 144].

It is also immediately obvious that the I(V) characteristics above the clusters is highly asymmetric. The tunnel current increases dramatically for negative bias greater than $\sim$ -1 V, resembling Schottky diode behaviour. This increased current for negative sample bias shows the system to be forward biased when applying a negative sample bias. This is as expected for a Schottky barrier formed on an n-type substrate. The diode behaviour suggests that a space charge region, or depletion layer, forms near the surface. The conductivity band of the Ge substrate shifts upward at the interface

with the cluster, resulting in the formation of a depletion layer, which gives rise to the Schottky type behaviour seen with STS. Asymmetric tunneling I(V) spectra have previously been observed for non-metallic 3 nm high Au clusters on p-Si(111) by Radojkovic *et al.* [144]. The clusters here are much smaller, and show that Schottky behaviour can occur for clusters that are not yet metallic.

7.6.2 STS of 0.5 Å Fe Film on Ge(001) Surface

STS was also carried out on surfaces similar to that imaged in figure 7.11, which is the Ge(001) surface following the deposition of $\sim$ 0.5 Å Fe film. A closed Fe film is not formed, the surface being characterised by mainly 2 ML high Fe islands. An STM image of the surface, and two STS maps, are shown in figure 7.19. The STS maps presented are for +0.15 V and -0.15 V sample bias. This is to illustrate that within what is the band gap of the Ge substrate, states due to the Fe film are resolved. Only within a $\sim$ 0.15 V region around 0 V do the I(V) maps show no contrast. This is conclusive evidence that the deposited Fe results in the formation of these islands. This move towards metallicity of the islands is also evident from the STS curve presented. This is the average of every curve taken during scanning within the dashed box in the STM image. It therefore represent the averaged contributions of all of the Fe islands and also the Ge substrate. Within this dashed box the Fe islands are almost exclusively 2 ML in height. The curve shows that the surface does not have a significant bandgap, indicating that these 2 ML high islands no longer exhibit the semiconducting behaviour of the (12×12) Å^2 and (12×8) Å^2 clusters. The STS curves still shows a change in slope around E$_f$, showing that the surface is still not perfectly metallic.

By examining single spectroscopy points on this surface the contributions
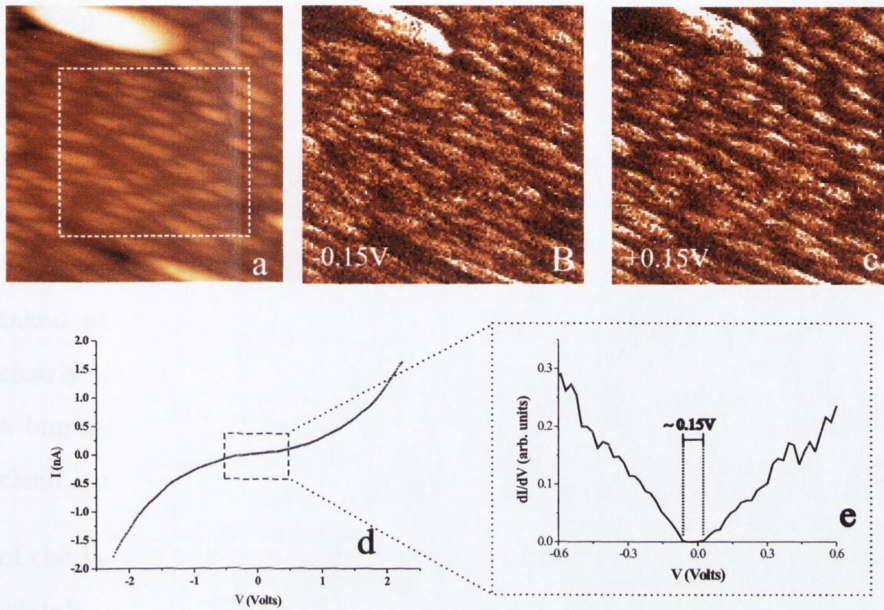
Figure 7.19: (a): STM image of the surface following deposition of the 0.5 Å Fe film. (b): STS map of the surface for V_b = -0.15 V. (c): STS map of the surface for V_b = 0.15 V. Both maps show that the Fe film is resolved, and therefore has conducting states, in the band gap region of the Ge substrate. (d): I(V) spectra for the entire region inside the dashed box. Islands inside are almost exclusively 2 ML high. (e): A differentiated zoom-in of the I(V) spectra for the region near E_f, showing that following deposition of the Fe film, the surface does not exhibit a large band gap ($\sim$ 0.15 V), pointing to a transition towards metallic behaviour.

Figure 7.20: I(V) curve on the Fe island (black), and the adjacent substrate, taken at the points shown in the inset STM image. The Fe curve again clearly shows a move toward metallic behaviour. The Ge substrate still has a bandgap, however it is now reduced to ∼ 0.4 eV, from ∼ 0.8 eV for the clean surface.

of the Fe islands and Ge substrate can be separated, and the effect of the Fe islands on the electronic properties of the Ge substrate can be seen. Figure 7.20 sho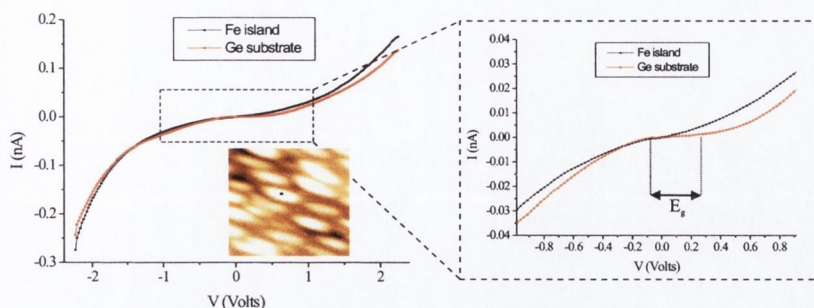ws an I(V) curve for an Fe islands, alongside an I(V) curve of the Ge substrate surrounded by these Fe islands. The points from which the curves are taken are shown in the inset STM image. These single point curves are highly reproducible within the same areas of the surface. As seen from the averaged curve in the previous section, the Fe islands move towards metallic behaviour, with a very small conductivity gap region measured. The Ge surface still exhibits a semiconducting gap, however it is much reduced compared to the clean Ge(001) surface. The bandgap for the clean surface was found to be ∼ 0.8 eV, whereas the bandgap here is ∼ 0.4 eV. These states within the band gap region are induced by the presence of the Fe clusters on the surface. Using STM, First *et al.* [143] have shown that metal cluster induced states exist within the GaAs bandgap in the proximity of the Fe

clusters. More recently, Reusch *et al.* [145] have imaged such metal induced states using an STM in cross sectional configuration at a Au/GaAs(110) interface. It is clear from the STS data presented here that the Fe/Ge(001) interface also results in the semiconductor substrate exhibiting such metal induced states within the bandgap.

Chapter 8

Formation and

Characterisation of Iron Oxide

on the Ge(001) surface

8.1   Introduction

Integration of spin polarised carriers into existing technologies is a major issue in the field of spin electronics and it is therefore of interest to study the formation of proposed half metals on semiconductor substrates [11,12]. As shown by Schmidt [146], successful spin injection into a semiconductor requires either spin polarisations of close to 100%, or the close matching of the conductivities of the semiconductor and source. Therefore the use of materials with a relatively wide bandgap, and a source of 100% spin polarised carriers, such as CrO_2 and Fe_3O_4 is desirable for this purpose [7]. Another advantage of magnetite is that it has a suitably high T_c value for device operation. Furthermore, most known magnetic semiconductors are sources of spin polarised holes, whereas CrO_2 and Fe_3O_4 are sources of spin polarised

125

electrons. Polarised electrons have been shown to have relatively large spin scattering lengths in GaAs [129]. As this has not been demonstrated for polarised hole carriers, a source of spin polarised electrons is preferable.

In this chapter a study of the oxidation of Fe films deposited on Ge(001) substrates is presented. The oxide formed is characterised with AES, LEED and STM/STS. This characterisation points to the formation of magnetite (001). The onset of intermixing due to increased annealing temperature is discussed.

8.2 Deposition of 50 Å Fe/Ge(001)

The Ge(001) surface was prepared as previously described in section 7.2.1. AES showed contamination at the surface to be below the detection limit of the Auger analyser. LEED exhibited the (2×1) mesh, and STM imaged the Ge dimer rows, oriented along the [1$\bar{1}$0] direction, characteristic of the clean Ge surface. Following this, $\sim$ 50 Å Fe films were deposited onto the Ge(001) surface, from an ultrapure Fe rod source, at a rate of 2 Å/min. The chamber pressure during deposition did not exceed 1×10^{-9} mbar. An AES spectrum of the surface following the evaporation of a 40 Å film is shown in 8.1. It can be seen that the only peaks present are those of elemental Fe. The low energy peak at 47 eV is as expected for elemental Fe [147]. Low energy peaks of Ge are not resolved. As has been seen by Ma *et al.* [131], the LEED mesh of this film is consistent with the growth of bcc iron. Such a LEED mesh can be seen in figure 8.1(c). The growth takes place with the Fe [100] direction parallel to the Ge [100] direction. The primitive unit cell of the LEED mesh is twice that of Ge(001) surface, for the same beam energy. This yields a lattice constant half that of Ge(001), which is consistent with the growth of
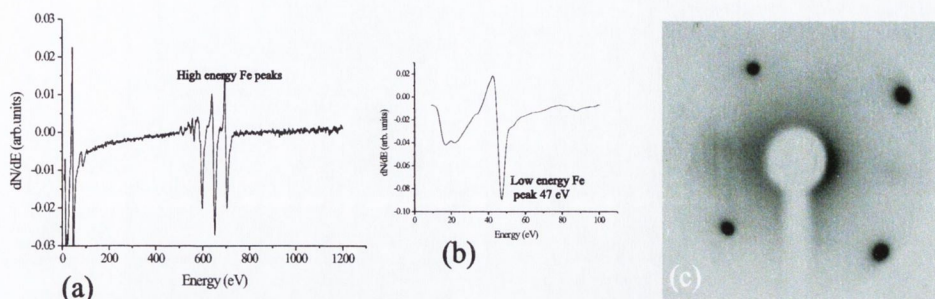
Figure 8.1: (a): Auger spectrum of 50 Å thick Fe film deposited on Ge(001) substrate. Only peaks associated with elemental Fe are resolved. (b): Low energy peak at 47 eV as expected for elemental Fe. (c): LEED mesh of the surface, with beam energy of 46 eV. The primitive unit cell of the LEED mesh is cubic, and double that of Ge(001).

bcc Fe with a lattice constant of 2.87 Å.

8.3   Oxidation of Fe/Ge(001) Films

8.3.1   Oxidation at 200°C and 300°C

Following deposition of the 50 Å Fe films, they were oxidised in 5×10^{-6} Torr O_2, for 10 min, at temperatures from 200°C to 300°C. The results were found to be independent of the annealing temperature, within this range. This oxidation procedure has been used successfully by Dedkov *et al.* and Fonin *et al.* to obtain thin films of magnetite (111) on W(110) and Al_2O_3(111) respectively [67,68]. A representative Auger spectrum following oxidation is shown in figure 8.2(a). Comparing this to figure 8.1, it is clear to see that the described procedure has resulted in oxidation of the Fe film. The oxygen to iron ratio of the surface is 1.56 ± 0.05. The single peak at 47 eV, associated
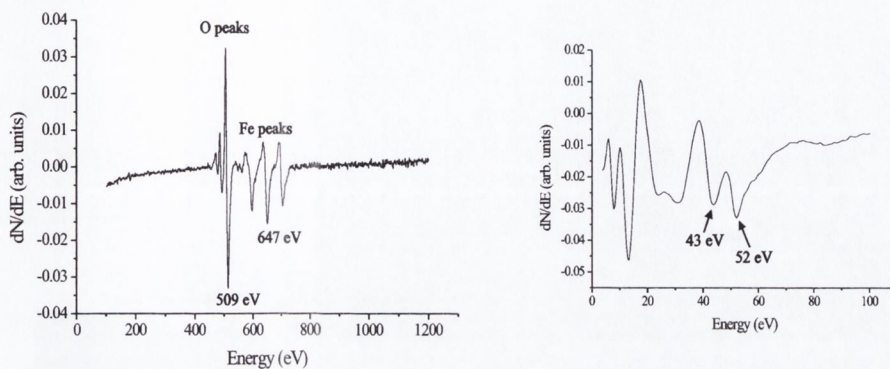
Figure 8.2: Auger spectrum of 50 Å thick Fe film on Ge(001) following oxi-
dation at 300°C, as described in text.

with elemental Fe, is replaced by two peaks at 43 eV and 52 eV, with the
intensity of the latter being greater. While this is indicative of the presence
of an iron oxide phase at the surface the use of these low energy peaks to
accurately ascribe the oxide type is unreliable [93]. One of the most important
points to be taken from the AES spectrum is that there is no evidence for the
presence of Ge at the surface. It must be noted, however that the possibility
of intermixing closer to the interface region cannot be excluded using AES.

A LEED mesh of this surface, taken with a beam energy of 89 eV, is shown
in figure 8.3(a). A LEED mesh of the $(\sqrt{2} \times \sqrt{2})R45°$ reconstructed magnetite
(001) single crystal surface, obtained using the same LEED parameters, is
also shown. Comparison of the two meshes shows that the unit cell of the
oxidised Fe thin film is the same as that of the unreconstructed unit cell of
the magnetite (001) single crystal. This (6×6) Å^2 unit cell is marked in both
photos by a red dashed square. It is clear from this that the oxidised thin Fe
film, on Ge(001), forms a structure consistent with that of unreconstructed
magnetite (001). The absence of the $(\sqrt{2} \times \sqrt{2})R45°$ reconstruction for the
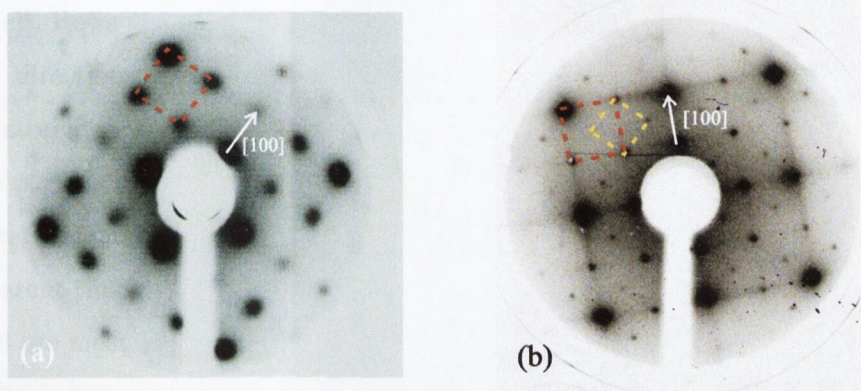
Figure 8.3: (a): LEED mesh of 50 Å thick Fe film on Ge(001) following oxidation at 300°C. Beam energy is 89 eV. The red dashed square shows the primitive unit cell. (b): LEED mesh of the $(\sqrt{2} \times \sqrt{2})R45°$ reconstructed magnetite (001) surface of a single crystal, using the same beam energy, for comparison. The (6×6)Å^2 unreconstructed cell is marked by the red dashed square, and is the same size as the primitive cell in (a). For clarity the $(\sqrt{2} \times \sqrt{2})R45°$ cell is marked with a yellow dashed square.

thin film can be explained by the fact the surface polarity of thin films, which is the driving force behind the reconstruction of magnetite (001) surface, is finite [71].

STM images of such a surface are shown in figure 8.4. Small terraces, with ill defined edges are imaged over the entirety of the surface. Atomic scale rows are discerned on the terraces, seen more clearly in the derivative image [Fig. 8.4(c)]. Rows are imaged on different terraces oriented along two perpendicular directions i.e they have a two fold symmetry. The separation between the atomic rows is $\sim 6 \pm 0.5$ Å, in agreement with the observed LEED mesh. The periodicity along the row direction is not discernible. The measurement of step heights over long ranges is complicated by surface roughness, but it is apparent that neighbouring terraces which exhibit 90° rotation of the atomic rows are most often separated in height by ~ 2 Å. However rotation of rows by 90° is occasionally evident on terraces of the same height. This can be seen from figures 8.4(b), and 8.4(c), where the terraces labelled X and Y are of the same height and yet the atomic rows rotate by 90°. A blue arrow marks the resulting anti-phase boundary.

Scanning tunneling spectroscopy was performed on this surface, using a tunnelling set-point of $V_b = +1$ V and $I_t = 0.1$ nA. Firstly, from figure 8.5(a), it is clear to see that the I(V) properties of the surface change drastically following the described oxidation procedure. Prior to oxidation the I(V) characteristics are consistent with metallic behaviour. As expected, the oxidation results in the appearance of a band gap that is not present for the I(V) spectra of the Fe(50Å)/Ge(001) surface.

Due to the widely varying band gap values of the differing iron oxide phases, the magnitude of the gap can give a good indication of the type of oxide present at the surface. Bulk magnetite has a band gap ~ 0.1 eV,
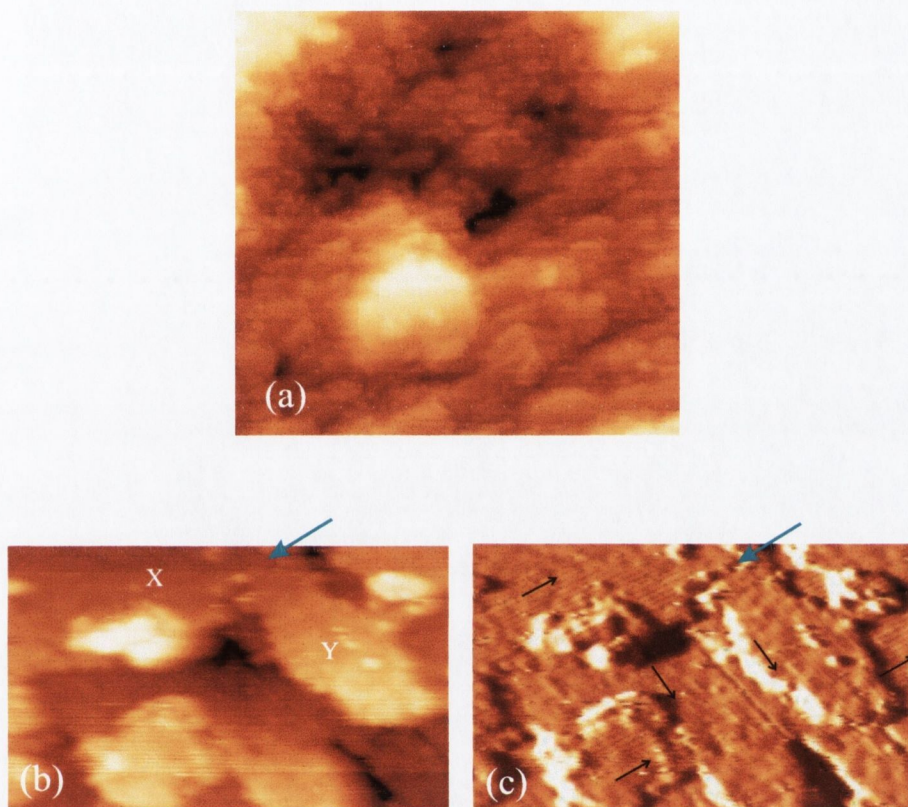
Figure 8.4: (a): (950×920) Å² STM image of the Fe(50 Å)/Ge(001) surface, following oxidation at 300°C. (b): (300×200) Å² STM image of the surface. (c): Differentiated version of figure b. Atomic rows are clearly resolved, oriented in two perpendicular directions, indicated by black arrows. A 6 Å periodicity is measured between the rows. The blue arrow marks the location of an antiphase boundary. All images $I_t = 0.1$ nA, $V_b = +1$ V.

Figure 8.5: (a) I(V) tunneling spectra of the Fe 50 Å/Ge(001) surface pre and post oxidation. (b) Normalised I(V) spectrum of the oxidised surface.

compared to band gaps in the region of 1.94 - 2.3 eV for the other iron oxides [52]. A normalised I(V) curve is presented in figure 8.5(b). A reproducible band gap of 0.15 ± 0.05 eV is measured from spectra taken on the surface following oxidation at 200°C and 300°C. The magnitude of the measured gap is consistent with the presence of magnetite at the surfac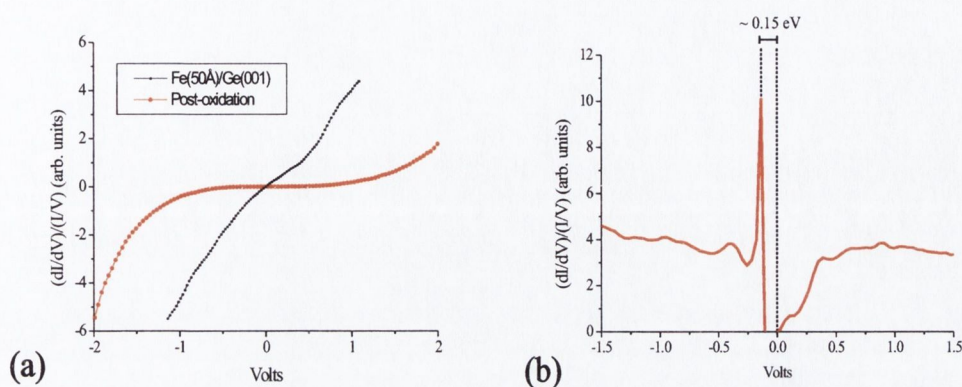e. The I(V) curves obtained compare well with those obtained on a single crystal of magnetite (001), shown in section 5.6, and also with those obtained by Wei *et al.* on the $Fe_3O_4(001)$/MgO surface [96].

8.3.2 Oxidation of Fe at 400°C and 500°C

Fe films of thickness $\sim$ 50 Å were grown onto the clean (2×1) reconstructed Ge(001) surface. They were then oxidised at 5×10^{-6} Torr O_2 for 10 min, at an increased temperature of 400°C. AES shows the formation of an iron oxide phase with low energy peaks again present at 43 eV and 52 eV, as shown in figure 8.6. However, unlike the Fe film oxidation at 300°C, Ge peaks are
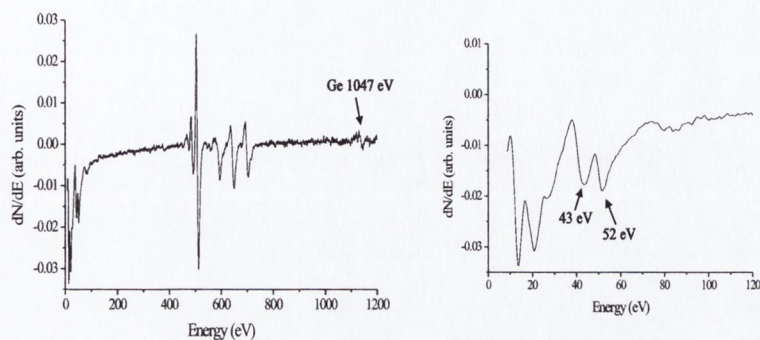
Figure 8.6: Auger spectrum of Fe(50 Å)/Ge(001) surface, following oxidation at 400°C. A germanium concentration of 16% is present at the surface.

resolved in the 1000-1200 region of the AES spectrum. The 1147 eV peak shows a Ge concentration of $\sim$ 16% at the surface. We recall that in the previous chapter it was found that a Fe-Ge alloy was formed on the surface for T $\sim$ 400°C. The presence of Ge at the surface of the Fe oxide, formed by annealing at this temperature, is consistent with this fact.

Fe films, $\sim$ 50 Å thick, were also oxidised under the same conditions at an increased annealing temperature to 500°C. An AES spectrum of the resulting surface is shown in figure 8.7. The surface concentration of Ge is 88%, and the O/Fe ratio 0.5. The Ge low energy Auger peaks at 47 eV, 53 eV and 89 eV are resolved. We note that iron oxide can also give rise to Auger peaks at 47 and 53 eV, however the presence of the peak at 89 is conclusive proof that the origin of these low energy peaks is Ge. The high surface concentration of Ge shows that oxidation of Fe films to form oxide-semiconductor interfaces is not possible at such temperatures, due to interdiffusion between the Fe and Ge.
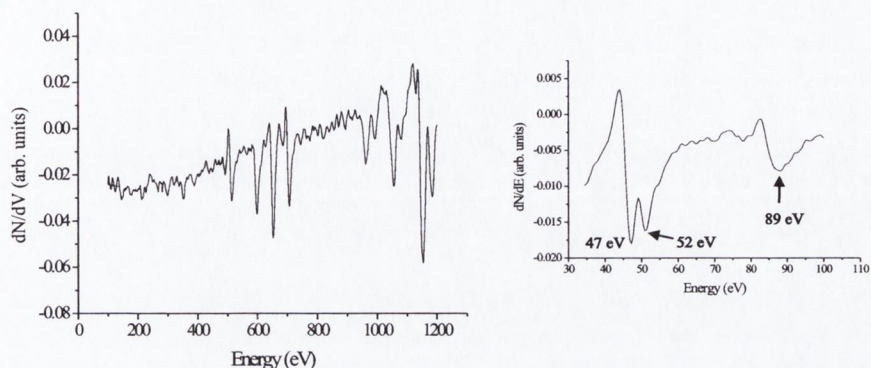
Figure 8.7: Auger spectrum of Fe(50 Å)/Ge(001), following oxidation at 500°C. A germanium concentration of 88% is present at the surface.

8.4 UHV Post Annealing of Iron Oxide Films Formed at 200-300°C

As previously stated, one of the main advantages of using magnetite as a spin injector is that it has a high $T_c \sim 850$ K. However, in order for this to be useful the oxide-semiconductor interface must remain stable to such temperatures. The fact that forming the iron oxide at temperatures at, and above, 400°C results in a severely intermixed surface suggests that the interface is not stable above this temperature. To investigate this further an Fe film was oxidised at 300°C, as described in section 8.3.1. The sample was charaterised as in section 8.3.

It was found that post annealing of the sample for prolonged periods, ($\sim$ 24 hours), in UHV, at temperatures of up to 300°C does not change the surface characteristics. The sample was then post annealed in UHV at 400°C, for 14 hours. An Auger spectrum of the surface following this UHV annealing is shown in figure 8.8. A Ge surface concentration of 95% is mea-
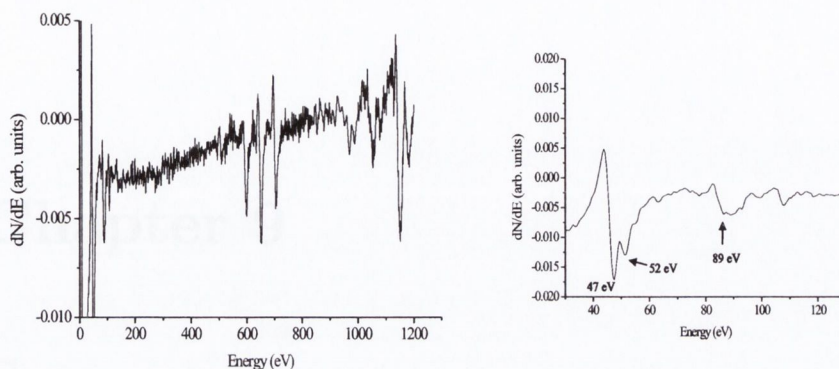
Figure 8.8: Auger spectrum of Fe(50 Å)/Ge(001), following oxidation at 300°C and further annealing in UHV at 400°C for 14 hours. A germanium concentration of 95% is measured.

sured. The Fe concentration is 4.5%, and O 0.5%. This shows that the iron oxide-semiconductor junction is not stable to UHV annealing at temperatures ∼ 400°C.

Chapter 9

Summary

AES, LEED and STM/STS have been used to study the surface properties of three systems; the $Fe_3O_4(001)$ surface, the initial nucleation of Fe on the Ge(001) surface, and finally, iron oxide on Ge(001).

9.1 Conclusions

9.1.1 The $Fe_3O_4(001)$ Surface

The $Fe_3O_4(001)$ surface initially shows the presence of large concentrations of Ca contamination, which give rise to (1×n) surface reconstructions, where n = 1, 2, 3, 4. The clean surface was prepared by cycles of annealing in oxygen, Ar^+ ion etching, and UHV annealing. Following this preparation, the surface exhibits the $(\sqrt{2} \times \sqrt{2})R45°$ LEED mesh. STM was performed on this surface using tips prepared from both anti-ferromagnetic MnNi and non-magnetic W. The surface is terminated at the octahedral, or B-, plane. A 6 Å periodicity along the Fe rows is imaged with MnNi tips. This suggests the formation of Fe-Fe dimers, as the bulk periodicity along the Fe rows is 3 Å, and also due to the large size of the imaged bright points. Two different dimer species are

136

imaged with MnNi, and they each form a $(\sqrt{2} \times \sqrt{2})R45°$ symmetry. Also imaged are apparent local depressions, forming a $(\sqrt{2} \times \sqrt{2})R45°$ array. The latter is consistent with an oxygen vacancy network on the surface, expected due to the polarity of the magnetite (001) surface. The imaged Fe_{oct} rows have a wave-like structure along the [110] direction. W tips image the same structure, and the same $(\sqrt{2} \times \sqrt{2})R45°$ array of depressions, however they do not distinguish between the two dimer species. This can be explained in terms of a spin polarised contribution to the tunnel current when tunneling with MnNi tips. Tunneling spectra of this surface shows a conductivity gap ~ 0.25 eV wide, and states consistent with PES experiments and calculations are resolved.

9.1.2   Fe on the Ge(001) Surface

The clean Ge(001) surface was prepared by cycles of Ar^+ ion etching and UHV annealing. The surface exhibits the well known (2×1) LEED mesh. STM also shows the (2×1) reconstruction and STS of the surface is in general agreement with previous studies, with a band gap of ~ 0.8 eV measured. Deposition of ~ 0.15 ML of Fe at room temperature results in the formation of (12×8) Å² and (12×12) Å² Fe clusters, which are ~ 1.1 Å in height. The clusters nucleate with an exact registry on the Ge(001) surface, with a favoured nucleation site apparent in the STM images. The Ge(001) substrate maintains the dimer row structure of the clean surface following deposition of the Fe film, however the long range (2×1) order breaks down. While some small scale intermixing cannot be ruled out, STM images are consistent with the formation of an abrupt interface. For thicker films (0.5 - 2.4 ML) STM reveals 3-D island growth occurs for this system.

Deposition of 0.15 ML films at elevated substrate temperature of $\sim 200°C$

results in the formation of either 1 or 2 ML high Fe chains or 3-6 ML high Fe islands, elongated along the [110] direction, that is, across the Ge dimer rows. The constituent Fe clusters that make up the chains are the same size as those that form at room temperature. They form due to diffusion of the smaller clusters along the $[1\bar{1}0]$ direction. Larger Fe islands alter the reconstruction of the substrate significantly, giving rise to a striped domain structure of the c(4×2) and p(2×2) reconstructions. Again there is no evidence of severe intermixing for these films. Annealing experiments show severe intermixing to occur for T $\sim$ 400°C.

STS was carried out on the Ge(001) surface with the (12×8) Å^2 and (12×12) Å^2 Fe clusters that form for room temperature deposition. The clusters exhibit a band gap similar to the substrate. Schottky like behaviour is seen in the I(V) spectra taken over the Fe clusters. For 0.5 ML film thickness the Fe islands move toward metallic behaviour, with a measured gap of $\sim$ 0.15 V. The band gap of the Ge between these Fe islands is reduced to $\sim$ 0.4 eV, compared to $\sim$ 0.8 eV for the clean surface, suggesting the existence of metal induced states in the surface band gap of the semiconducting substrate.

9.1.3   Iron Oxide on Ge(001)

Finally, Fe films on Ge(001) were oxidised in an attempt to produce magnetite thin films. Fe films of thickness $\sim$ 50 Å were deposited onto the clean (2×1) reconstructed Ge(001) surface. They were oxidised in 5×10^{-6} Torr O_2, for 10 minutes, at temperatures between 200°C and 300°C. Within this range results were found to be independent of oxidation temperature. AES shows peaks at 43 and 52 eV, consistent with the presence of an iron oxide, and shows no evidence for any Ge present at the surface. LEED is consistent with the formation of unreconstructed Fe_3O_4(001). STM of the surface reveals

rows separated by 6 Å, in agreement with the LEED mesh. The periodicity along the rows is not resolved. STS of the surface shows a gap of ~ 0.15 eV, around E_f, close to the expected value for magnetite. The STS curves are in agreement with those obtained on the single crystal magnetite (001) surface. While the oxide-semiconductor junction is stable to UHV annealing at 300°C, annealing at 400°C results in the diffusion of Ge, as seen with AES.

9.2 Future Work

9.2.1 The Fe_3O_4(001) Surface

Still further characterisation of the Fe_3O_4(001) surface is necessary for a full understanding to be reached. Recent work has come to a general agreement that the octahedral termination is more favourable, however, in terms of the structure of the $(\sqrt{2} \times \sqrt{2})R45°$ reconstructed surface there is still no agreement as to the reasons for this symmetry. Before the electronic and magnetic properties of the surface can be understood and explained, it is essential that the structure of the surface is known. Specifically, it is essential to conclusively show whether there is a $(\sqrt{2} \times \sqrt{2})R45°$ array of oxygen vacancies, or whether the symmetry arises due to some other mechanism.

The charge ordering imaged with MnNi tips is also worth further investigation. Imaging this structure with other magnetic tips, such as Cr, would increase the evidence that this is indeed due to a spin polarised contribution to the tunnel current. Obtaining more images with W tips, over a large range of bias voltages, would conclusively show that the contrast is not due to an electronic contribution to the tunnel current. It would also be interesting to perform STS on the $(\sqrt{2} \times \sqrt{2})R45°$ reconstructed magnetite surface using magnetic tips. Comparison of I(V) curves obtained with magnetic and non-

magnetic tips may provide evidence for spin polarised tunneling when using magnetic tips.

9.2.2 Fe on the Ge(001) Surface

An interesting aspect of this study is the (12×8) Å^2 and (12×12) Å^2 Fe clusters that nucleate on Ge(001), at room temperature. The fact that at elevated temperature these cluster nucleate together to form elongated Fe chains means that one can study how the electronic properties of these chains vary with length, using STS. For example, the dependence of chain length on the band gap, and the Schottky type behaviour, could be studied. Furthermore, given the fact that these chains form at moderate temperature ($\sim$ 200°C), the diffusion of the Fe cluster to form the chains could be studied using variable temperature STM. One could also deposit similar amounts of other elements onto the Ge(001) surface to see whether the cluster formation occurs for other materials. If it does, the I(V) properties of similar sized clusters of different elements could be studied.

9.2.3 Iron Oxide on Ge(001)

Further studies of this system are necessary to ascertain the quality of the interface formed between the oxide and semiconductor. As only surface sensitive techniques have been used here, intermixing at the interface cannot be ruled out. Similarly, while the evidence presented here clearly shows magnetite to form, the techniques used here do not show whether the Fe film is oxidised to magnetite in its entirety. Given the absence of the $(\sqrt{2} \times \sqrt{2})R45°$ reconstruction for the thin films formed here, it would be interesting to attempt to form thicker films, through repeated cycles of Fe deposition and

oxidation at 300°C, to see if the reconstruction does appear for as film thickness increases, as one would expect for a polar surface.

Bibliography

[1] G. A. Prinz. *Science*, 282(5394):1660, 1998.

[2] S. A. Wolf, D. D. Awschalom, R. A. Buhrman, J. M. Daughton, S. von Molnàr, M. L. Roukes, A. Y. Chtchelkanova, and D. M. Treger. *Science*, 294:1488, 2001.

[3] C. M. Fang, G. A. de Wijs, and R. A. de Groot. *J. Appl. Phys.*, 91(10):8340, 2002.

[4] H. Ohno. *Science*, 281:951, 1998.

[5] Y. D. Park, A. T. Hanbicki, S. C. Erwin, C. S. Hellberg, J. M. Sullivan, J. E. Mattson, T. F. Ambrose, A. Wilson, G. Spanos, and B. T. Jonker. *Science*, 295:651, 2002.

[6] A. H. MacDonald, P. Schiffer, and N. Samarth. *Nature Materials*, 4:195, 2005.

[7] B. T. Jonker. *Proceedings of the IEEE*, 91(5):727, 2003.

[8] A. Ionescu, M. Tselepi, D. M. Gillingham, G. Wastlbauer, S. J. Steinmller, H. E. Beere, D. A. Ritchie, and J. A. C. Bland. *Phys. Rev. B*, 72:125404, 2005.

[9] A. Yanase and K. Siratori. *J. Phys. Soc. Jpn.*, 53:312, 1984.

[10] H. J. Zhu, M. Ramsteiner, H. Kostial, M. Wassermeier, H. P. Schönherr, and K. H. Ploog. *Phys. Rev. Lett.*, 87(1):016601, 2001.

[11] Y. X. Lu, J. S. Claydon, Y. B. Xu, D. M. Schofield, and S. M. Thompson. *J. Appl. Phys.*, 95(11):7228, 2004.

[12] Y. X. Lu, J. S. Claydon, E. Ahmad, Y. B. Xu, M. Ali, B. J. Hickey, S. M. Thompson, J. A. D. Matthew, and K. Wilson. *J. Appl. Phys.*, 97:10C313, 2005.

[13] J.C. Vickerman, editor. *Surface Analysis: The Principal Techniques.* Wiley, New York, 1997.

[14] D. Briggs and M.P. Seah. *Practical Surface Analysis: Ion and Neutral Spectroscopy.* Wiley, New York, 1992.

[15] D.P. Woodruff and T. A. Delchar. *Modern Techniques of Surface Science.* Cambridge Solid State Series. Cambridge University Press, second edition, 1994.

[16] G.P. Chambers and J. Fine. *Practical Surface Analysis*, volume 2. Wiley, New York, second edition, 1992. Pages 705-720.

[17] M.A. Van Hove, V.H. Wienberg, and C.-M. Chan. *Low-Energy Electron Diffraction.* Volume 6 of Springer Series in Surface Science. Springer-Verlag,Berlin.

[18] G. Binnig, H. Rohrer, Ch. Gerber, and E. Wiebel. *Phys. Rev. Lett.*, 49:57, 1982.

[19] R. Wiesendanger. *Scannning Probe Microscopy and Spectroscopy.* Cambridge University Press, Cambridge, 1994.

[20] C. Julian Chen. *Introduction to Scanning Tunneling Microscopy*. Cambridge University Press, Cambridge, 1994.

[21] J. Bardeen. *Phys. Rev. Lett.*, 6 (57), 1961.

[22] P. M. Tedrow and R. Meservey. *Phys. Rev. Lett.*, 26:192, 1971.

[23] M. Julliere. *Phys. Lett. A*, 54:225, 1975.

[24] J. C. Slonczewski. *Phys. Rev. B*, 39:6995, 1989.

[25] M. Bode. *Rep.Prog. Phys.*, 66:523–582, 2003.

[26] J. A. Stroscio, R. M. Feenstra, and A. P. Fein. *Phys. Rev. Lett.*, 57 (20):2579, 1986.

[27] N. D. Lang. *Phys. Rev. Lett.*, 34:5947, 1986.

[28] A. Quinn. *Development of an Ultra-High Vacuum Scanning Tunneling Microscope*. PhD thesis, Physics Department. Trinity College Dublin, July 1996.

[29] J. Osing. *Studies Towards Spin Sensitive Scanning Tunneling Microscopy*. PhD thesis, Physics Department. Trinity College Dublin, October 1998.

[30] S. Murphy. *Surface Studies of the Fe/Mo(110) and Fe/W(100) Expitaxial Systems*. PhD thesis, Physics Department. Trinity College Dublin, 2000.

[31] VAT Vacuum Products Ltd. 235 Regents Park Road, Finchley, London N3 3LG, UK.

[32] Physical Electronics Inc. (formerly Perkin-Elmer). 6509 Flying Cloud Drive, Eden.

[33] Vacuum Generators. Maunsell Road, Castleham Industry Estate, Hastings, East Sussex BN8 6SJ, UK.

[34] Caburn MDC Ltd. The Old Diary, Glynde, East Sussex BN8 6SJ, UK.

[35] Pfeiffer Vacuum GmbH. Emmeliusstrasse, K-35614, Asslar.

[36] Saes Getters G.B . Ltd. 5 Southern Court, South St, Reading, Berkshire RG1 4QS U.K.

[37] Omicron. Limberger Str. 75 D-65232 Taunusstein Germany.

[38] Leybold Inficon Inc. Two Technology Place, East Syracuse, NY 13057-9714 U.S.A.

[39] Ciaran Seoighe. *Surface Studies of Magnetite (001)*. PhD thesis, Physics Department. Trinity College Dublin, 2000.

[40] IRCON Inc. 7301 Norh Caldwell Av. Niles, Illinois 60648. U.S.A.

[41] PSP Vacuum Technology. Macclesfield SK11 OLR, U.K.

[42] Stanford Research Systems. 1290-D Reamwood Av., Sunnyvale, California, 94089 U.S.A.

[43] Thermo Vacuum Generators. Maunsell Road, Castleham Ind. Est. Hastings TN38 9NN, England.

[44] S.H. Pan. *Piezo Electric Motor*. International Patent Publication No WO93/19194, 1993. International Bureau, World Intellectual Property Organisation.

[45] Nanotec Electronica. Padilla, 3 1.D 28006-Madrid.Spain.

[46] R. Wiesendanger, I.V. Shvets, D. Bürgler, G. Tarrach, H.J. Güntherodt, J.M.D. Coey, and S. Gräser. *Science*, 255:583, 1992.

[47] A. A. Minakov and I. V. Shvets. *Surf. Sci.*, 236:L377, 1990.

[48] S. F. Ceballos, G. Mariotto, S. Murphy, and I. V. Shvets. *Surf. Sci.*, 523:131–140, 2003.

[49] H. Bourque and R. M. Leblanc. *Rev. Sci. Instrum.*, 66:2695, 1995.

[50] B. Hacker, A. Hillebrand, T. Hartmann, and R. Guckenberger. *Ultramicroscopy*, 42-44:1514, 1992.

[51] S F Ceballos. *STM Study of the (001) and (110) Surfaces of Magnetite*. PhD thesis, Trinity College, Dublin, 2004.

[52] R.M. Cornell and U. Schwertmann. *The Iron Oxides*. VCH Verlagsgesellschaft mbH, first edition, 1996.

[53] E. J. W. Verwey and P. W. Haayman. *Physica*, 8:979, 1941.

[54] E. J. W. Verwey, P. W. Haayman, and R. Romeyn. *J. Chem. Phys.*, 15:181, 1947.

[55] F. Walz. *J. Phys. Condens. Matter*, 14:R285–R340, 2002.

[56] X. W. Li, A. Gupta, G. Xiao, W. Qian, and V. P. Dravid. *Appl. Phys. Lett.*, 73(22):3282, 1998.

[57] P. J. van der Zaag, P. J. H. Bloemen, J. M. Gaines, R. M. Wolf, P. A. A. van der Heijden, R. J. M. van de Veerdonk, and W. J. M. de Jonge. *J. Mag. Mag. Mater.*, 211:301–308, 2000.

[58] S. Iida, K. Mizushima, M. Mizoguchi, K. Kose, K. Kato, K Yanai, N. Goto, and S. Yumoto. *J. Appl. Phys.*, 53:2164, 1982.

[59] M. Mizoguchi. *J. Phys. Soc. Jpn.*, 44:1501, 1978.

[60] J. M. Zuo, J. C. H. Spence, and W. Petuskey. *Phys. Rev. B*, 42:8451, 1990.

[61] J. P. Wright, J. P. Attfield, and P. G. Radaelli. *Phys. Rev. B*, 66:214422, 2002.

[62] J. Garcia, G. Subias, M. G. Proietti, J. Blasco, H. Renevier, J. L. Hodeau, and Y. Joly. *Phys. Rev. B*, 63:054110, 2001.

[63] G. Subias, J. Garcia, J. Blasco, M. Grazia Proietti, H. Renevier, and M. Concepcion Sanchez. *Phys. Rev. Lett.*, 93:156408, 2004.

[64] M. Mizoguchi. *J. Phys. Soc. Jap.*, 70 (8):2333–2344, 2001.

[65] Z. Zhang and S. Satpathy. *Phys. Rev. B*, 44:13319–13331, 1991.

[66] S. F. Alvarado, M. Erbudak, and P. Munz. *Phys. Rev. B*, 14:2740, 1976.

[67] Yu. S. Dedkov, U. Rüdiger, and G. Güntherodt. *Phys. Rev. B*, 65:064417, 2002.

[68] M. Fonin, Yu. S. Dedkov, J. Mayer, U. Rüdiger, and G. Güntherodt. *Phys. Rev. B*, 68:045414, 2003.

[69] G. Hu and Y. Suzuki. *Phys. Rev. Lett.*, 89:276601, 2002.

[70] P. W. Tasker. *J. Phys. C. Solid State Phys.*, 12:4977, 1979.

[71] C. Noguera. *J. Phys. Cond. Matter*, 12 (31):367–410, 2000.

[72] M. Seo, J. B. Lumsden, and R. W. Staehle. *Surf. Sci.*, 50:541, 1975.

[73] A. V. Mijiritskii, M. H. Langelaar, and D. O. Boerma. *J. Mag. Mag. Mat.*, 211:278, 2000.

[74] Yu. S. Dedkov, M. Fonin, D. V. Vyalikh, J. O. Hauch, S. L. Molodtsov, U. Rüdiger, and G. Güntherodt. *Phys. Rev. B*, 70:073405, 2004.

[75] J. M. D. Coey, I. V. Shvets, R. Wiesendanger, and H. J. Güntherodt. *J. Appl. Phys.*, 73:6742, 1993.

[76] G. Tarrach, D. Bürgler, T. Schaub, R. Wiesendanger, and H. Güntherodt. *Surf. Sci.*, 285:1, 1993.

[77] F. C. Voogt, T. Fujii, P.J.M. Smulders, L. Niesen, M. A. James, and T. Hibma. *Phys. Rev. B*, 60:11193, 1999.

[78] J. M. Gaines, P. J. H. Bloemen, J. T. Kohlhepp, C. W. T. Bulle-Lieuwma, R. M. Wolf, R. M. Reinders, R. M. Jungblut, P. A. A. van der Heijden, J. T. W. M. van Eemeren, J. aan de Stegge, and W. J. M. de Jonge. *Surf. Sci.*, 373:85, 1997.

[79] J. M .Gaines, J. T. Kohlhepp, P. J. H. Bloemen, R. M . Wolf, A. Reinders, and R. M Jungblut. *J. Mag. Mag. Mat.*, 165:439–441, 1997.

[80] B. Stanka, W. Hebenstreit, U. Diebold, and S. A. Chambers. *Surf. Sci.*, 49:448, 2000.

[81] S. A. Chambers, S. Thevethasan, and S. A. Joyce. *Surf. Sci.*, 450:L273, 2000.

[82] R. Koltun, M. Herrmann, G. Güntherodt, and V.A.M. Brabers. *Appl. Phys. A*, 73:49–53, 2001.

[83] G. Mariotto, S. Murphy, and I. V. Shvets. *Phys. Rev. B*, 66:245426, 2002.

[84] R. Pentcheva, F. Wendler, H. L. Meyerhiem, W. Moritz, N. Jedrecy, and M. Scheffler. *Phys. Rev. Lett.*, 94:126101, 2005.

[85] C. Cheng. *Phys. Rev. B*, 71:052401, 2005.

[86] Prof J. M. Honig. Purdue University, Indiana, USA.

[87] Guido Mariotto. *Surface Reconstructions of Fe$_3$O$_4$ (001)*. PhD thesis, Physics Department. Trinity College Dublin, 2001.

[88] R. Aragon, R.J. Rasmussen, J.P. Shepherd, J.W. Koenitzer, and J. M. Honig. *J. Magn. Magn. Mater.*, 1335:47–54, 1986.

[89] R. Aragon, R. J. Rasmussen, J.P. Shepherd, J.W. Koenitzer, and J. M. Honig. *J. Magn. Magn. Mater.*, 54-47:1335, 1986.

[90] S. F. Ceballos, G. Mariotto, K. Jordan, S. Murphy, C. Seoigue, and I.V. Shvets. *Surf. Sci.*, 548:106–116, 2004.

[91] G. Mariotto, S. F. Ceballos, S. Murphy, N. Berdunov, C. Seoighe, and I. V. Shvets. *Phys. Rev. B*, 70:035417, 2004.

[92] V. S. Smentkowski and J. T. Yates. *Surf. Sci.*, 232:113, 1990.

[93] H. den Daas, O. L. J. Gijzeman, and J. W. Geus. *Surf. Sci.*, 290:26, 1993.

[94] Y. J. Kim, Y. Gao, and S. A. Chambers. *Surf. Sci.*, 371:358, 1997.

[95] I.V. Shvets, G. Mariotto, K. Jordan, N. Berdunov, R. Kantor, and S. Murphy. *Phys. Rev. B*, 70:155406, 2004.

[96] J. Y. T. Wei and N. C Yeh. *J. Appl. Phys.*, 83 (11):7366, 1998.

[97] A. Chainani, Y. Yokoya, T. Morimoto, T. Takahashi, and S. Todo. *Phys. Rev. B*, 51(24):17976, 1995.

[98] S. Dhar, H. Kosina, V. Palankovski, S. E. Ungersbock, and S. Selberherr. *IEEE Transactions on Electron Devices*, 52(4):527, 2005.

[99] S. Cho, S. Choi, S. C. Hong, Y. Kim, J. B. Ketterson, B. J. Kim, Y. C. Kim, and J. H. Jung. *Phys. Rev. B*, 66:033303, 2002.

[100] W. Zhu, H. H. Weitering, E. G. Wang, E. Kaxiras, and Z. Zhang. *Phys. Rev. Lett.*, 93(12):126102, 2004.

[101] J. W. Freeland, R. H. Kodama, M. Vedpathak, S. C. Erwin, D. J. Keavney, R. Winarski, P. Ryan, and R. A. Rosenberg. *Phys. Rev. B*, 70:033201, 2004.

[102] M. Cantoni, M. Riva, G. Isella, R. Bertacco, and F. Ciccacci. *J. Appl. Phys.*, 97:093906, 2005.

[103] Jian-Long Li, Jin-Feng Jia, Xue-Jin Liang, Xi Liu, Jun-Zhong Wang, Qi-Kun Xue, Zhi-Qiang Li, John S. Tse, Zhenyu Zhang, and S. B. Zhang. *Phys. Rev. Lett.*, 88(6):066101, 2002.

[104] Calculated using CASTEP algorithm of Materials Studio.

[105] R. E. Schlier and H. E. Farnsworth. *J. Chem. Phys.*, 30:917, 1959.

[106] S. D. Kevan. *Phys. Rev. B*, 32:2344, 1985.

[107] D. J. Chadi. *Phys. Rev. Lett.*, 43(1):43, 1979.

[108] J. Ihm, M. L. Cohen, and D. J. Chadi. 21:4592, 1980.

[109] M. T. Yin and M. L. Cohen. *Phys. Rev. B*, 24:2303, 1981.

[110] P. Krüger, A. Mazur, J. Pollmann, and G. Wolfgarten. *Phys. Rev. Lett.*, 57(12):1468, 1986.

[111] S. Ferrer, X. Torelles, V. H. Etgens, H. A. van der Vegt, and P. Fajardo. *Phys. Rev. Lett.*, 75(9):1771, 1995.

[112] S. D. Kevan and N. G. Stoffel. *Phys. Rev. Lett.*, 53(7):702, 1984.

[113] M. Needels, M. C. Payne, and J. D. Joannopoulos. *Phys. Rev. B*, 38(8):5543, 1988.

[114] Y. Takagi, Y. Yoshimoto, K. Nakatsuji, and F. Komori. *Surf. Sci.*, (559):1–15, 2004.

[115] B. Rottger, Th. Bertrams, and H. Neddermeyer. *J. Vac. Sci. Technol. B*, 14(2):925, 1996.

[116] J. A. Kubby, J. E. Griffith, R. S. Becker, and J. S. Vickers. *Phys. Rev. B*, 36(11):6079, 1987.

[117] H. J. W. Zandvliet. *Phys. Rep.*, (388):1–40, 2003.

[118] W. S. Yang, X. D. Wang, K. Cho, J. Kishmoto, S. Fukatsu, T. Hashizume, and T. Sakurai. *Phys. Rev. B*, 50(4):2406, 1995.

[119] H. J. W. Zandvliet, B. S. Swartzentruber, W. Wulfhekel, B. J. Hattink, and B. Poelsema. *Phys. Rev. B*, 57:R6803, 1998.

[120] O. Gurlu, H. J. W. Zandvliet, and B. Poelsema. *Phys. Rev. Lett*, 93(6):066101, 2004.

[121] K. Kushida, K. Hattori, S. Arai, T. Iimori, and F. Komori. *Surf. Sci.*, (442):300–306, 1999.

[122] K. Seino and A. Ishii. *Surf. Sci*, (493):420–425, 2001.

[123] L. H. Chan and E. I. Altman. *Phys. Rev. B*, 66(155339), 2002.

[124] O. Gurlu, H. J. W. Zandvliet, B. Poelsema, S. Dag, and S. Ciraci. *Phys. Rev. B*, 70:085312, 2004.

[125] O. Gurlu, O. A. O. Adam, H. J. W. Zandvliet, and B. Poelsema. *Appl. Phys. Lett.*, 83(22):4610, 2003.

[126] T. Dietl, H. Ohno, F. Matsukuru, J. Cibert, and D. Ferrand. *Science*, 287:1019, 2000.

[127] S. Choi, S. C. Hong, S. Cho, Y. Kim, J. B. Ketterson, C. Jung, K. Rhie, B. J. Kim, and Y. C. Kim. *Appl. Phys. Lett*, 81(19):3606, 2002.

[128] S. Choi, S. C. Hong, S. Cho, Y. Kim, J. B. Ketterson, C. Jung, K. Rhie, B. J. Kim, and Y. C. Kim. *J. Appl. Phys.*, 93(10):7670, 2003.

[129] J. M Kikkawa and D. D. Awschalom. *Phys. Rev. Lett.*, 80(19):4313, 1998.

[130] E. I. Rashba. *Phys. Rev. B*, 62:R16267, 2000.

[131] P. Ma and P. R. Norton. *Phys. Rev. B*, 56(15):9881, 1998.

[132] P. Ma, G. W. Anderson, and P. R. Norton. *Surf. Sci.*, (420):134–141, 1999.

[133] G. A. Prinz. *Ultrathin Magnetic Structures II*. Springer-Verlag, Berlin, 1994.

[134] E. M. Kneedler, B. T. Jonker, P. M. Thabado, R. J. Wagner, B. V. Shanabrook, and L. J. Whitman. *Phys. Rev. B*, 56(13):8163, 1997.

[135] M. Schleberger, P. Walser, M. Hunziker, and M. Landolt. *Phys. Rev. B*, 60(20):14360, 1999.

[136] L. H. Chan, E. I. Altman, and Y. Liang. *J. Vac. Sci. Technol. A*, 19(3):976, 2001.

[137] J. S. Hovis, R. J. Hamers, and C. M. Greenlief. *Surf. Sci. Lett.*, 440:L815–L819, 1999.

[138] J. G. Nelson, W. J. Gignac, R. S. Williams, S. W. Robey, J. G. Tobin, and D. A. Shirley. *Phys. Rev. B*, 27(6):3924, 1983.

[139] T. Miller T. C. Hsieh and T. C. Chiang. *Phys. Rev. B*, 30:7005, 1984.

[140] J. Alvarez, V. H. Etgens, X. Torrelles, H. A. van der Vegt, P Farjardo, and S. Ferrer. *Phys. Rev. B*, 54(8):5581, 1996.

[141] Shangjr Gwo, Chung-Pin Chou, Chung-Lin Wu, Yi-Jen Ye, and Shu-Ju. *Phys. Rev. Lett.*, 90:185506, 2003.

[142] T. M. Galea, C. Ordas, E. Zoethout, H. J. W. Zandvliet, and B. Poelsema. *Phys. Rev. B*, 62(11):7206, 2000.

[143] P. N. First, J. A. Stroscio, R. A. Dragoset, D. T. Pierce, and R. J. Cellota. *Phys. Rev. Lett.*, 63:1416, 1989.

[144] P. Radojkovic, M. Schwartzkopff, M. Enachescu, E. Stefanov, E. Hartmann, and F. Koch. *J. Vac. Sci. Technol. B*, 14:1229, 1996.

[145] T. C. G. Reusch, M Wenderoth, L Winking, N. Quass, and R. G. Ulbrich. *Phys. Rev. Lett.*, 93(20):206801, 2004.

[146] G. Schmidt, D. Ferrand, L. W. Molenkamp, A. T. Filip, and B. J. van Wees. *Phys. Rev. B.*, 62:R4790, 2000.

[147] G. Ertl and K. Wandelt. *Surf. Sci.*, 50:479, 1975.